

## **COMPARISON OF FAULT-DETECTION METHODS IN PHOTOVOLTAIC MODULES**

An analysis of techniques utilising IV-tracing, UVF-imaging, EL-imaging,  
and IRT-imaging via visual analysis for fault-detection in PV-modules

HERMAN SCHULZE LJOSLAND

**SUPERVISOR**

Anne Gerd Imenes

**CO-SUPERVISOR**

Ingunn Burud

**University of Agder, 2022**

Faculty of Engineering and Science

Department of Engineering and Sciences





## **Abstract**

This Master's thesis is written to fulfil the graduation requirements of the Master's Programme in Renewable Energy Engineering during the spring of 2022, and is based on previous work at the University of Agder (UiA). The thesis compares the five different PV-module fault-detection techniques of UVF-, indoor/outdoor IRT-, EL-imaging, and IV-tracing, based on the current literature and the experiments performed on five select PV-modules. The faults of the five PV-modules are defined by visual inspection of the experiment results, and an order of when to use each of the five fault-detection techniques is presented.

It was found that the faults-types detectable by these methods are cell-cracks, isolated cell-areas, circuit issues, resistance issues, hot-spots, defective bypass-diode, potential induced degradation, and optical degradation. The five tested PV-modules, available at UiA, were found to be suffering from cell-cracks of varying severity from negligible to causing areas of cells to be isolated from the circuit, hot-spots, high internal cell-resistance, and faults caused by production-issues or mechanical overloading. One should use IRT-imaging, UVF-imaging, IV-tracing, and EL-imaging, in order, to perform fault-detection on modules in a PV-farm. This order is based on the technique's fault-detection efficacy, and how intrusive it is to the normal operation of the PV-farm.



## Preface

My academic background is a bachelor's degree in renewable energy engineering, fulfilled with a Bachelor's thesis on bio-TPU as a replacement for conventional TPU in lay-flat hoses in collaboration with Mandals AS and the University of Agder. This is a Master's thesis titled "Comparison of fault-detection methods in photovoltaic modules", which is based on my unpublished research project in the course ENE503 at the University of Agder, named "Power loss estimation of different PV-module faults" [1]. The thesis has been written to fulfil the graduation requirements of the Master's Programme in Renewable Energy Engineering at the University of Agder (UiA). I was engaged in researching and writing this thesis from January to May of 2022.

The reasoning for my interest in this project is twofold. The first reason was the ever-increasing need for good fault-detection protocols for PV-modules, as the amount of electricity production from PV across the world is ever increasing. The second reason was the practical nature of the project, giving many opportunities to work with the PV-modules and the relevant testing equipment. I would like to thank my supervisors Anne Gerd Imenes (UiA), and Ingunn Burud at the Norwegian University of Life Sciences (NMBU), for their excellent support, insight, and guidance during the process of creating this thesis. I would also like to thank Oscar Kwame Segbefia, for sharing his experience in working with many of the techniques used in the experiments.

Some parts of this thesis are quoted from the earlier work of ENE503, such instances are labelled accordingly, while the method, results, and discussion segments are all new in this thesis. In the case of whole paragraphs with a single source, the associated citation is noted after the last period of the last sentence of the paragraph. [X]

I hope you enjoy your reading.

Herman Schulze Ljosland

Grimstad, 2022.05.16



## Individual/Group Mandatory Declaration

The individual student or group of students is responsible for the use of legal tools, guidelines for using these and rules on source usage. The statement will make the students aware of their responsibilities and the consequences of cheating. Missing statement does not release students from their responsibility.

1.	I/We hereby declare that my/our report is my/our own work and that I/We have not used any other sources or have received any other help than mentioned in the thesis.	<input checked="" type="checkbox"/> Yes <input type="checkbox"/> No
2.	<b>I/we further declare that this thesis:</b> <ul style="list-style-type: none"><li>• has not been used for another exam at another department/university/university college in Norway or abroad;</li><li>• does not refer to the work of others without it being stated;</li><li>• does not refer to own previous work without it being stated;</li><li>• have all the references given in the literature list;</li><li>• is not a copy, duplicate or copy of another's work or manuscript.</li></ul>	<input checked="" type="checkbox"/> Yes <input type="checkbox"/> No
3.	I/we am/are aware that violation of the above is regarded as cheating and may result in cancellation of exams and exclusion from universities and colleges in Norway, see Universitets- og høyskoleloven §§4-7 og 4-8 og Forskrift om eksamen §§ 31.	<input checked="" type="checkbox"/> Yes <input type="checkbox"/> No
4.	I/we am/are aware that all submitted theses may be checked for plagiarism.	<input checked="" type="checkbox"/> Yes <input type="checkbox"/> No
5.	I/we am/are aware that the University of Agder will deal with all cases where there is suspicion of cheating according to the university's guidelines for dealing with cases of cheating.	<input checked="" type="checkbox"/> Yes <input type="checkbox"/> No
6.	I/we have incorporated the rules and guidelines in the use of sources and references on the library's web pages.	<input checked="" type="checkbox"/> Yes <input type="checkbox"/> No

## Publiseringsavtale

Authorization for electronic publishing of the thesis.

Author(s) have copyrights of the thesis. This means, among other things, the exclusive right to make the work available to the general public (Åndsverkloven. §2).

All theses that fulfill the criteria will be registered and published in Brage Aura and on UiA's web pages with author's approval.

Theses that are not public or are confidential will not be published.

I hereby give the University of Agder a free right to make the task available for electronic publishing:	<input checked="" type="checkbox"/> Yes <input type="checkbox"/> No
Is the thesis confidential?	<input type="checkbox"/> Yes <input checked="" type="checkbox"/> No
Is the task except for public disclosure?	<input type="checkbox"/> Yes <input checked="" type="checkbox"/> No



# Contents

<b>List of Figures</b>	<b>x</b>
<b>List of Tables</b>	<b>xiii</b>
<b>Abbreviations</b>	<b>xiv</b>
<b>Symbols</b>	<b>xiv</b>
<b>1 Introduction</b>	<b>1</b>
1.1 Background . . . . .	1
1.2 Research Question . . . . .	2
1.3 About this Thesis . . . . .	2
<b>2 Theory</b>	<b>3</b>
2.1 Cell- and Module Construction . . . . .	3
2.1.1 Photovoltaic Cell Structure . . . . .	3
2.1.2 Modules and Substrings . . . . .	4
2.1.3 Bypass Diodes . . . . .	5
2.2 Photovoltaic Systems . . . . .	5
2.3 Sensors for Characterisation . . . . .	6
2.4 Standard Test Conditions . . . . .	6
2.5 Infrared Thermography Imaging . . . . .	7
2.6 Electroluminescence Imaging . . . . .	9
2.6.1 Camera . . . . .	9
2.6.2 Daylight Imaging . . . . .	10
2.7 Current-Voltage Testing . . . . .	11
2.8 Ultraviolet Fluorescence Imaging . . . . .	12
<b>3 Literature Review</b>	<b>15</b>
3.1 Current-Voltage Testing . . . . .	15
3.2 Infrared Thermography Testing . . . . .	18
3.3 Electroluminescence Testing . . . . .	20
3.4 Ultraviolet Fluorescence Testing . . . . .	28
3.5 Optical Degradation . . . . .	30
3.6 Hot-Spots . . . . .	31
3.7 Fault Statistics . . . . .	32
3.8 Fault Detection Summary . . . . .	34
<b>4 Method</b>	<b>37</b>
4.1 Preliminary Research . . . . .	37
4.2 Health and Safety Considerations . . . . .	37
4.3 Common Methods for All Tests . . . . .	38

4.4	Ultraviolet Fluorescence Experiments . . . . .	39
4.5	Current-Voltage Tracing Experiments . . . . .	40
4.5.1	Automatic Current-Voltage Tracing . . . . .	40
4.5.2	Manual Current-Voltage Tracing . . . . .	41
4.6	Infrared Thermography Experiments . . . . .	42
4.7	Electroluminescence Experiments . . . . .	44
<b>5</b>	<b>Results</b>	<b>47</b>
5.1	Module $\alpha$ -I . . . . .	48
5.2	Module $\alpha$ -II . . . . .	52
5.3	Module $\alpha$ -III . . . . .	56
5.4	Module $\alpha$ -IV . . . . .	60
5.5	Module $\beta$ -I . . . . .	64
<b>6</b>	<b>Discussion</b>	<b>69</b>
6.1	Module $\alpha$ -I . . . . .	70
6.2	Module $\alpha$ -II . . . . .	74
6.3	Module $\alpha$ -III . . . . .	76
6.4	Module $\alpha$ -IV . . . . .	78
6.5	Module $\beta$ -I . . . . .	82
6.6	Fault Detection Validity . . . . .	84
6.7	Method Comparison . . . . .	85
<b>7</b>	<b>Conclusion</b>	<b>89</b>
<b>8</b>	<b>Further Work</b>	<b>91</b>
	<b>References</b>	<b>93</b>
	<b>Appendix</b>	<b>A1</b>
<b>A</b>	<b>Blank IEC Visual Inspection Checklist</b>	<b>A2</b>
<b>B</b>	<b>Westech CL-160WM Data-Sheet</b>	<b>A3</b>



## List of Figures

2.1.1	Simplified model of electric potential generated in a photovoltaic cell. . . . .	3
2.1.2	Simplified model of a photovoltaic cell cross-section [2]. . . . .	4
2.1.3	Example of photovoltaic module with 60 cells in series. . . . .	4
2.1.4	Example of photovoltaic module with an active bypass diode, caused by a cell-fault. The current flow, and active circuit is marked in red, while the inactive is marked in blue. . . . .	5
2.4.1	AM spectra compiled from data by National Renewable Energy Laboratory [3]. . .	6
2.5.1	Emissivity relative to the viewing angle of a photovoltaic module and the reflected temperature [4]. . . . .	7
2.5.2	Optimal viewing angle for infrared thermography. . . . .	8
2.6.1	Optimum angle for electroluminescence photography. . . . .	10
2.7.1	Example of a nominal current-voltage-, and power-voltage curve, with noted maximum power point, short-circuit voltage/current and open-circuit voltage. . . . .	11
2.8.1	Illustrative example of ultraviolet fluorescent build-up and circumferential photo-bleaching. . . . .	12
2.8.2	Representation of how ingress of oxygen and water, as well as hot-spots affect the ultraviolet fluorescence response of a photovoltaic module [5]. . . . .	13
3.1.1	Examples of different faults or other performance altering conditions, and how they affect the current-voltage curve [6]. . . . .	15
3.1.2	Standard equivalent single diode circuit of photovoltaic cell, or -module [2]. . . . .	16
3.1.3	Current-voltage curve response with varying series resistance [6]. . . . .	17
3.1.4	Current-voltage curve response with varying shunt resistance [2]. . . . .	17
3.2.1	Table of infrared images and current-voltage curves correlated to different cell faults [7]. . . . .	18
3.2.2	Table of infrared images and current-voltage curves correlated to different circuit faults [7]. . . . .	19
3.3.1	Mono- and multi-crystalline photovoltaic cells as seen using electroluminescence imaging [8]. . . . .	20
3.3.2	Two examples of electroluminescence imaging used for fault detection, not visible with conventional RGB photography [8]. . . . .	21
3.3.3	Internal cell temperature affects the visibility of the multi-crystalline grain boundaries [8]. . . . .	21
3.3.4	Electroluminescence scan of the dashed line in Figure 3.3.3, as well as the difference between the 100- and 25°C measurements. The scan was made left to right. [8] . . .	22
3.4.1	Electroluminescence- and ultraviolet fluorescence response of a photovoltaic cell with cross-crack fault [5]. . . . .	28
3.4.2	Cell temperatures and ultraviolet fluorescence response of a photovoltaic module with prolonged operation with varying cell temperature [5]. . . . .	28
3.5.1	Electroluminescence image of a module with an area of optical degradation, at forward current of (a) $I_{SC}$ , and (b) $0,1 \cdot I_{SC}$ [9]. . . . .	30

3.5.2	Ultraviolet fluorescence image of two modules, one with optical degradation causing low ultraviolet response (a), and one without optical degradation and therefore higher ultraviolet response (b) [9]. . . . .	30
3.6.1	Infrared thermography, and current-voltage/power-voltage response of a photovoltaic module suffering from reduced fill-factor caused by hot-spot [10]. . . . .	31
3.6.2	Infrared thermography of a problematic junction-box, and an electroluminescence image of a module suffering from hot-spots [10]. . . . .	32
4.3.1	Junction boxes of the four of the modules tested in these experiments. . . . .	39
4.5.1	Irradiance testing equipment used in conjunction with HT I-V 500W. . . . .	41
4.5.2	Equipment used for manual current-voltage tracing of photovoltaic modules. . . . .	42
4.6.1	Photography of the author with FLIR A6750 MWIR camera on tripod, set up for infrared thermography imaging of photovoltaic modules. <i>Photo: Anne Gerd Imenes.</i>	43
4.7.1	All three colour bands of red, green, and blue, from electroluminescence experiment result image of a photovoltaic module. . . . .	44
4.7.2	Equipment setup for both the electroluminescence- and ultraviolet fluorescence imaging experiments. . . . .	45
5.1.1	Photography of module with designation $\alpha$ -I, with circuit diagram overlay. . . . .	48
5.1.2	Measured and STC-corrected current- and power- curves as a function of voltage, module $\alpha$ -I. . . . .	48
5.1.3	STC-corrected and nominal current- and power- curves as a function of voltage, module $\alpha$ -I, according to data-sheet nominal- and open-circuit voltage. . . . .	49
5.1.4	STC-corrected and nominal current- and power- curves as a function of voltage, module $\alpha$ -I, according to measured maximum power point-, and open-circuit voltage.	49
5.1.5	$\alpha$ -I indoor ultraviolet fluorescence image. . . . .	50
5.1.6	$\alpha$ -I operational, outdoor infrared thermography image. . . . .	50
5.1.7	$\alpha$ -I indoor electroluminescence image. . . . .	51
5.1.8	$\alpha$ -I forward-current infrared image. . . . .	51
5.2.1	Photography of module with designation $\alpha$ -II, with circuit diagram overlay, and crop of bypass-diode configuration. . . . .	52
5.2.2	Current- and power- curves as a function of voltage, module $\alpha$ -II. . . . .	52
5.2.3	$\alpha$ -II indoor ultraviolet fluorescence image. . . . .	53
5.2.4	$\alpha$ -II operational, outdoor infrared thermography image. . . . .	54
5.2.5	$\alpha$ -II indoor electroluminescence image. . . . .	54
5.2.6	$\alpha$ -II forward-current infrared image. . . . .	55
5.3.1	Photography of module with designation $\alpha$ -III, with circuit diagram overlay, and crop of bypass-diode configuration. . . . .	56
5.3.2	Current- and power- curves as a function of voltage, module $\alpha$ -III. . . . .	56
5.3.3	$\alpha$ -III indoor ultraviolet fluorescence image. . . . .	57
5.3.4	$\alpha$ -III operational, outdoor infrared thermography image. . . . .	58
5.3.5	$\alpha$ -III indoor electroluminescence image. . . . .	58
5.3.6	$\alpha$ -III forward-current infrared image. . . . .	59
5.4.1	Photography of module with designation $\alpha$ -IV, with circuit diagram overlay. . . . .	60

5.4.2	Current- and power- curves as a function of voltage, module $\alpha$ -IV. . . . .	60
5.4.3	$\alpha$ -IV indoor ultraviolet fluorescence image. . . . .	61
5.4.4	$\alpha$ -IV operational, outdoor infrared thermography image. . . . .	61
5.4.5	$\alpha$ -IV indoor electroluminescence image. . . . .	62
5.4.6	$\alpha$ -IV forward-current infrared image. . . . .	62
5.5.1	Photography of module with designation $\beta$ -I, with circuit diagram overlay. Bypass-configuration unknown. . . . .	64
5.5.2	$\beta$ -I current- and power-curves as a function of voltage. . . . .	64
5.5.3	$\beta$ -I ultraviolet fluorescence image. . . . .	65
5.5.4	$\beta$ -I operating infrared image. . . . .	66
5.5.5	$\beta$ -I electroluminescence image. . . . .	66
5.5.6	$\beta$ -I forward-current infrared image. . . . .	67
6.1.1	All results from experiments performed with module $\alpha$ -I. . . . .	71
6.1.2	Indoor ultraviolet fluorescence image of module $\alpha$ -I, with zoomed area of interest. . . . .	71
6.1.3	$\alpha$ -I infrared thermography image overlaid EL-image. . . . .	72
6.2.1	All results from experiments performed with module $\alpha$ -II. . . . .	75
6.3.1	All results from experiments performed with module $\alpha$ -III. . . . .	77
6.4.1	All results from experiments performed with module $\alpha$ -IV. . . . .	79
6.4.2	$\alpha$ -IV infrared thermography image overlaid EL-image. . . . .	80
6.4.3	Highlighting of ultraviolet fluorescence- and electroluminescence image, point-crack in module $\alpha$ -IV. . . . .	80
6.5.1	All results from experiments performed with module $\beta$ -I. . . . .	83

## List of Tables

2.6.1	Detectors and their applicable wavelengths [11]. . . . .	9
3.1.1	How examples of faults, or other performance altering conditions, affect the IV-characteristics [6]. . . . .	15
3.3.1	Electroluminescence fault images from the IEA-PVPS T13-01:2014 report [12]. . . . .	23
3.4.1	Ultraviolet fluorescence fault images [12]. . . . .	29
3.8.1	Main fault symptoms with infrared imaging, electroluminescence imaging, current-voltage testing, and ultraviolet fluorescence imaging. Each method is shown by examples that in general do not correspond to the same module. . . . .	34
4.3.1	Modules tested, their designation, and characteristics. . . . .	38
5.1.1	Test result table from current, voltage, and power experiments of module $\alpha$ -I, including four the stages of measured, STC-corrected, nominal, and altered conditions. . . . .	49
5.1.2	Main temperatures of interest, outdoor infrared thermography of module $\alpha$ -I. . . . .	50
5.1.3	Main temperatures of interest, indoor infrared thermography of module $\alpha$ -I with short-circuit current applied in forward bias. . . . .	51
5.2.1	Relevant STC- and nominal values for module $\alpha$ -II. . . . .	53
5.2.2	Main temperatures of interest, outdoor infrared thermography of module $\alpha$ -II. . . . .	54
5.2.3	Main temperatures of interest, indoor infrared thermography of module $\alpha$ -II with short-circuit current applied in forward bias. . . . .	55
5.3.1	Relevant STC- and nominal values for module $\alpha$ -III. . . . .	57
5.3.2	Main temperatures of interest, outdoor infrared thermography of module $\alpha$ -III. . . . .	58
5.3.3	Main temperatures of interest, indoor infrared thermography of module $\alpha$ -III with short-circuit current applied in forward bias. . . . .	59
5.4.1	Relevant STC- and nominal values for module $\alpha$ -IV. . . . .	61
5.4.2	Main temperatures of interest, outdoor infrared thermography of module $\alpha$ -IV. . . . .	62
5.4.3	Main temperatures of interest, indoor infrared thermography of module $\alpha$ -IV with short-circuit current applied in forward bias. . . . .	62
5.4.4	Two extreme examples of corrected short-circuit current, and open-circuit voltage based on measured temperature, temperature difference and data-sheet values . . . . .	63
5.5.1	Relevant STC- and nominal values for module $\beta$ -I. . . . .	65
5.5.2	Main temperatures of interest, outdoor infrared thermography of module $\beta$ -I. . . . .	66
5.5.3	Main temperatures of interest, indoor infrared thermography of module $\beta$ -I with short-circuit current applied in forward bias. . . . .	67

## Abbreviations

Abbreviation	Description
c-Si	Crystalline silicon
EL	Electroluminescence
EVA	Ethylene-vinyl acetate
FF	Fill-factor
IEA	International Energy Agency
IEC	International Electrotechnical Commission
IR	Infrared
IRT	Infrared thermography
MPP	Maximum power point
Multi-C/Mono-C	Multi-crystalline/Mono-crystalline
NREL	National Renewable Energy Laboratory
PID	Potential induced degradation
PV	Photovoltaic
RGB	Red-green-blue
STC	Standard test conditions
UiA	University of Agder
UV	Ultraviolet
UVF	Ultraviolet fluorescence

## Symbols

Symbol	Description
$G$	Incident irradiance
$k$	Boltzmann constant
$I_{MPP}$	Maximum power point current
$I_{SC}$	Short-circuit current
$q$	Elementary charge
$R_S$	Series resistance
$R_{Sh}$	Shunt Resistance
$T$	Temperature
$V_{MPP}$	Maximum power point voltage
$V_{OC}$	Open-circuit voltage



# 1 Introduction

This chapter of the report, addresses the background for the work done in this Master's Thesis, the research question undertaken, and an "About this Thesis"-section. Chapter 1.1 is mostly quoted from the unpublished research project "Power loss estimation of different PV-module faults" by H. S. Ljosland [1], except for some necessary edits.

## 1.1 Background

Electrical energy production is a central point of discussion in today's society, given the prospect of anticipated issues caused by climate change and the push towards more renewable energy sources. The European Green New Deal has set a goal for Europe to be a carbon-neutral continent within the year 2050 [13]. A central point of this goal entails replacing fossil energy sources with renewable ones. Harvesting energy from the plentiful solar radiation will play a key role in realising this goal. Photovoltaics being the fastest-growing source of renewable energy [14], the need for efficient fault detection is increasing each year.

Faults in photovoltaic (PV) modules can affect its power production efficiency to a varying degree, depending on the nature of the fault. The faults may vary in origin i.e. production defects, age-related degradation or physical damage from outside sources. Keeping the efficiency of PV-modules as high as possible results in more efficient use of the area they occupy, as well as keeping the production of electricity high. Different environments may also affect the PV-modules in different ways. Two quite different, potentially problematic examples would be sand storms in the Sahara desert and snow in the Arctic, of which both may result in the same obstruction of incident irradiance on the PV-modules. Different areas may also have differing standards in terms of technology, quality control, logistics, etc. which may prompt varying needs for fault detection frequency and/or techniques. From a social perspective, the efficient use of land has been a central issue for the last couple of years, as seen in the discussion of recent land-based wind turbine farms. As economics is the most important factor in a PV-farm, fault detection becomes important as module efficiency affects the income from the PV-farm.

There are several ways to detect faults in PV-modules. The Master's thesis compares five different techniques of fault detection in PV-modules, by comparing the results, their viability in fault detection of PV-modules, and how intrusive the techniques are in a PV-farm setting. The five methods used in this thesis are current-voltage characteristic tests, indoor/outdoor infrared thermography, ultraviolet fluorescence, and electroluminescence photography.

## 1.2 Research Question

How do the techniques of fault-detection of photovoltaic modules compare to each other, in regards to fault-detection by visual inspection of the results?

- How does current-voltage tracing, indoor ultraviolet fluorescence imaging, indoor electroluminescence imaging, outdoor operational infrared thermography, and indoor infrared thermography at forward-biased short-circuit current compare against each other?
- Of the five modules selected for characterisation, which types of faults are detectable with the use of these techniques?
- In which order should one use these techniques to identify faulty modules in a photovoltaic farm setting?

## 1.3 About this Thesis

This Master's thesis is divided into eight main chapters. Chapter 1: Introduction presents the background/motivation of the thesis, and the research question to be answered. Chapter 2: Theory presents the relevant basic information needed for comprehending the concepts discussed later in the thesis. Chapter 3: Literature Review presents and discusses the current research in the field of fault detection in photovoltaic (PV) modules. This chapter is the foundation of the discussion, and the method in addition to the relevant IEC-standards. Chapter 4: Method describes the procedure taken for each of the fault-detection techniques performed during the experiments of this thesis. All of the results found by these methods are then presented in Chapter 5: Results. These results, and the techniques are then discussed in Chapter 6: Discussion, before a conclusion is drawn and presented in Chapter 7: Conclusion. Finally, Chapter 8: Further Work discusses the further work that should be done, based on the findings in the thesis, to further the research in the field of fault detection in PV-modules.

The thesis was created based on the unpublished research project titled "Power loss estimation of different PV-module faults" by H. S. Ljosland [1], during the 7,5 ECTS course "ENE-503 Energy Research Project" at the University of Agder. The thesis was produced with the available equipment and facilities at the Grimstad campus of the University of Agder, from January to May of 2022. The thesis adds to the current research in the field by comparing the five chosen fault-detection techniques, and developing a step-by-step approach to fault-detection of in-field PV-modules.



## 2 Theory

The theory chapter of this report, up to and including Chapter 2.7: Current-Voltage Testing, is quoted from the unpublished research project in the ENE503-course "Power loss estimation of different PV-module faults" by H. S. Ljosland [1], with some clarifying reformulation. The chapter encompasses the theoretical foundation of understanding the chapters hereinafter: Cell- and Module Construction, Photovoltaic Systems, Standard Test Conditions, Infrared Thermography Imaging, Electroluminescence Imaging, Current-Voltage Testing, and Ultraviolet Fluorescence Imaging.

### 2.1 Cell- and Module Construction

#### 2.1.1 Photovoltaic Cell Structure

The simplest way of describing a silicon-based photovoltaic cell is a *p-n junction*<sup>1</sup> with one side illuminated, where photons are absorbed and may generate *electron-hole pairs*<sup>2</sup> if the photon energy is sufficient. The p-n junction separates the "holes" and electrons to each side of the cell, which induces an electric potential across the cell [2, 17]. A simplified model of this process is shown in Figure 2.1.1.

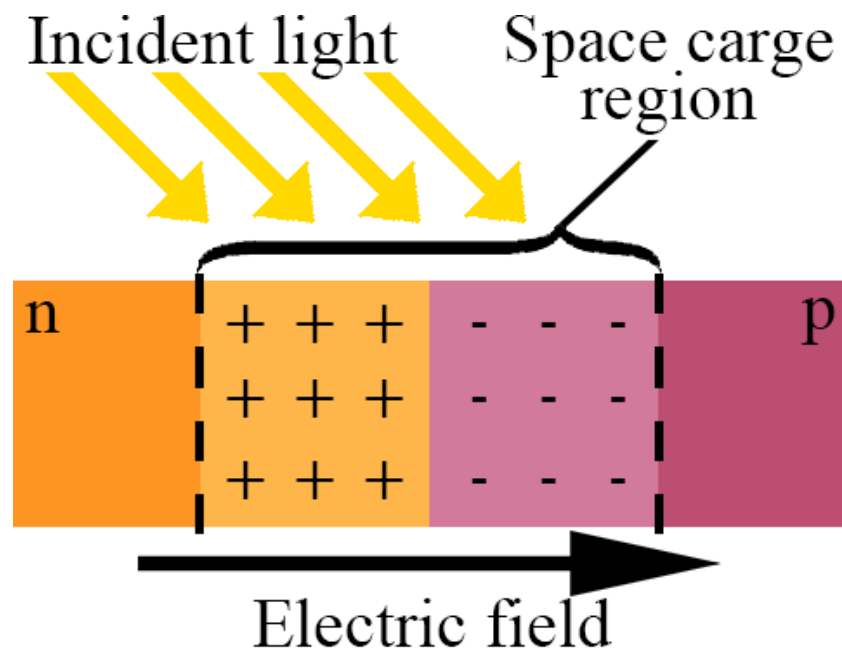


Figure 2.1.1: Simplified model of electric potential generated in a photovoltaic cell.

If the cell is a closed circuit, the aforementioned electric potential will induce a current through the cell. This current allows for the holes to be filled, through the process known as electron-hole pair recombination. The frequency of this process is dependent on the material properties and its temperature. If an absorbed photon lacks the required energy to free the electron, the energy will be converted into heat. The same goes for photons with more energy than required, as the surplus energy of the absorbed photon is converted to heat. [2, 17]

<sup>1</sup>"P-n junction, in electronics, the interface within diodes, transistors, and other semiconductor devices between two different types of materials called p-type and n-type semiconductors." [15].

<sup>2</sup>Given enough energy, an electron can cross the bandgap into the conduction band; the spot left by the electron is called a "hole" [16].

The basic structure of a photovoltaic (PV) cell, from back to front, consists of a backing plate,  $p^-$ -base,  $n^+$ -emitter, anti-reflection coating, and the top electrical grid. The top electrical grid includes the main busbar and the connected front contacts, called "fingers". The external load would be connected to the cell with cathode at the busbar and anode at the back contact. Several designs of contacts and doped regions of PV-cells are in use, Figure 2.1.2 is an example of one of them. [2, 17]

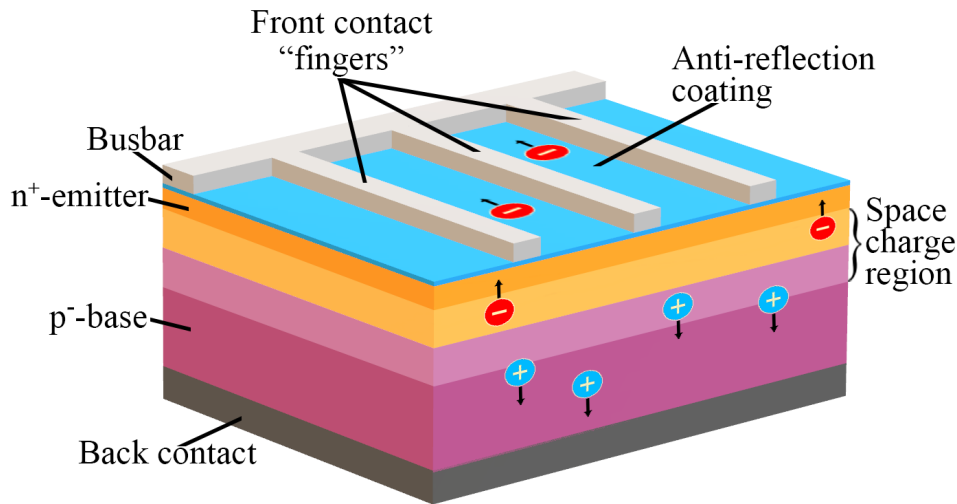


Figure 2.1.2: Simplified model of a photovoltaic cell cross-section [2].

### 2.1.2 Modules and Substrings

Several PV-cells can be connected together in a module to increase the current and/or voltage delivered. Connecting the cells in series, called stings, increases the voltage by a factor of the number of cells in the string. Connecting strings in parallel increases the current by a factor of the number of parallel strings. Dividing these strings utilising for example bypass diodes are called substrings. [2] An illustrative example is shown in Figure 2.1.3, where 60 cells are connected in series. In this example, with the assumption of cell voltages of 0,6 V, the open circuit would be 36 V.

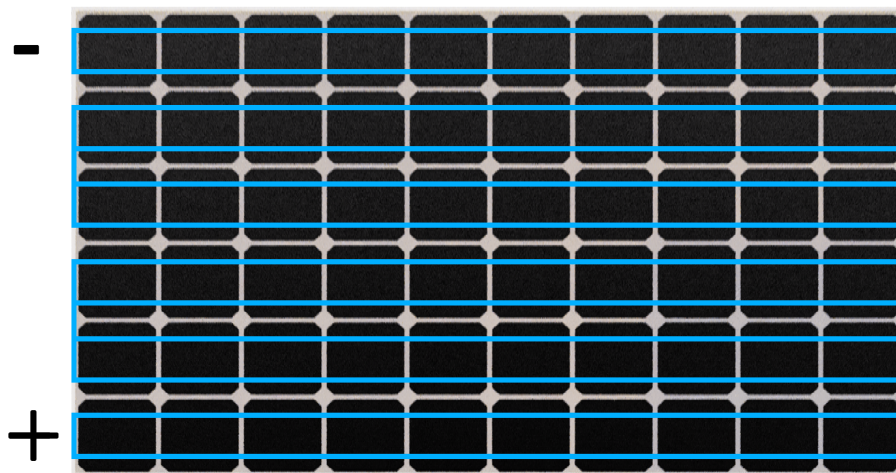


Figure 2.1.3: Example of photovoltaic module with 60 cells in series.

### 2.1.3 Bypass Diodes

In the event of shading or faults in one or more cells in the module, the current through the affected cells would drop drastically. The current drop in the cell affects the current through the whole string, lowering the efficiency of the module. The shading of one cell may also cause heat to build up, because of the increased resistance in the cell. [2]

Adding a bypass diode in anti-parallel with the cell or string helps mitigate these issues by allowing for the current to flow through the diode. A bypass diode for each cell would assure the least drop in efficiency in the case of local shading or faults in one module, but the cost would be high compared to the benefits. Therefore, the bypass diodes are most often connected across several cells, with a maximum of about 15 cells per diode for Si-cells, to reduce the total cost of the module. [18]

Figure 2.1.4 shows a case of a cell in a PV-module suffering from a fault, causing the current through the cell to drop significantly. This causes the bypass diode to be forward biased, allowing for the current to flow through it instead of the faulty cell.

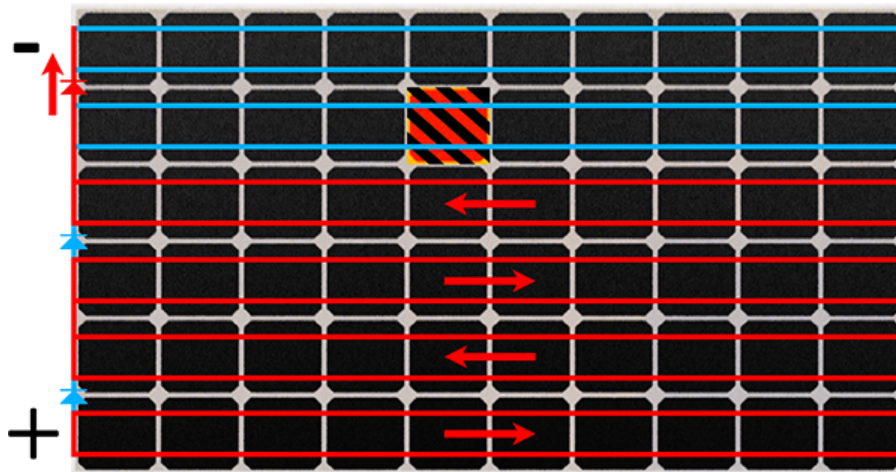


Figure 2.1.4: Example of photovoltaic module with an active bypass diode, caused by a cell-fault. The current flow, and active circuit is marked in red, while the inactive is marked in blue.

## 2.2 Photovoltaic Systems

Extending outside an individual PV-module, systems of series and/or parallel connected modules are most often used in larger solar generators. In this case, there may be several modules in strings of a certain length, in parallel with other strings, to ensure the wanted voltage and current through each set of modules. Each string is also often accommodated by their own fuse to moderate the risk of over-current. Expanding with several of these sets enables the solar farm to capture more solar energy. [2]

### 2.3 Sensors for Characterisation

When performing tests on PV-modules, a reference of the incident irradiance and module temperature is needed. The measurement of the incident irradiation can be performed either by a pyranometer, or a cheaper reference cell. The measurement module with a reference cell sometimes consists of several types of reference cells, relating to different types of PV-modules, for example multi-crystalline- or mono-crystalline silicon cells. The module temperature may be measured by means of a temperature-probe, which is mounted on the back-side of the module. To perform a proper characterisation of the module's IV-response, most measurement apparatus also requires an incident irradiation of at least  $500 \frac{W}{m^2}$ , to generate a viable result. This means that this kind of testing is also very reliant on acceptable weather conditions. The better the conditions, the better characterisation can be made and is easier to compare to the characterisation done under standard test conditions. [2]

### 2.4 Standard Test Conditions

Per the IEC 61853:2011-standard, standard test conditions (STC) for photovoltaic cells are defined as AM 1.5 irradiation spectrum, with a radiation intensity of  $1 \frac{kW}{m^2}$ , and a cell temperature of  $25^{\circ}C$ . One purpose of testing under STC is to determine the impact irradiance and temperature have on the PV-module's performance. The performance of the PV-module, under normal conditions, is affected linearly by the cell temperature and its incident irradiance. [19]

Figure 2.4.1 shows the AM 0, global AM 1.5, and direct AM 1.5 spectra as defined by the ASTM G173-03. AM 0 is the irradiance spectrum from the sun as before it is affected by the earth's atmosphere. The two AM 1.5 spectra are adjusted for absorption, scattering, reflection, etc. as the sunlight would travel through 1,5 times the thickness of the atmosphere. The global AM 1.5 spectrum is defined for use with flat PV-modules, while the direct AM 1.5 is defined for use with solar concentrators. These two are separately defined since the concentrators rely heavily on direct irradiance from the sun, while flat PV-modules may also benefit from indirect irradiance. The power concentration of AM 0, global AM 1.5, and direct AM 1.5 spectra are  $1366,1$ ,  $1000$ , and  $900 \frac{W}{m^2}$ , respectively. [20, 21]

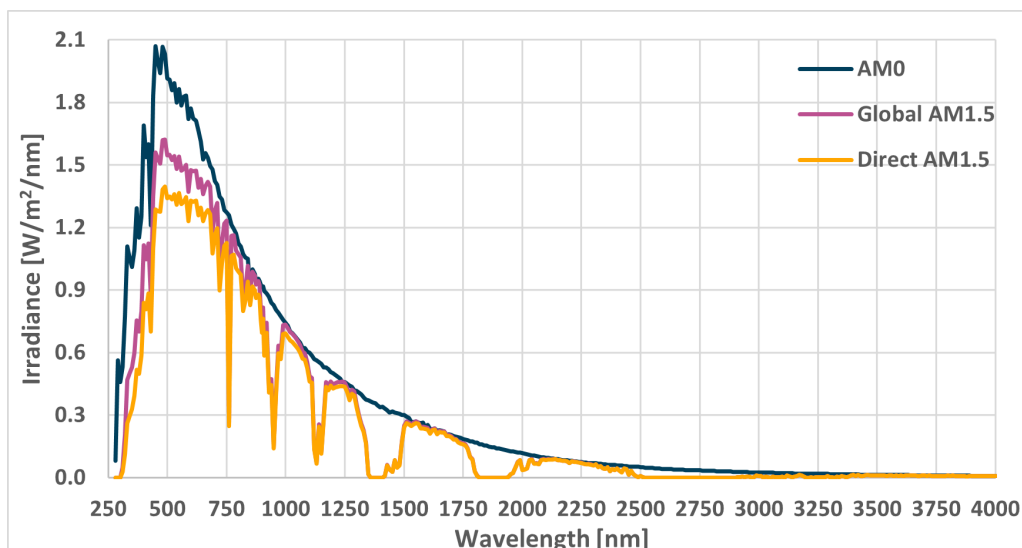


Figure 2.4.1: AM spectra compiled from data by National Renewable Energy Laboratory [3].

## 2.5 Infrared Thermography Imaging

Infrared (IR) thermography (IRT) is a contact-less and relatively safe method of conducting inspections of PV-modules in a way that is impossible to do with the naked eye. By use of IRT-imaging, some faults in relation to the PV-module can be detected in the early stages. With a known emission coefficient of a given surface, the temperature of the surface is possible to determine by measurement of the infrared radiation. The emissivity of PV-modules are not easily determined, as Kurnik et al. found, measured results vary between 0,6 – 0,92 [22]. IEC-standard 62446-3:2017 states that glass panels have an emissivity coefficient of around 0,85 – 0,9, being a function of the viewing angle. A typical plot of emissivity as a function of the *reflected temperature*<sup>3</sup>, and angle relative to the module plane, is shown in Figure 2.5.1 [4]. Infrared thermometers work by detecting the radiation of a single point of a surface, while the thermographic camera utilises an array of sensors which generate a two-dimensional thermographic picture. [2, 24]

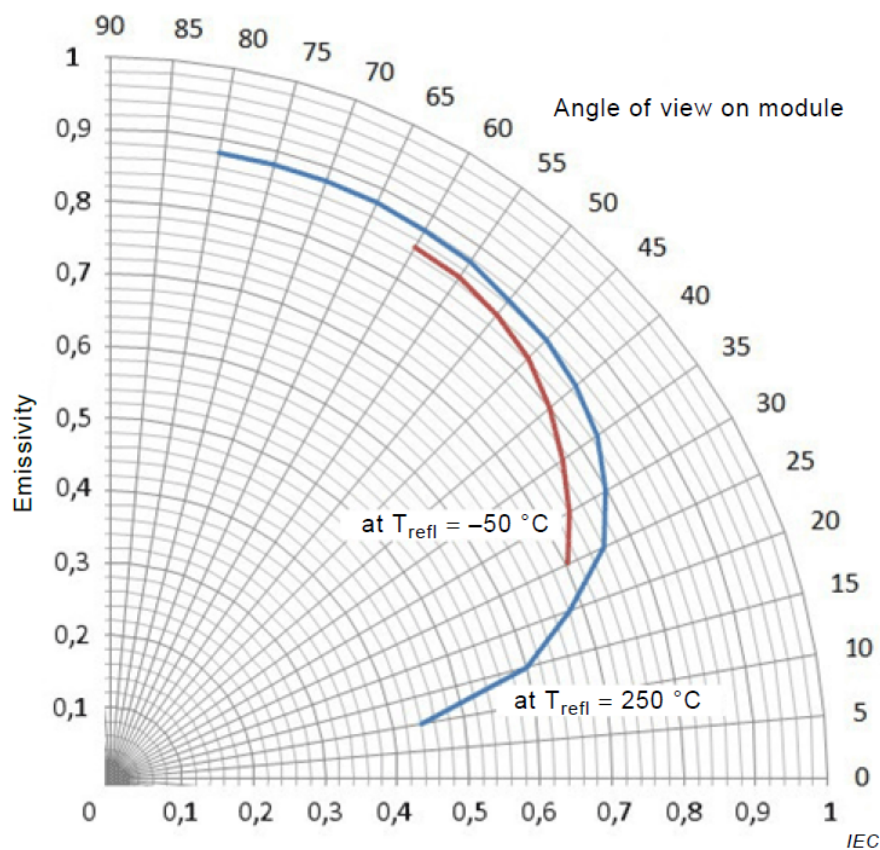


Figure 2.5.1: Emissivity relative to the viewing angle of a photovoltaic module and the reflected temperature [4].

There are two different methods of IRT-imaging of PV-modules, bright- and dark thermography. Bright thermography is recognised as being a temperature analysis of PV-modules which are exposed to direct sunlight. For diagnostic purposes, an irradiance level of at least  $500\text{ }\frac{\text{W}}{\text{m}^2}$  is required. Running the PV-modules in short-circuit mode will increase the temperature in the problematic areas of the module, making it easier to detect faults. Dark thermography is done by running a high reverse current, up to two times short-circuit current, through the panel in a dark laboratory. In this setting, areas with high contact resistance with the contact fingers will heat up significantly

<sup>3</sup>Reflected temperature (also known as background temperature or T-reflected) is any thermal radiation originating from other objects that reflect off the target you are measuring."- Teledyne FLIR LLC [23]



compared to the areas with low contact resistance. Thermography in a laboratory also allows for measurements of the backside of the panel, where it is easier to get sharper images of the temperature gradients in the module. Testing in a laboratory also eliminates the module stands, which may hinder a full view of the backside of the panel. PV-modules mounted on stands may also limit the possibilities of satisfactory viewing angles for the imaging. Understanding how different faults and problems affect the local temperatures of a PV-module, makes thermography an effective tool to detect and diagnose different issues in the given module. To mitigate the problems caused by sunlight reflecting off of the glass pane on the PV-module, a viewing angle of 5-60° off normal is recommended. [2, 24]

Recommended viewing angle is further illustrated in Figure 2.5.2, for clarification, where the green area is within the recommended angle. IEC standard 62446-3:2017 however, recommends a viewing angle as close to normal on the module plane while avoiding reflections of self, sun, etc. The type of camera used should also be considered in terms of pixel-resolution, noise, temperature range, and associated software for post-processing.

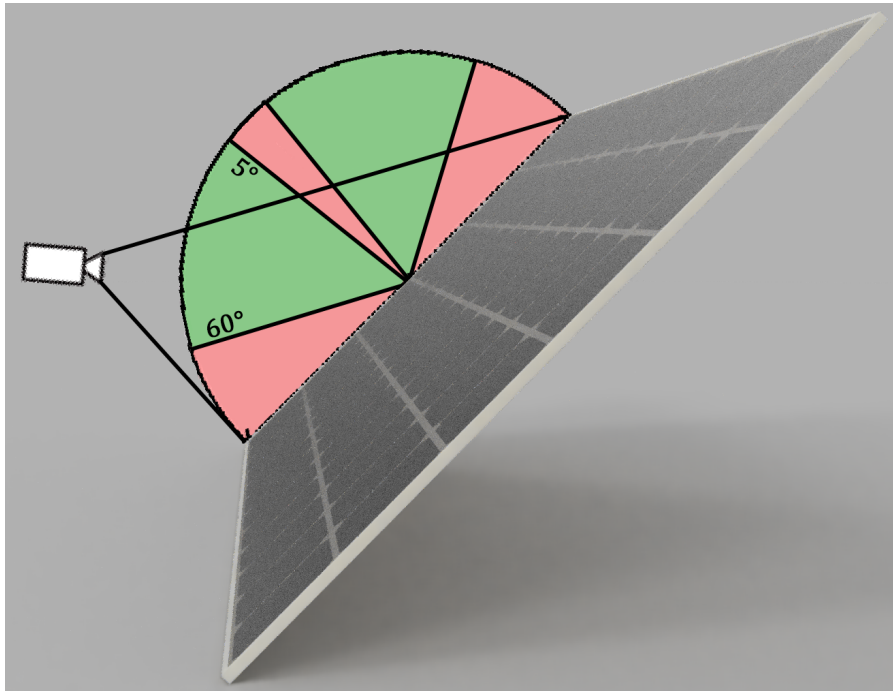


Figure 2.5.2: Optimal viewing angle for infrared thermography.

## 2.6 Electroluminescence Imaging

Electroluminescence (EL) imaging is a very helpful tool in uncovering faults in PV-modules. The basic principle of EL-imaging is to supply a short-circuit current to the PV-module, such as to make the module operate in forward bias. By doing this, the PV-module emits a weak stream of photons with wavelengths of about 1000-1200 nm. Since conventional camera sensors mostly operate outside this region, a camera with a purpose-built sensor might be needed to get satisfactory photographic data. Alternatively, a camera with filters can be used. [2]

The photon radiation from the module is a result of direct recombination in the cells. The more radiation from a given area indicates a higher operating efficiency than the ones with less radiation. Areas with low or no recombination are seen as dark areas in the EL-images, these areas are either very inefficient or defective. [25]

### 2.6.1 Camera

Typically, the detectors in digital cameras are light sensing pixels or semiconductors, which may be cooled by means of i.e. thermoelectric cooling. Keeping the detector cool may reduce the signal-to-noise ratio. Table 2.6.1 shows some examples of semiconductor-detectors and their useful detection bands. [11]

Table 2.6.1: Detectors and their applicable wavelengths [11].

<b>Detector</b>	<b>Sensitive Wavelength [nm]</b>
Germanium	800–1700
Indium-Gallium-Arsenic	700–2600
Silicon	300–1100
Indium-Arsenic	1000–3800

Parameters such as pixel-resolution, noise, quantum efficiency, and dynamic range are also important factors which should be taken into consideration when acquiring an EL-camera. The lens type chosen for the camera also affects how it can be used by affecting the work distance possible with the camera. The resolution of the camera also affects the resolution of the picture directly. An example of this would be a hypothetical camera with a resolution of 1000 by 500 pixels taking a picture of a PV-module with dimensions of 1 by 0,5 meters. In this example, the resolution of the picture would be 1 mm by 1 mm. Therefore, the camera should also be placed as close to the module as possible, while also keeping the lens axis normal to the module plane as shown in Figure 2.6.1. Higher resolution cameras may also require longer exposure periods, and if the picture is more compressed in the camera, it will take longer to transfer to the computer. [11]

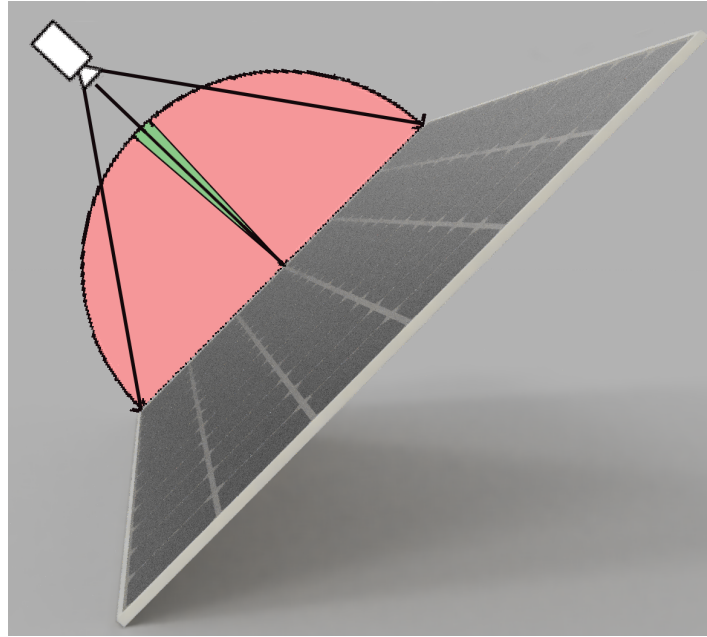


Figure 2.6.1: Optimum angle for electroluminescence photography.

All lenses used in EL-imaging should not contain any filters or coatings that may reduce the IR-photons near the band-gap of the semiconductor material in the PV-module. Optical lenses are sufficient in most cases, modules with lower band-gaps than 600 nm, however, require Germanium lenses. The choice of lenses, wide-angle or telephoto, may depend on how close or far from the module one wishes to place the camera. Filters may also be used to eliminate wavelengths outside the band-gap of the module in question. 850–950 nm long-pass filters may be used when EL-imaging a silicon PV-module. [11]

### 2.6.2 Daylight Imaging

While conventional EL-imaging is done in a dark laboratory, Alves dos Reis Benatto et al. [26] presented a drone-based system, which allowed for daylight EL-imaging. This system allowed for EL-imaging and detection of faults at the scale of disconnected cell regions larger than the irradiance variations caused by the crystalline nature of multi-crystalline Si-cells, at a rate of 120 frames per second. Usable EL-image results were obtained by post-processing the drone-images, wherein the images were processed by an algorithm which subtracted the background from the images, adjusted the perspective of the images by PV-module edge detection, and compensation for movement in the image sequence. Using both AC and DC modulation also served to improve the images of the modules, by avoiding irradiance interference from the sunlight. [8]

Kropp et al. [27] also utilised computer algorithms to perform EL-characterisation of PV-modules by use of a stationary near-infrared camera, and an accumulator bank which stored the energy from the PV-module and boosted the voltage before sending it back to the module to stimulate it for the EL-imaging. Both EL- and *photoluminescence*<sup>4</sup> (PL) images were used in the algorithm to achieve the quality required for characterisation.

<sup>4</sup>"Photoluminescence is a process in which a molecule absorbs a photon in the visible region, exciting one of its electrons to a higher electronic excited state, and then radiates a photon as the electron returns to a lower energy state." - Munson et al. [28]



## 2.7 Current-Voltage Testing

The daylight current-voltage (IV) test entails recording the current through a PV-module between  $V_{SC}$  and  $V_{OC}$  while the module is illuminated. The data recorded from this test contain most of the central information on the module's operating characteristics. The shape of the IV-curve can be used to spot faults or defects in the module. Figure 2.7.1 shows an example of a nominal IV- and PV-curve in orange- and purple colour, respectively. The PV-curve is calculated by

$$P(V) = I \cdot V, \quad (1)$$

where  $I$  is the current corresponding to the voltage,  $V$ . The peak of the PV-curve, where the power output is at its highest, is called the maximum power point,  $P_{MPP}$ . This point is a product of the maximum power point current,  $I_{MPP}$ , and -voltage,  $V_{MPP}$ . [2]

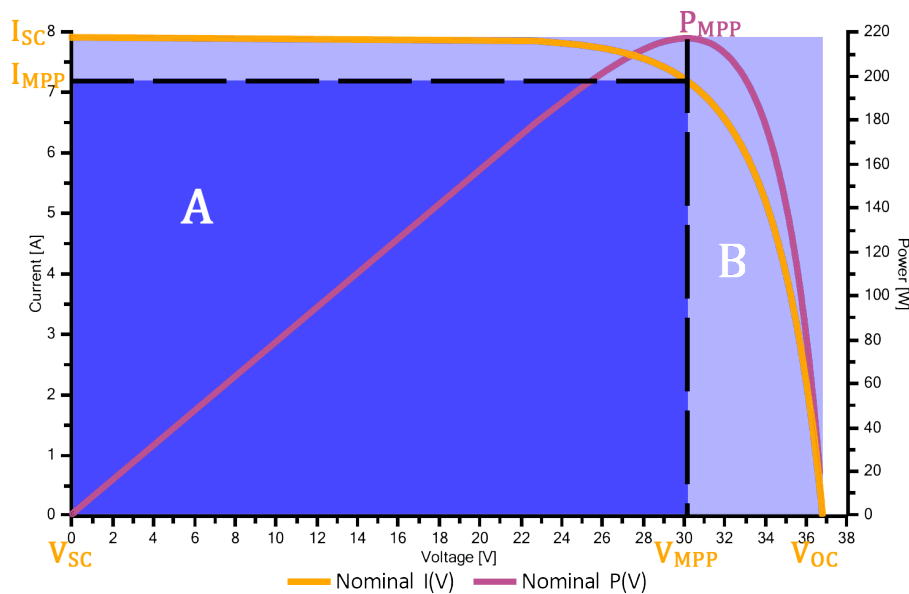


Figure 2.7.1: Example of a nominal current-voltage-, and power-voltage curve, with noted maximum power point, short-circuit voltage/current and open-circuit voltage.

The fill-factor (FF) is determined by the relationship between  $P_{MPP}$  and the product of  $V_{OC}$  and  $I_{SC}$ , as shown in 2.7.1 by area "A" and "B", respectively. This is a characteristic which essentially describes the efficiency of the PV-module. FF is mathematically expressed as

$$FF = \frac{V_{MPP} \cdot I_{MPP}}{V_{OC} \cdot I_{SC}} = \frac{P_{MPP}}{V_{OC} \cdot I_{SC}}. \quad (2)$$

The fill-factor is affected by several aspects. Some of the main characteristics affecting the FF is irradiance and temperature; increasing the irradiance raises both the  $I_{SC}$  and  $V_{OC}$ , while increasing the temperature mainly decreases the  $V_{OC}$ . [29]

## 2.8 Ultraviolet Fluorescence Imaging

Inspection of photovoltaic (PV) modules using ultraviolet (UV) fluorescence (UVF) relies on the fluorescence of the polymeric laminate the PV-cells are embedded in. The cells are typically embedded in ethylene-vinyl acetate (EVA), with varying amounts and combinations of oxidation stabilisers, UV absorbents, and/or polymeric crosslinkers. The fluorescence in a material is caused by the atoms in the molecules absorbing electromagnetic radiation, in this case, UV-radiation, wherein an electron is excited. When the electron subsequently returns to a lower energy band, a photon is released within a wavelength related to the atom and the level of excitation of the electron. [5]

A fluorophore is a chemical compound which is able to emit light in this process. They typically consist of one or more aromatic groups or other cyclic groups. These materials are often used as additives or products resulting from the degradation of the polymers. Figure 2.8.1 shows an illustrative example of where there is a buildup of UV-fluorophores in the laminate of the cell, with a case of photo-bleaching around the circumference of the cell. The bleaching is caused by molecules, such as oxygen and water, diffusing from/through the back-sheet of the module, reacting with electromagnetic radiation. The UVF can be measured using a UV-source and a spectrometer, which will result in a spectral UV-response from the material in question, along with the reflection of the UV-radiation

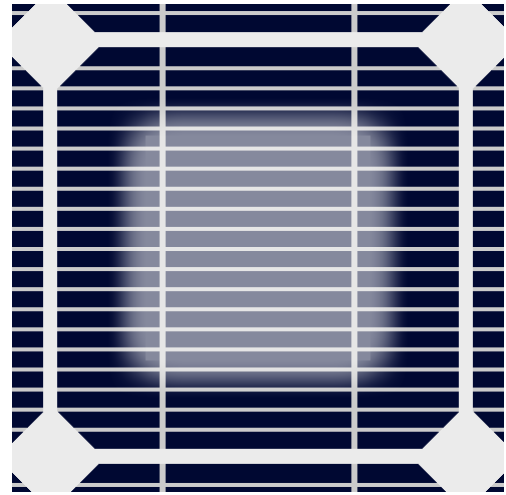


Figure 2.8.1: Illustrative example of ultraviolet fluorescent build-up and circumferential photo-bleaching.

from the source. This process only gives information about the UVF at a single point at a time. This thesis addresses the UVF of areas the size of PV-cells or -modules and will therefore not utilise this method. [5]

A simpler process is to use a normal camera with a sensor measuring outside the electromagnetic spectrum of the UV-source, with UV-irradiation of the whole module. The testing should be done in a dark environment, as to limit the effect external radiation has on the resulting image, in addition to the low amount of light being emitted from the module during the experiment. The impact on the results from the reflected UV-radiation can be minimised by the UV-source being outside the electromagnetic range of the sensor, or by filtering the electromagnetic range of the source. The UV-source's most often used in these experiments are within the wavelength range of 350–380 nm, accompanied by a low-pass filter on the camera. If UVF test of the glass plates is to be done, one could use a 254 nm-, or >350 nm source in the case of modern glass containing tin-oxides, or older Cerium-coated glass, respectively.

The intensity of the UVF-response of the encapsulating polymer in a PV-module increases with the duration of the lamination process. Wherein, it is correlated to the byproducts from the additives, and cross-linking activators in the polymer. However, these fluorophores lose most of their fluorescent properties within the first days of exposure to sunlight. Further in the lifetime of the module, it was found that oxygen and/or water would diffuse through the back-plate of the module. The oxygen and water would then, together with external UV-radiation, cause "photobleaching" of the fluorophores in the EVA-laminate. In the case of cracked cells, this process also takes place as illustrated in Figure 2.8.2. [5]

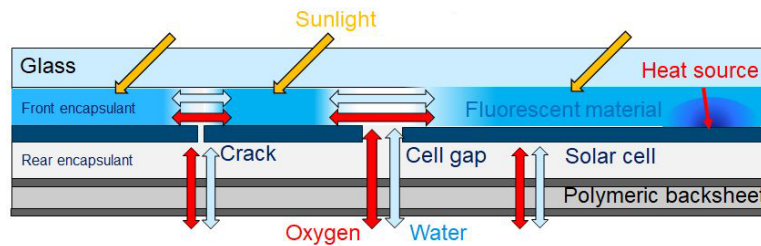


Figure 2.8.2: Representation of how ingress of oxygen and water, as well as hot-spots affect the ultraviolet fluorescence response of a photovoltaic module [5].



### 3 Literature Review

Some parts of this literature review are quoted from H. S. Ljosland's "Power loss estimation of different PV-module faults" [1].

#### 3.1 Current-Voltage Testing

Figure 3.1.1 shows some examples of how abnormal ageing, bypass-diode on, and short circuit may affect the IV-curve, as presented by Huang et al. [6]. As described in Table 3.1.1, abnormal ageing increases the  $R_S$  and decreases the  $V_{MPP}$ , bypass-diode on decreases the  $V_{MPP}$ , and the cell/string short circuit decreases the  $V_{OC}$  and  $V_{MPP}$ . All of these faults result in a reduced FF to a varying degree, while the  $I_{SC}$  remains unaffected, in reference to the normal operation. [6]

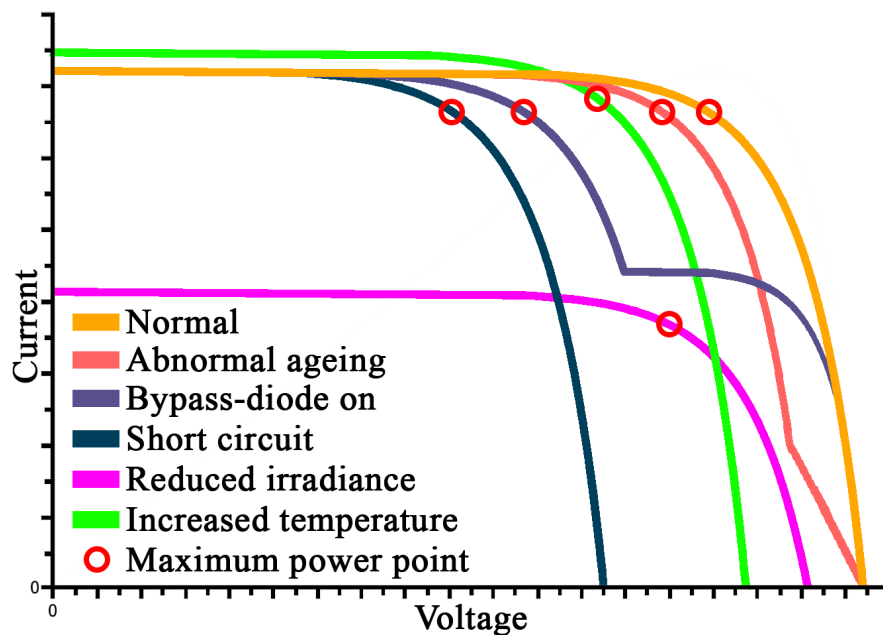


Figure 3.1.1: Examples of different faults or other performance altering conditions, and how they affect the current-voltage curve [6].

Table 3.1.1: How examples of faults, or other performance altering conditions, affect the IV-characteristics [6].

Fault type	$V_{OC}$	$I_{SC}$	$V_{MPP}$	$I_{MPP}$	$R_S$
Abnormal ageing	—	—	↓	—	↑
Bypass-diode on	—	—	↓	—	—
Short circuit	↓	—	↓	—	—
Reduced irradiance	↓	↓	↓	↓	—
Increased temperature	↓	↑	↓	↑	—

The actual, full, efficiency of the PV-module is given by the maximum power point power,  $P_{MPP}$ , per the irradiated power on the module,  $P_{Opt}$ . The open-circuit voltage is defined as the voltage between the two poles of the module, while the circuit is not connected. The short-circuit current is defined as the current through the module while the poles of the modules are short-circuited.

The IV-curve will also be affected in the event of a change in the shunt resistance,  $R_{Sh}$ , or the series resistance,  $R_S$ , of the standard model equivalent circuit of the PV-cells as illustrated in Figure 3.1.2. The equation for the characteristic curve using the standard model is given in Equation 3, where  $I_0$  is the output current,  $V_0$  is the output voltage,  $I_{Ph}$  is the photocurrent,  $I_D$  is the current through the diode,  $m$  is the ideality factor, and  $V_T$  is the thermal voltage;

$$I_0 = I_{Ph} - I_D \cdot \left( e^{\frac{V_0 + I_0 \cdot R_S}{m \cdot V_T}} - 1 \right) - \frac{V_0 + I_0 \cdot R_S}{R_{Sh}}. \quad (3)$$

The thermal voltage is defined as

$$V_T = \frac{k \cdot T}{q}, \quad (4)$$

where  $k$  is the Boltzmann constant,  $8,6175 \cdot 10^{-23} \frac{eV}{K}$ ,  $T$  is the temperature, in Kelvin, and  $q$  is the elementary charge,  $1,6022 \cdot 10^{-19} As$ . The photocurrent is given by the product of the spectral sensitivity of the cell,  $S(\lambda)$ , and the optical power hitting the cell;

$$I_{Ph} = S(\lambda) \cdot P_{Opt} \quad [2]. \quad (5)$$

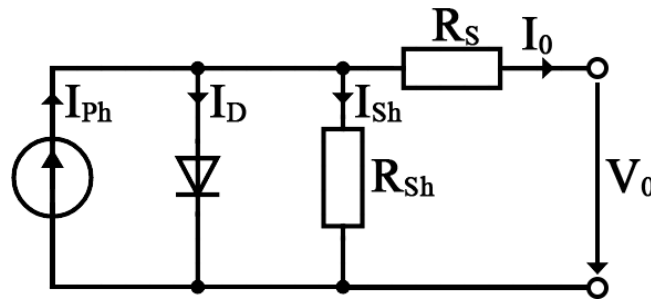


Figure 3.1.2: Standard equivalent single diode circuit of photovoltaic cell, or -module [2].

Figure 3.1.3 shows an illustrative example of the IV-curve response with a change in unit-less  $R_S$ . Using the curve with the lowest  $R_S$ , it is clear that increasing the resistance mainly causes  $V_{MPP}$  to decrease, until it goes far enough to decrease  $I_{SC}$  [2]. It is also clear that a change in  $R_S$  does not affect the  $V_{OC}$ .

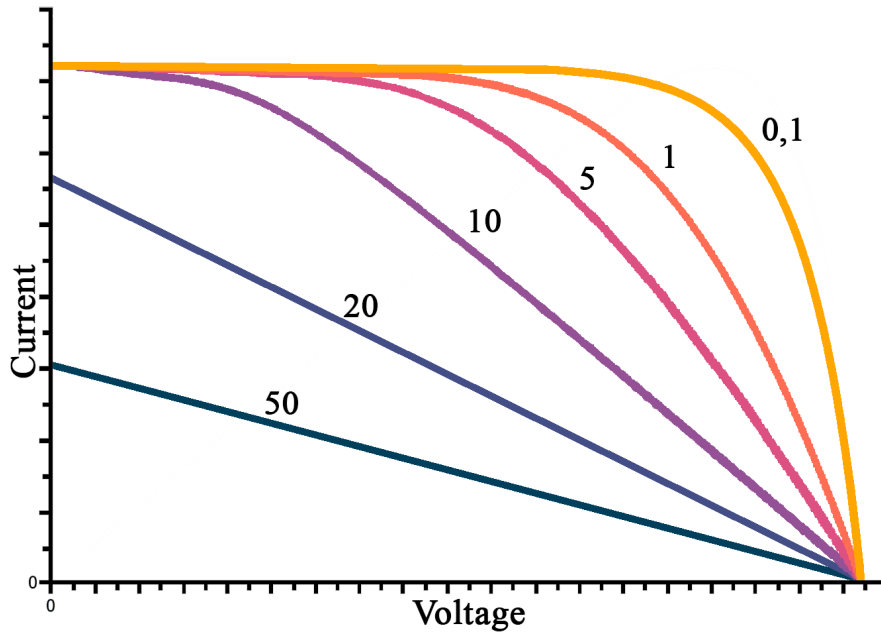


Figure 3.1.3: Current-voltage curve response with varying series resistance [6].

Figure 3.1.4 shows an illustrative example of the IV-curve response in the case of change in a unit-less  $R_{Sh}$ . Using the highest resistance value as a reference shows that a decrease of the  $R_{Sh}$  mainly causes the  $I_{MPP}$  to drop, with a relatively low drop in  $V_{OC}$ . This is until the curve drops enough to cause the  $V_{OC}$  to drop significantly. It is also clear that change in  $R_{Sh}$  does not affect the  $I_{SC}$  [2].

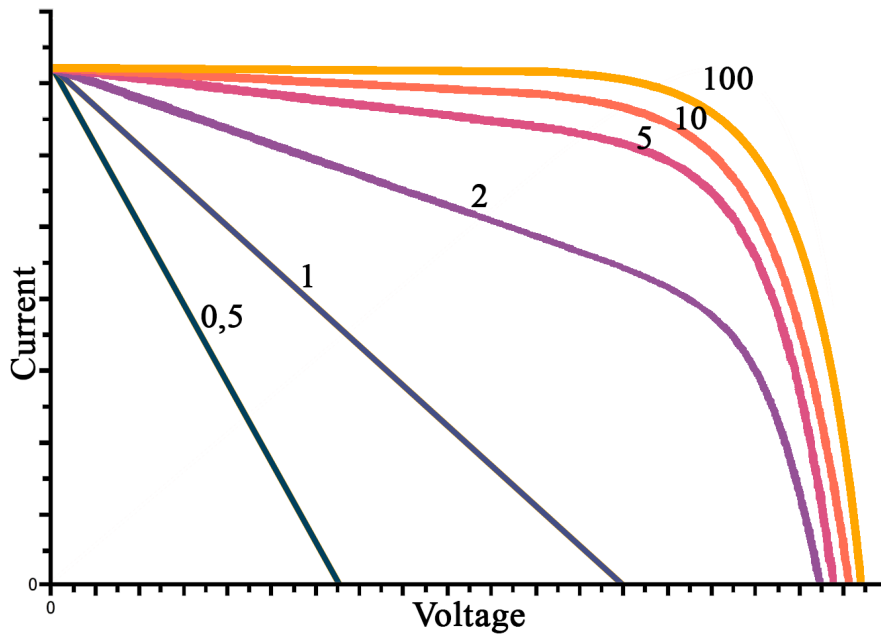


Figure 3.1.4: Current-voltage curve response with varying shunt resistance [2].

### 3.2 Infrared Thermography Testing

R. D. Isaksen performed continuous testing of several fault types over a couple of months, using IRT- and EL-imaging [30]. She found that mechanical defects in the PV-module only affected the production and temperature to a relatively small degree. She suggested that this might be remedied by performing more tests, to generate a sufficient foundation of data, and/or performing the tests during the summer months. This is because of the increased incident irradiation during the summer, causing more heating of the PV-modules. She did however create a framework and method for long-duration testing of PV-modules using IRT-imaging, and the corresponding methods for the testing procedure. Isaksen found that modules damaged by the use of a hammer caused a bypass-diode to activate, and the median temperature of the module to rise. Her results also suggest that it is the number of cracked cells that mostly affects the power production, not just the size of the cracks. [30]

The following review of Tanakas et al.'s work is quoted from "Power loss estimation of different PV-module faults" [1]. Tsanakas et al. [7] developed tables for use in fault detection of PV-modules, using illustrations of infrared (IR) imaging of three modules in series. Figure 3.2.1 shows the faults relating to the cells in terms of physical- and optical faults/degradation. Figure 3.2.2 shows faults not directly related to the cells.

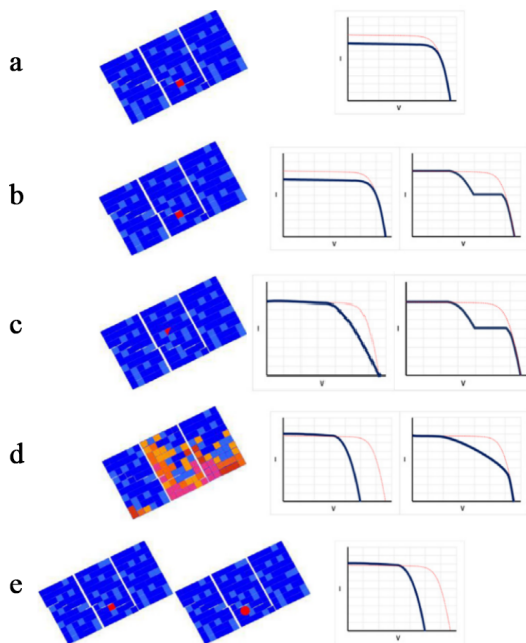


Figure 3.2.1: Table of infrared images and current-voltage curves correlated to different cell faults [7].

In Figure 3.2.1, case "a" shows an example of optical degradation of a cell. Here, there is one cell with a higher temperature than the others, and a drop in the short-circuit current,  $I_{SC}$ . They found that the power loss in this case is around 5% for issues with lamination, and around 10% for severe discolouration. The stress factor likely to cause these issues are high temperature and ultraviolet radiation.

Case "b" shows an example of a cell with cracks, micro-cracks or *snail trails*<sup>5</sup>. The amount of power loss in this case, heavily depends on the extent of the cracks and in which direction/pattern they run. An area of 8% inactivity will result in unacceptable losses, while 50% inactivity will trigger the bypass diode. The stress factors likely to cause such issues are thermal cycling or mechanical load.

Case "c" is an example of a piece missing from a cell, which has similar characteristics to the cracked cell, only with the missing piece showing increased temperature, instead of the whole cell. This fault causes an increase in series resistance,  $R_S$ , and the power loss is correlated to the size of the missing piece. The stress factors here are the same as in case "b". Both of case "b" and "c" shows typical signs of bypass-diode activation or drops in  $I_{SC}$  or  $V_{MPP}$ , respectively.

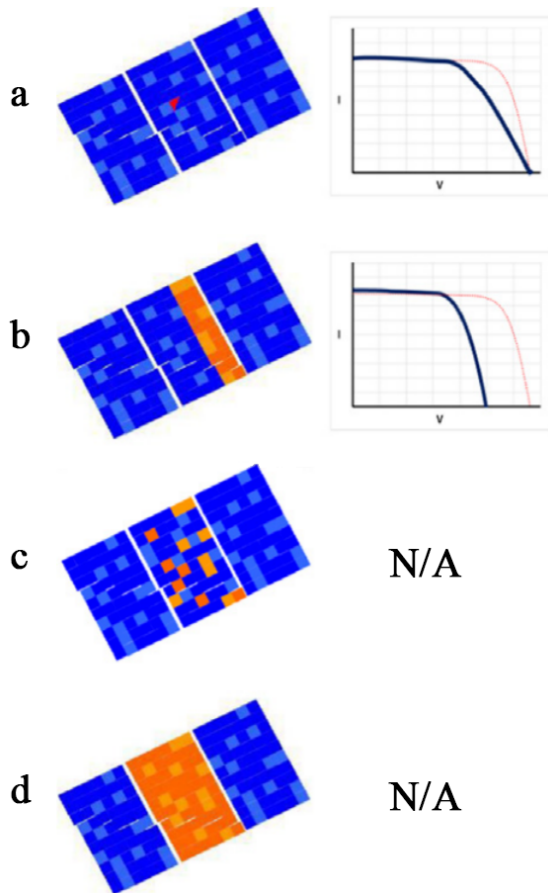
<sup>5</sup>Snail trails are discolourations of parts of the cell, caused by the ingress of contaminants in micro-structural cracks within the cell [31].



Case "d" shows an instance of *potential induced degradation*<sup>6</sup> (PID), which is most detectable at moments of low incident irradiation. The IRT-images show large areas of high temperature. The temperature difference in the module is higher for cases of medium degradation, compared to cases of more severe degradation. The power loss is up to 100 %, but the module is, in most cases, easily recoverable by applying a reverse voltage across the module. The amount of loss is dependent on the PV-module configuration. The IV-response shows either a drop in  $V_{OC}$  or both  $V_{MPP}$  and  $I_{MPP}$ . Stress factors are temperature, relative humidity, and electrochemical reactions.

The last case shows an example of shorted- or shunted cells, with a temperature difference lower than other fault types. As seen in the IV-response, there are negligible losses in the currents, but a significant drop in  $V_{OC}$ . The power loss in this case is directly correlated with the number of shunts in the module. The stress factors here, are thermal cycling and mechanical load.

Tsanakas et al. [7] also developed the table in Figure 3.2.2, which shows the thermal images and the corresponding IV-curves of different cases of circuit faults.



The first case shows an example where the connections between two cells are broken, to some degree. This kind of fault causes a very high temperature difference in parts or the whole of the cell in question, depending on the number of broken ribbons. In the case of an open circuit between the cells, the bypass diode would enable. The power losses are drastic for each of the broken ribbons, up to 30–50% loss. The fault is usually caused by thermal cycling or mechanical load.

Case "b" shows an example of a string in open-circuit with a defective bypass diode, or an internal short. The thermal response is a moderate, but uniform, temperature difference across the whole string or sub-string. The voltage loss in this case is according to

$$\Delta V = 1 - \frac{\text{Number of faulty strings}}{\text{Total number of strings}} \quad (6)$$

Case "c" is an example of all bypass diodes being shorted because of incorrect connections. This case gives a non-specific pattern of heat, with nearly 100% voltage loss. It is impossible to get an IV-curve in this

Figure 3.2.2: Table of infrared images and current-voltage curves correlated to different circuit faults [7].

condition, as is the case with the last example in the table.

The last case is an example of a module in open-circuit. The thermal images show low to moderate temperature difference, uniformly across the module. In this case, the module might be fully operational, but is not connected properly. The three last examples in this table are caused by electrical circuit faults.

<sup>6</sup>Power reduction caused by a high  $\Delta V$  between ground and module cables, causing  $\text{Na}^+$  ions to shunt the p-n junction in the cell [2].

### 3.3 Electroluminescence Testing

While some faults in PV-modules can be detected by the use of IRT- or EL-imaging, some are only detectable by the use of each method. As for the example of potential induced degradation and cracked cells, which are the most common defects, can be diagnosed by use of both methods but are more easily detected by the higher detail images of the EL-method. [32]

By subjecting PV-modules to excessive mechanical stress by hammer, Jensen [25] found that cracks parallel with the bus-bars caused significant reductions in power output. These cracks and efficiency measurements were done by use of EL-imaging along with IV-tracing, respectively. Jensen also found that the cracks developed over time, causing a further decrease in the power output of the module. There was also presented evidence pointing to cracks normal to the bus-bars having negligible losses when compared to that of the parallel cracks. These results correlate to the active area in the cells being reduced significantly more in the case of the parallel cracks. [25]

While comparing two modules with cracked cells, where one had cracks in the protective glass, Jensen found that the cracks in the module with cracked glass developed to be less efficient significantly faster than that of the module with cracked cells but intact glass. This suggests that exposure to the external environment would cause a faster degradation of the module's performance. [25]

Some types of PV-module faults are documented with electroluminescence (EL) photography by Fuyuki et al. [8]. A baseline test was done for both mono-, and multi-crystalline Si-cells, shown in Figure 3.3.1. As is evident, there are considerable differences in uniformity of the EL of the two types of cells, which is expected.

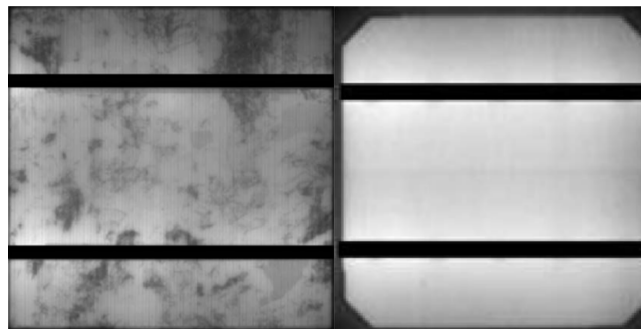


Figure 3.3.1: Mono- and multi-crystalline photovoltaic cells as seen using electroluminescence imaging [8].

Figure 3.3.2a shows an example of point-break cracks. They also captured an example of multiple faults in a mono-C Si-cell, depicted in Figure 3.3.2b. In this instance, there are both instances of a crack running approximately parallel with the bus-bars, marked by a red oval circle, and finger failures, marked in blue squares. This orientation of the crack is the most likely to affect the power production of the cell, whereas cracks perpendicular to the bus-bars are not as likely to affect the production [2]. This mono-C cell also shows signs of broken finger-contacts, marked with blue, dashed rectangles. This type of fault could either have been caused by damage from external sources, or because of a faulty printing process. Both of these instances showed no sign of fault with the use of conventional RGB photography, except for the broken finger contacts which were seen with a close-up image of one of the fingers. [8]

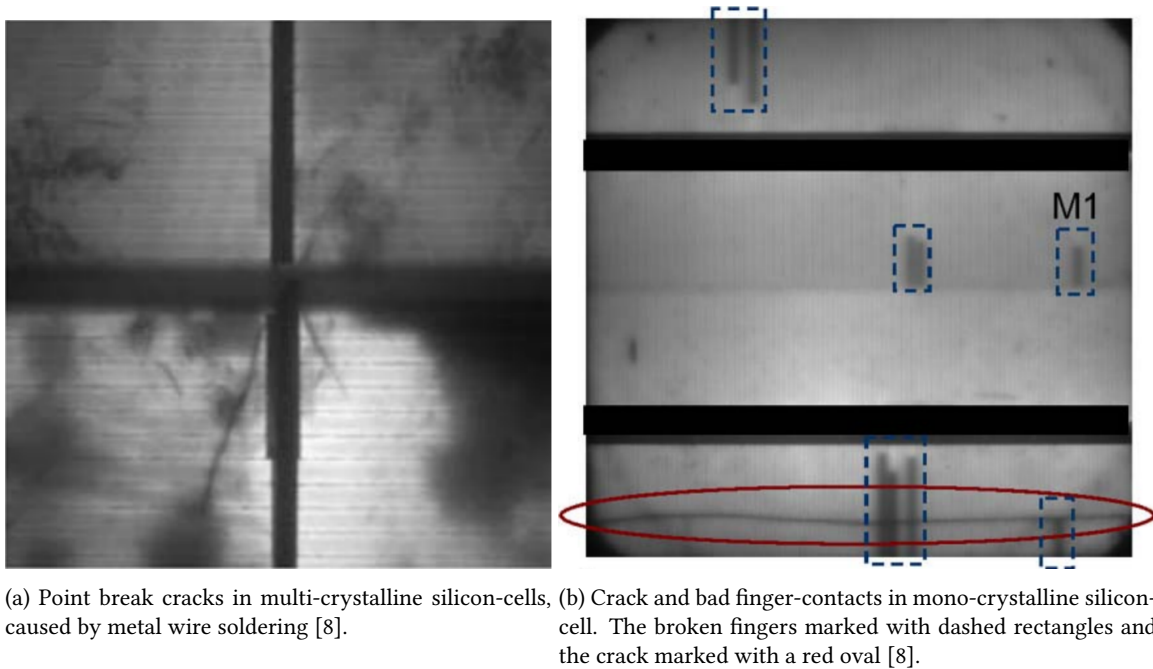


Figure 3.3.2: Two examples of electroluminescence imaging used for fault detection, not visible with conventional RGB photography [8].

Fuyuki et al. [8] also found there is a considerable difference in the EL-results of low- and high temperature in the case of the multi-C cell. Figure 3.3.3 shows the difference in result of a cell with a temperature of 25°C and 100°C, respectively. This may affect a hypothetical algorithm's ability to detect faults in multi-C PV-modules.

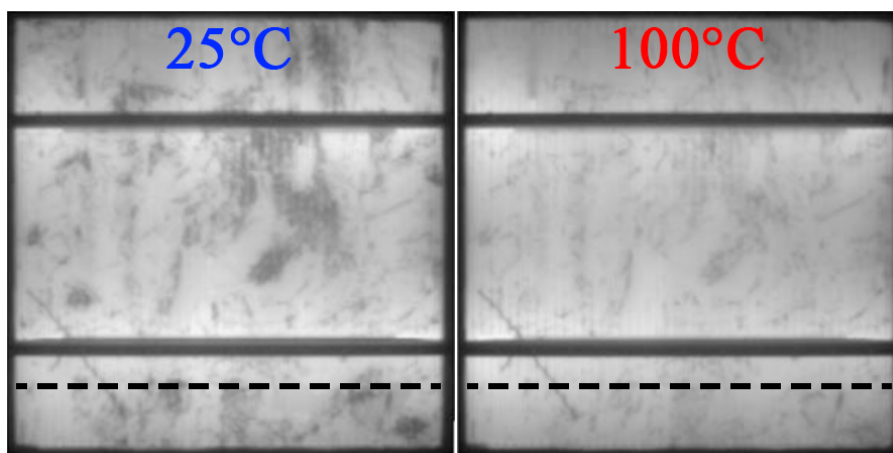


Figure 3.3.3: Internal cell temperature affects the visibility of the multi-crystalline grain boundaries [8].

The dashed line in Figure 3.3.3 shows where an EL-response intensity scan, from left to right, of the cell was made at both temperatures. The resulting plot of the scan is shown in Figure 3.3.4, where both the crack and the defect cluster on the right of the cell is highlighted. The red line represents the measurement done at 100°C and the blue represents the one made at 25°C. The brown line is the calculated difference between the two measurements. This difference suggests that the intensity does not change linearly, with less difference in the case of the crack and more difference in the case of the defect cluster at the right side of the cell.

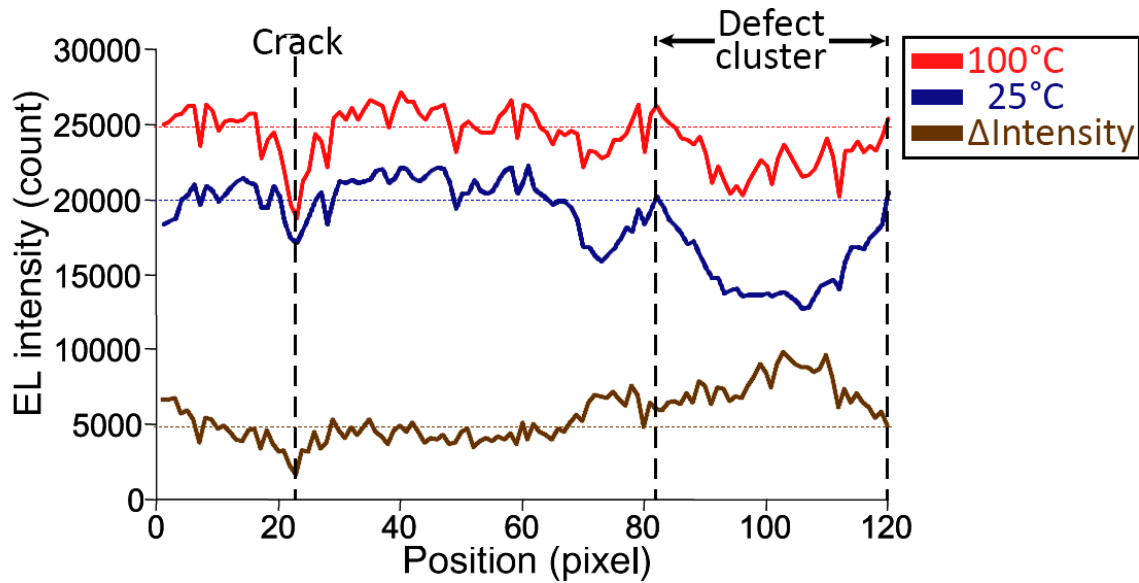


Figure 3.3.4: Electroluminescence scan of the dashed line in Figure 3.3.3, as well as the difference between the 100- and 25°C measurements. The scan was made left to right. [8]

Koch et al. performed a comparative study of outdoor EL-testing of on-site arrays of PV-modules, using manually moved camera stands and an unmanned aerial vehicle (UAV) [32]. In the case of the manual approach, there are several methods like boom-lifts, multi-camera tripods mounted to a section of the array at a time, or rail-based solutions. These manual methods were able to scan between 0,2 and 0,8 MWp per night. As for the approach of using a UAV, the wind speed plays a more significant role in the quality of the image results, and the energy density of the battery limits the flight time. The limited flight time also makes faster switching of the power supply to the modules more desirable, which could be done by wireless and/or autonomous systems. The combination of the UAV and the power supply switching allows for testing of 1 MWp per night, with fewer engineers needed. [32]

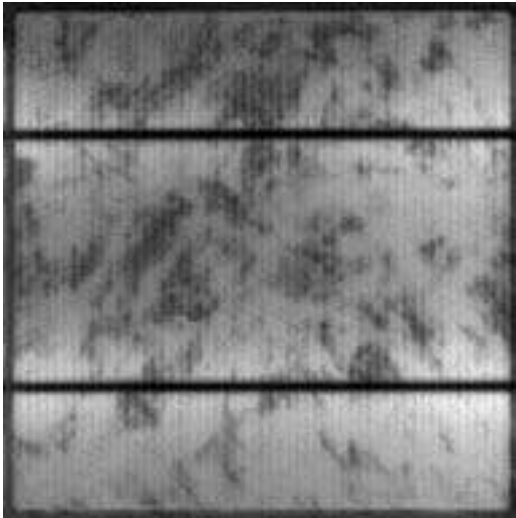
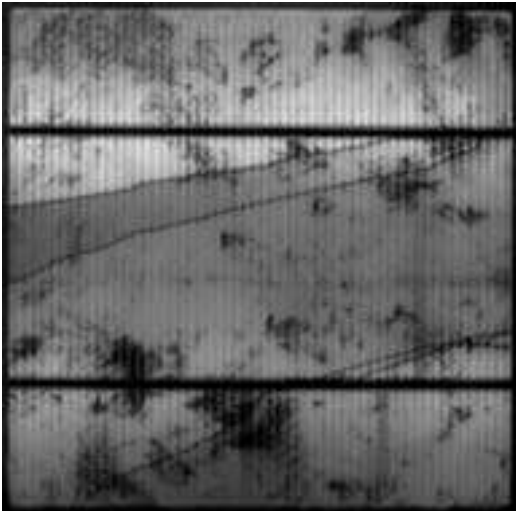
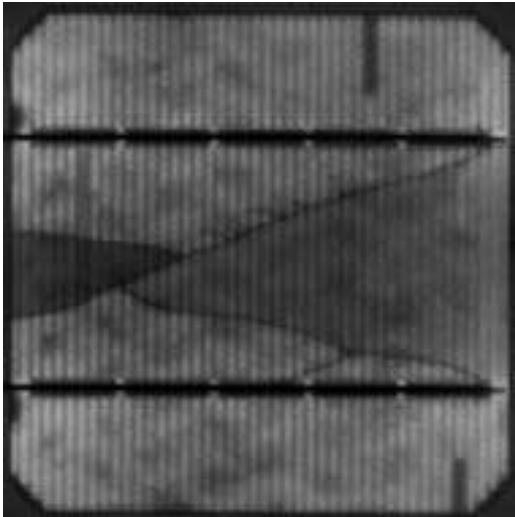
For analysis of large amounts of PV-modules the UAV-approach seemed to be the method with the best potential. However, the large amount of pictures taken, requires to be analysed using software-assisted data analysis. [32]

Köntgens et al. [12], in the IEA-PVPS T13-01;2014 report, found in-the-field EL-imaging is possible. Results of high quality may be obtained if two images are taken: one image without the applied DC-current and one with. In post-processing, the image taken without DC-current is then subtracted from the EL-image, resulting in none or minimal amounts of stray light. They also found that EL-imaging is a good method to identify cell-cracks or crystalline defects within the cells. Both would appear as a dark line on the EL-image, therefore no automatic system of detection had been satisfactory for fault detection. They also compounded a list of steps to identify cell-cracks from crystalline faults/grain-boundaries:

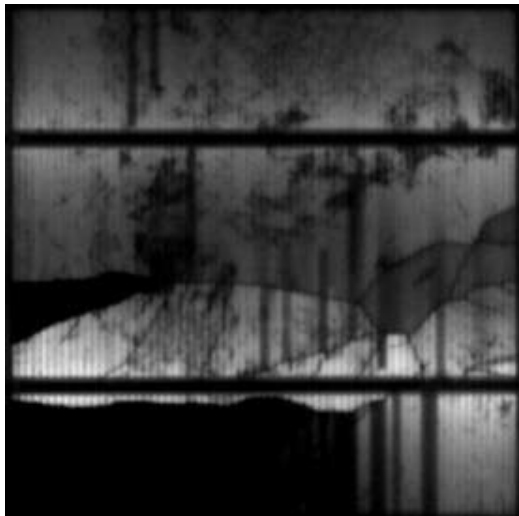
1. A cell-crack would appear, in the EL-image, as a dark grey line. The line would be of mostly constant width, and of a constant greyscale along the crack.
2. In the case of cell-cracks with an angle of  $\pm 45^\circ - \pm 5^\circ$ , relative to the fingers of the cells, would partly run parallel to the fingers. The cracks would then carry a resemblance to a step-function.
3. In the case of a sharp change in EL-intensity, it is most likely to be a crack.
4. The cracks most often appear from the busbars, cell-edge, or in the centre in the case of cross-cracks.
5. In the case of crystalline-defects, it might be able to identify them by comparing with neighbouring cuts from the silicon ingot. This is of course if they are present in the module in question. [12]

Examples of EL-images of known PV-module faults are shown in Table 3.3.1:

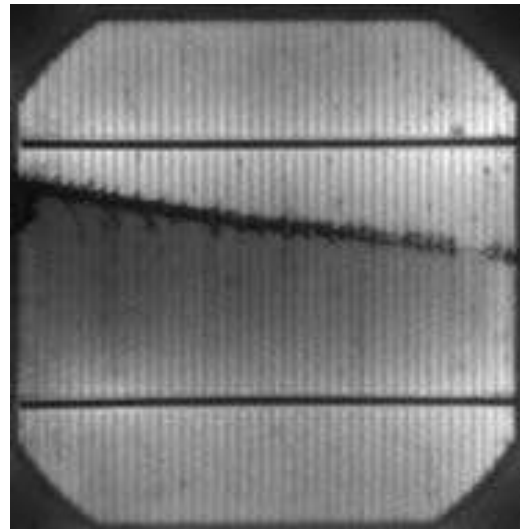
Table 3.3.1: Electroluminescence fault images from the IEA-PVPS T13-01:2014 report [12].

 <p>Normal multi-crystalline silicon cell.</p>	
 <p>Type A cell-crack. Cracks which do not isolate areas of the cell.</p>	 <p>Type B cell-crack. Cracks that create a significant drop of EL-response in an area of the cell.</p>

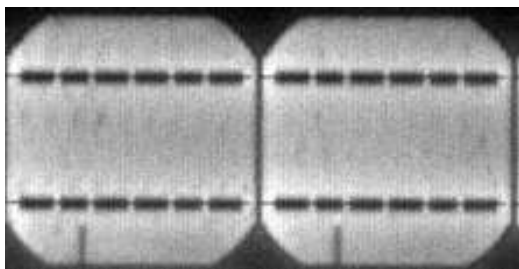




Type C cell-crack. Cracks which isolate areas of the cell completely, no EL-response from the affected areas.



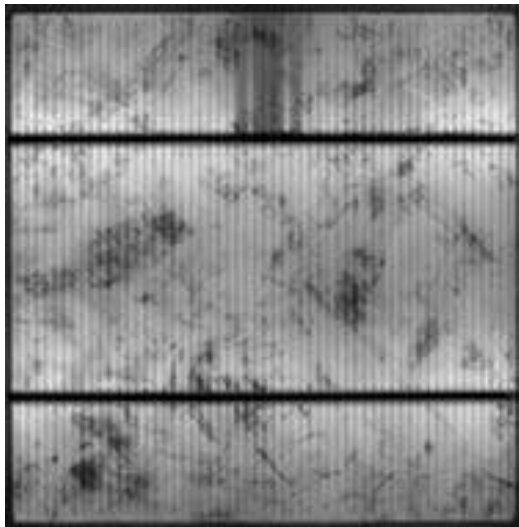
Cross-crack, spanning the width of the cell.



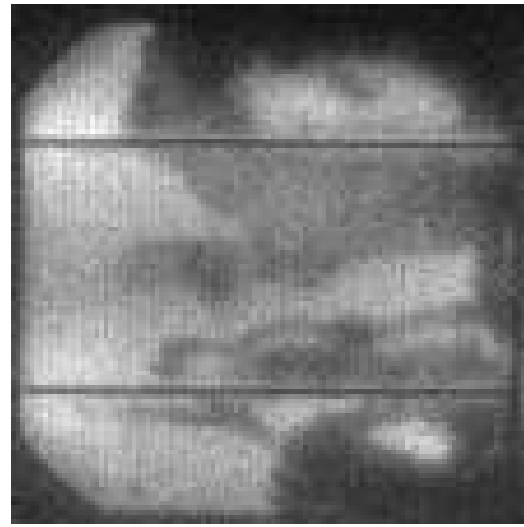
Finger fault from the edge of the cells (Type A). This case shows two cells with the same fault, which points to an issue in the production process of the cells.



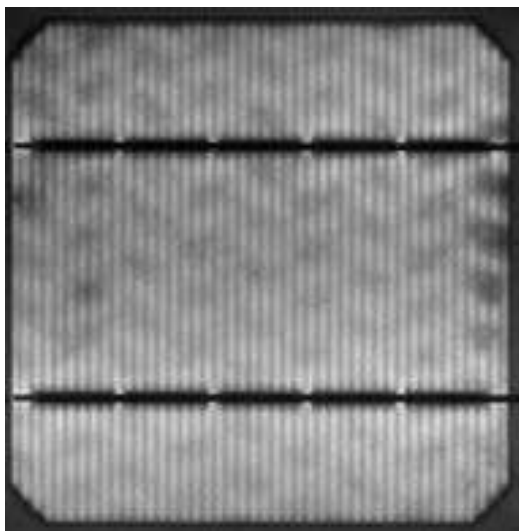
Finger fault type B, faulty finger connections caused by cell-cracks.



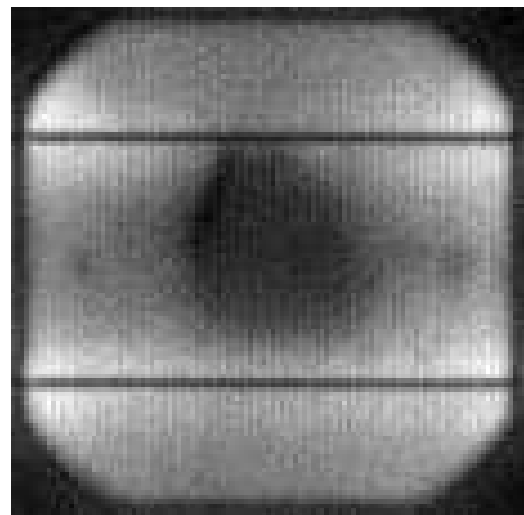
Finger fault type C, caused by improper soldering.



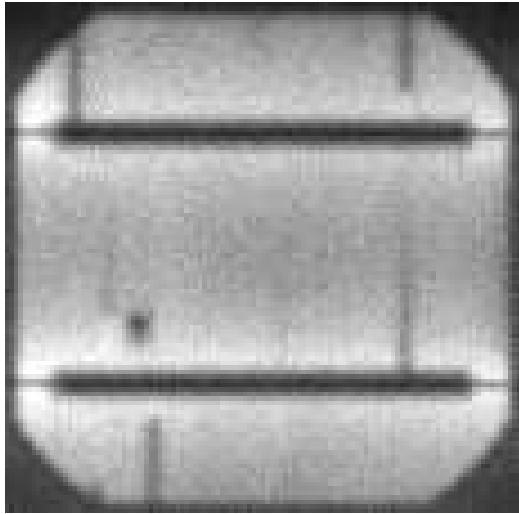
Humidity corrosion, caused by the ingress of water.



Contact forming failure A, caused by failed temperature homogeneity of the transport belt during the firing process.



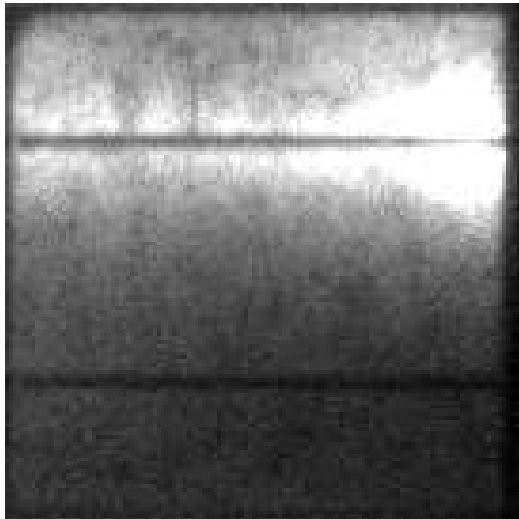
Contact forming failure B. Caused by failed temperature homogeneity during firing process, leading to contact resistance following a centre-edge gradient.



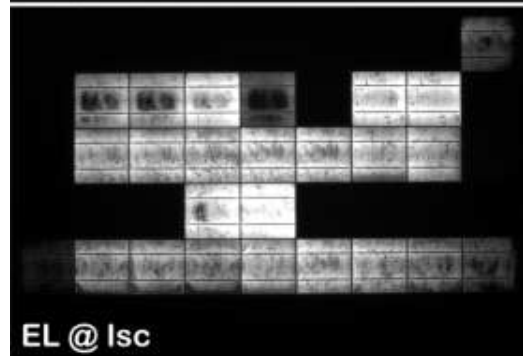
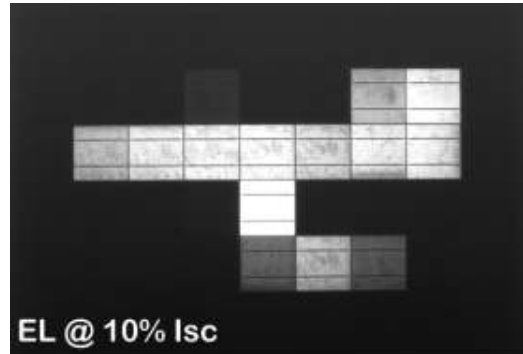
Solar cell shunt fault.



Interconnect shunt fault.

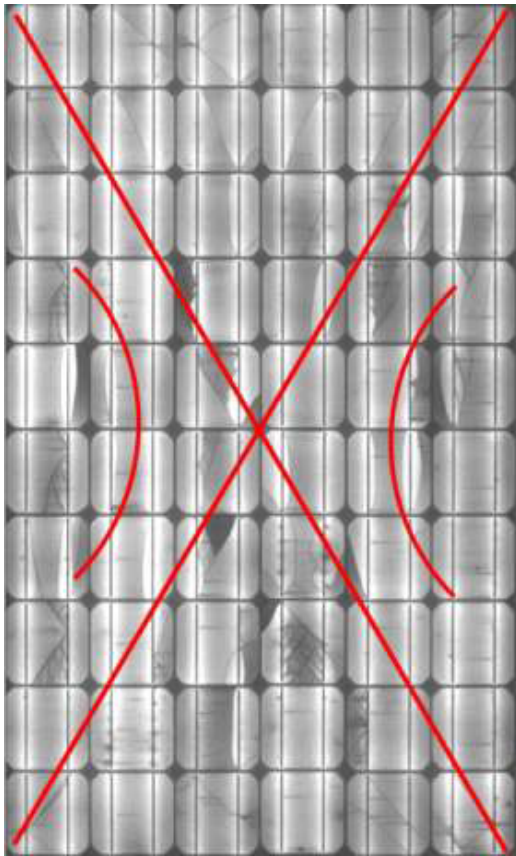


Interconnect disconnection.

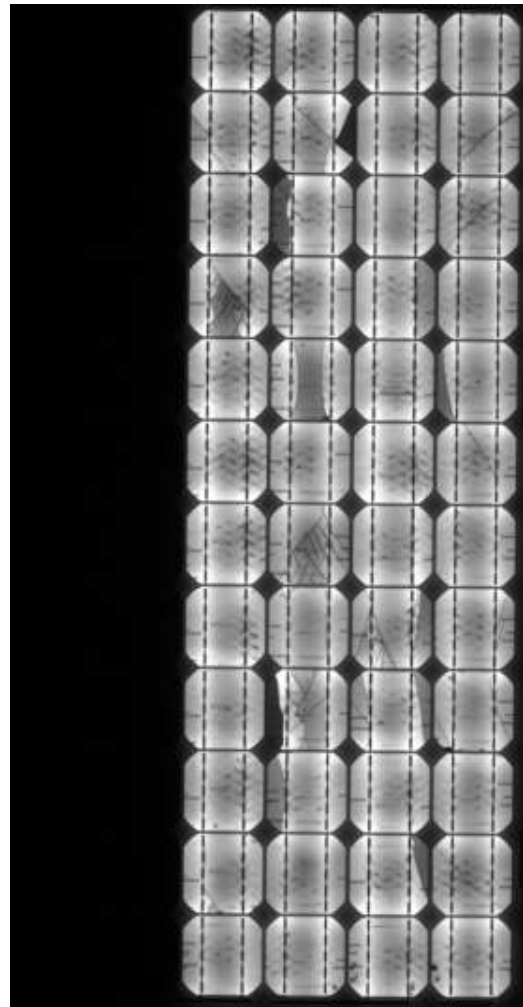


Potential induced degradation.





Cracks across whole module in a pattern suggesting the module having experienced a heavy mechanical load.



Bypass-diode fault, causing the disconnect of a sub-string.

### 3.4 Ultraviolet Fluorescence Testing

In a review of UVF assessment of PV-modules, Köntges et al. [5] found that the inherently long reaction time of the photobleaching process, made it possible to differentiate new and old modules by the difference in width of the circumferential photobleaching of the cell. Herein, the reaction time also allows for the assessment of the age of the cracks, based on the width of photobleaching emerging from the cracks. Figure 3.4.1 shows an example of EL- and UVF- response of a PV-cell, in which a cross-crack has developed. They found that the cracks show clearly in a cross-pattern in the EL-image, while appearing as a circular spot in the UVF-image. [5]

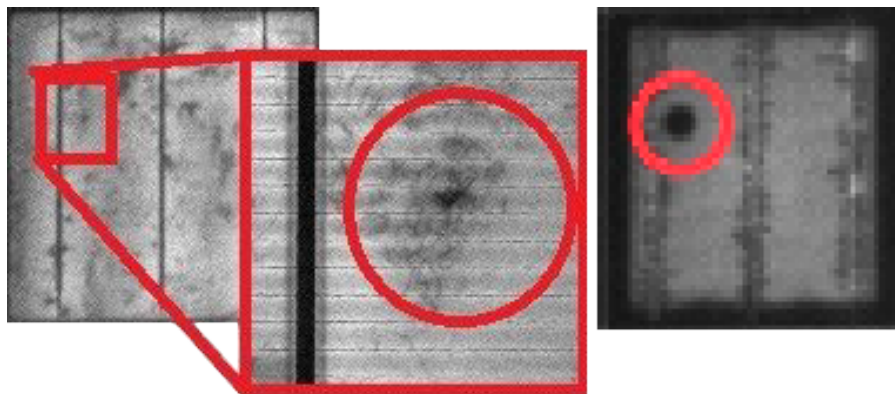


Figure 3.4.1: Electroluminescence- and ultraviolet fluorescence response of a photovoltaic cell with cross-crack fault [5].

Köntges et al. [5] found that a PV-module operating over a prolonged period of time, with widely differing cell-temperatures results in differing UVF-response from each cell. In this case, the cells which operated under higher temperatures showed a higher UVF-response than the cooler cells. Figure 3.4.2 shows their example, with the cell-temperatures of each cell measured with IRT, and the corresponding UVF-response. The red and green circles highlight the cells with one of the highest- and lowest operational temperatures, respectively. The UVF-test was done after the module had settled at ambient temperature. This corresponds with the theory presented in Chapter 2.8.

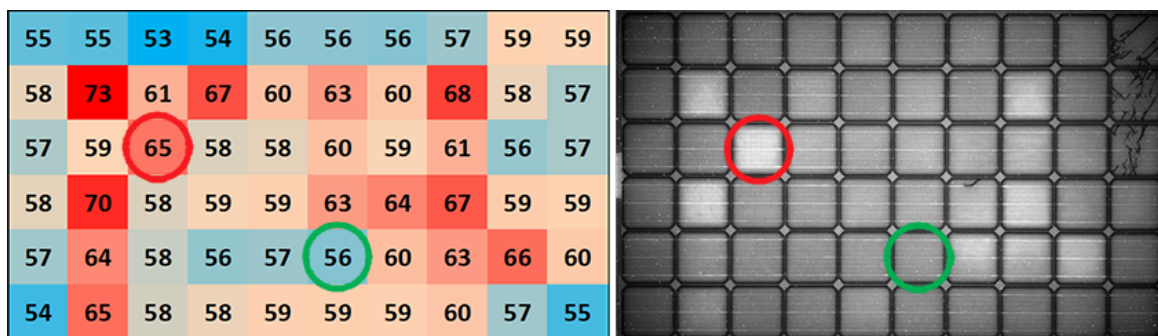
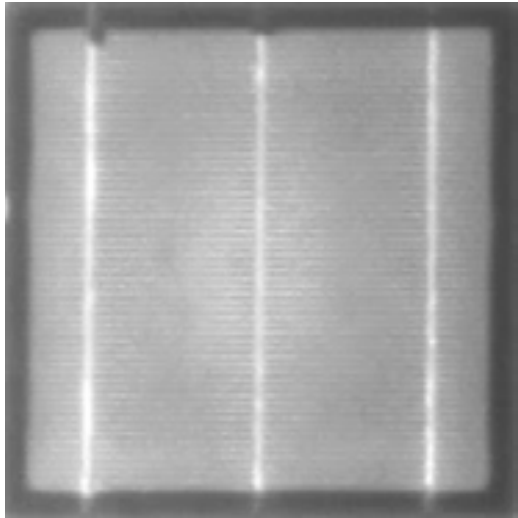
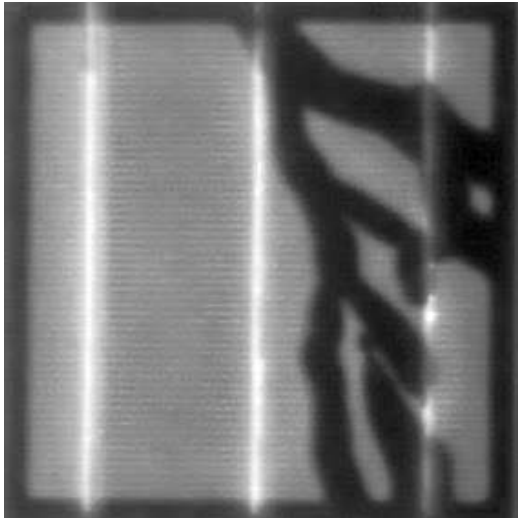
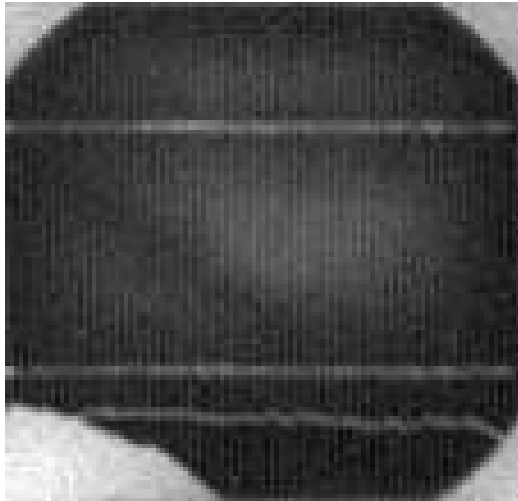
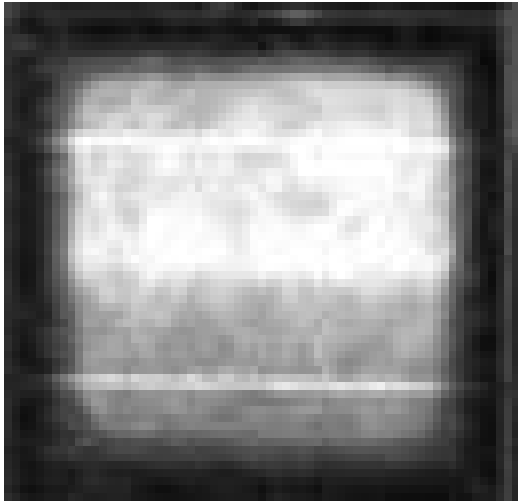


Figure 3.4.2: Cell temperatures and ultraviolet fluorescence response of a photovoltaic module with prolonged operation with varying cell temperature [5].

In the IEA-PVPS T13-01;2014 report, Köntges et al. [12] found that a PV-module has a more intense UVF-response the longer it is exposed to UV-radiation. The advised exposure amount was found to be around  $80 \frac{\text{kWh}}{\text{m}^2}$ , which would correlate to an exposure period of around 18 months in Germany. Table 3.4.1 shows their main findings of faults identified using UVF-images.

Table 3.4.1: Ultraviolet fluorescence fault images [12].

	
Cell with no failure. Photobleaching around the cell circumference.	Cracked cell, with photobleaching emerging from the cracks.
	
Isolated area of a cell.	Interconnect disconnection. Lopsided heating of the cell, because of one ribbon being disconnected, causes more fluorophores.

### 3.5 Optical Degradation

Segbefia et al. [9] (not yet peer-reviewed) used, among other methods, EL-, and UVF-imaging to identify optical degradation in PV-modules. During the analyses of several PV-modules, they found that optical degradation of the modules cause the EL-results to show small dark spots randomly distributed across the modules. For the UVF-results, the whole module shows a reduced UVF-response. Figure 3.5.1 a, and b shows two EL-images taken of the same module, at  $I_{SC}$ , and  $0,1 \cdot I_{SC}$  forward current, respectively. The highlighted area corresponds to an area where optical degradation has incurred.

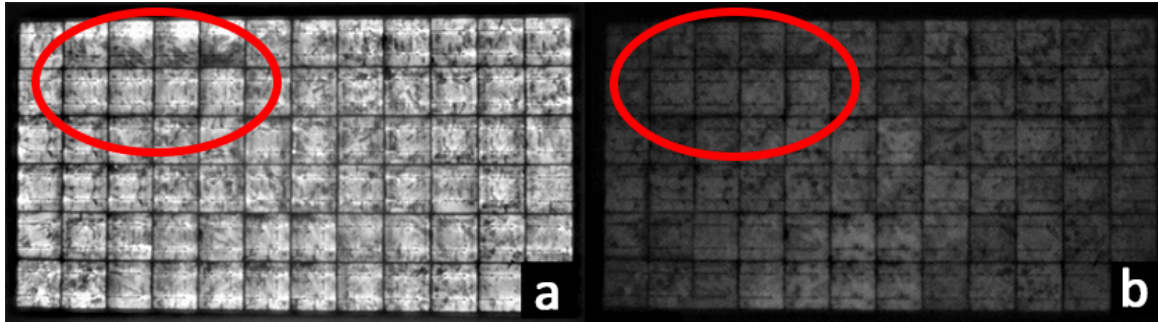


Figure 3.5.1: Electroluminescence image of a module with an area of optical degradation, at forward current of (a)  $I_{SC}$ , and (b)  $0,1 \cdot I_{SC}$  [9].

Figure 3.5.2 shows two images of two different modules, where (a) is a module with optical degradation across the whole module causing a low UVF-response. The module in image (b) is not afflicted by optical degradation, shown for reference.

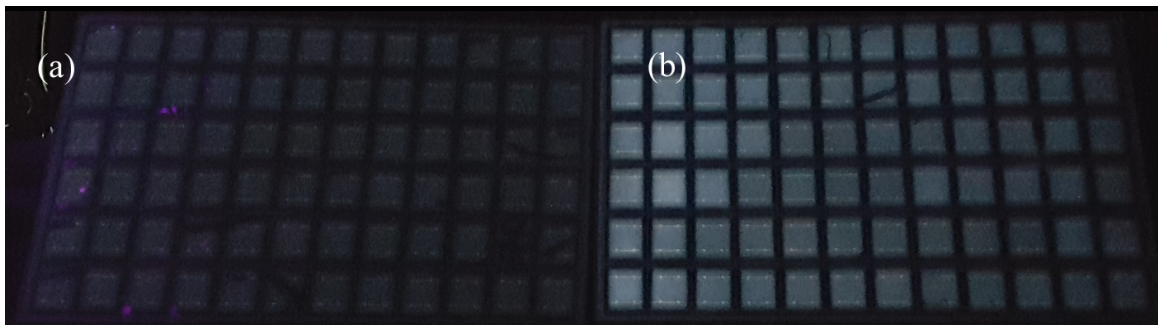
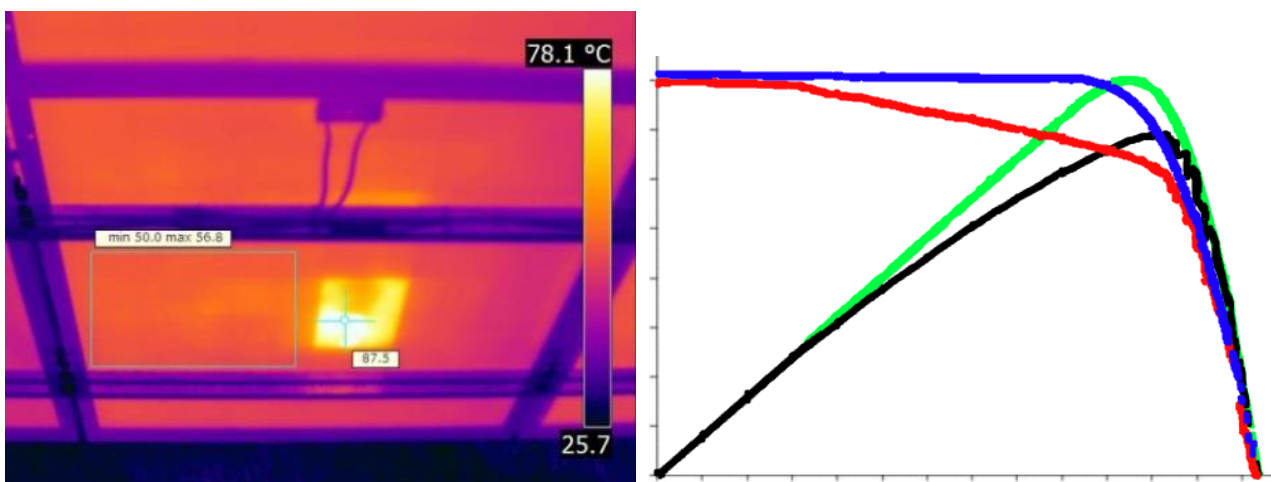


Figure 3.5.2: Ultraviolet fluorescence image of two modules, one with optical degradation causing low ultraviolet response (a), and one without optical degradation and therefore higher ultraviolet response (b) [9].

### 3.6 Hot-Spots

Moretón et al. [10] explored several cases of hot-spots in PV-modules in visual range, IR, and EL. The hot-spots occur when a faulty or damaged cell has an increased internal resistance, causing the driving current from the other cells in the same sub-string to be released as heat. The cause of the increased resistance may be of external kind as shading or dust, or it may be internal as cell-cracks, defective soldering, PID, etc. These hot-spots may decrease the lifetime of the module, and/or reduce its operational efficiency. Moretón et al. [10] also proclaim that the issue of hot-spots due to cell-cracks will endure, as a result of thinner wafers being used in the production of PV-cells. [10] Moretón et al. [10] found that infrared thermography is the best tool to find hot-spots in active PV-modules, and an IV-sweep of the module may also detect issues with the module. Examples of this is shown in the IRT-result in Figure 3.6.1a, and the IV-sweep shown in Figure 3.6.1b. In this IRT-image, it is easy to detect a troublesome component in the module from the sudden, and significant gradient in the module temperature around the area in question. The IV-sweep also show a considerable drop in fill-factor, compared to the reference values. Figure 3.6.2a shows an example of an IRT-result of a problematic junction-box, where there is a high temperature concentration in a component within the junction-box. These hot-spots may cause further damage to the module by overheating of the internal components. Figure 3.6.2b shows an example of an electroluminescence image of a module suffering from hot-spots. In this case, it is the dark areas in the cells on the left, and the top-centre cell with isolated areas suffering from excessive heat production. [10]

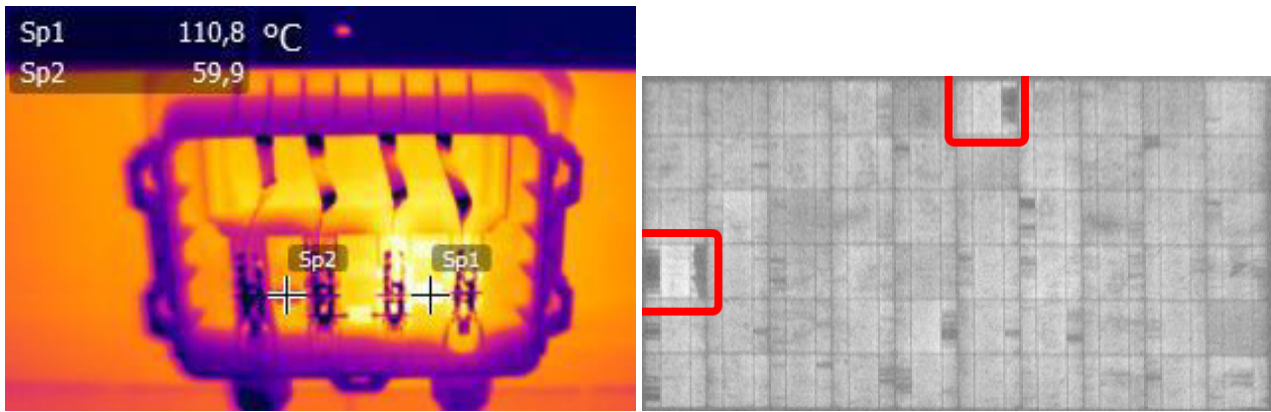


(a) Hot-spot diagnosed by infrared thermography of module backside [10].

(b) Current-voltage, and power-voltage curves of module with hot-spot, with reference plots marked in red/black and blue/green, respectively [10].

Figure 3.6.1: Infrared thermography, and current-voltage/power-voltage response of a photovoltaic module suffering from reduced fill-factor caused by hot-spot [10].





(a) Infrared thermography of a high-temperature issue in a module's junction-box [10].

(b) Electroluminescence image of a module suffering from hot-spots [10].

Figure 3.6.2: Infrared thermography of a problematic junction-box, and an electroluminescence image of a module suffering from hot-spots [10].

### 3.7 Fault Statistics

This part of the literature review addresses fault statistics of PV-modules. There are some of the claims from different sources which contradict each other, especially in terms of which kinds of faults are the most prevalent. These differences may be caused by different analysis methods, or being based on different data bases.

Haque et al. [33] found the most common faults in PV-modules are *light induced degradation*<sup>7</sup> or snail trails. They stated that about 2% of the modules do not reach the lifetime suggested by the manufacturer warranty, as is supported by IEA-PVPS T13-01:2014 [12]. It was found that the aforementioned faults resulted in power drops of about 10%. Some of the manufacturing faults consist of clusters of micro-cracks or moderate crystalline defects, both due to errors in manufacturing. They also found several faults which would either be due to external causes, or manufacturing errors. Some of these are improper handling during transportation, improper clamping, circuit faults, and lightning damages. The damages from transportation were mostly delamination, or cracks in either the covering glass plates or the cells themselves, each needing either IRT- or EL-imaging to be detected. In the case of the clamping, the problem often seemed to be the clamps either being improperly shaped, or being placed in a way which caused damage to the glass plate. In the case of circuit faults, it is most often connection issues, or damage allowing for moisture ingress causing corrosion or shorts. Lightning strikes are also known to cause damage by over-current load of the module. [33]

Per the IEA-PVPS T13-01:2014 report by M. Köntges et al. [12], one of the most apparent issues in PV-modules is ethylene-vinyl acetate (EVA) discolouration. The discolouration is mainly caused by a combination of UV-radiation, oxygen- and/or water exposure, which results in yellowing of the EVA film laminated around the PV-cells. Over around 1800 studies, they found that EVA-discoloration causes an increase in power loss of about 0,5% per annum. It was also found that of the 1800 studies, 60% of the modules had EVA-discoloration of some degree, while the most severe cases led to

<sup>7</sup>Light induced degradation (LID) of a PV-cell, caused by boron-oxygen faults from the wafer enduring prolonged light exposure. LID causes a reduced minority-carrier lifetime in the wafer. [34]

a power loss of around 10%. The most prevalent reason for the discolouration seems to be inadequate additives or their concentration in the EVA. The discolouration can lead to high temperatures, embrittlement of the EVA, and corrosion. [12]

The Si-cells are brittle, and cracks in them may often not be visible to the naked eye. In the case of the IEA report, it was found that the most common PV-module configurations were 60 cells with three bypass-diodes. This configuration was therefore used in the research in PV-module performance in relation to cell-cracks. The most common sources of cracks seemed to be mishaps during the wafer cutting process, the stringing of cells, embedding them in the module, packaging them, transporting them, and installation of the modules. The cracks may develop to be longer and wider over time, caused by mechanical stress and/or thermo-mechanical stress. The severity of the power loss in a cell is dependent on the inactive area caused by the cracks. Herein, the length and width of the cracks play a major role, but the most important factor is the direction of the crack. The most severe cases can cause large enough power losses in the cell, causing the bypass-diode to enable. Such a case may cause a module power loss of 33%, depending on the internal circuit characteristics of the module. An example done on a solar power plant with 159 modules at 165 Wp which had been in operation for 6 years, showed that cracks had caused a power loss of 10% in 50% of the modules, and 3,8% of the modules showed an active bypass-diode. [12]

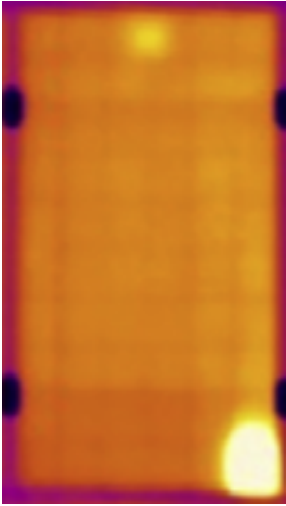

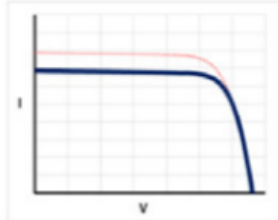
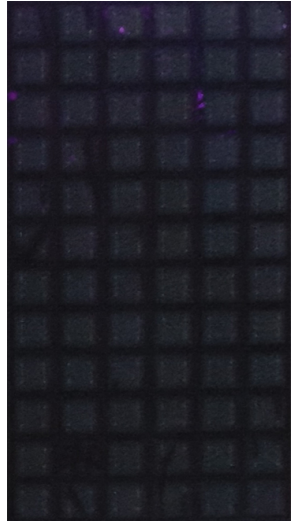

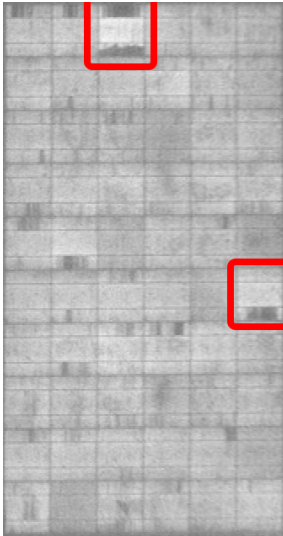
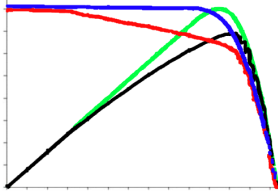
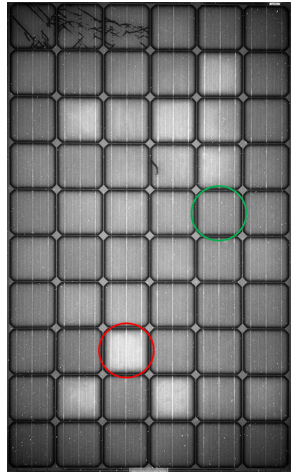
Investigation of burn marks revealed that they are mostly caused by heat as a result of either solder bond failure, ribbon breakage, reversed current flow, etc. The solder- or ribbon bond failures were predominantly caused by thermal fatigue, as a result of thermal resistance runaway where heat causes the resistance to increase, causing the cell to heat even further. The reversed current cases were caused by shading, cracked cells, shunted cells, or other thermal runaway. They found that in the worst cases, the damaged cells can cause situations of electric arcs, which in turn can result in the module catching fire. Infrared thermal imaging can identify if the module should be replaced in cases of continued heating of the burn-marked areas. [12]

They also investigated cases of modules suffering from potential induced degradation (PID), which are caused by a high positive potential in the cell relative to ground. It was found that these cases resulted in low power loss in situations of high incident irradiance, while showing more power loss in cases of low incident irradiance. The modules showed no signs of fault in the visible part of the electromagnetic spectrum, while detectable with IRT- and EL- imaging. Therefore, they assumed that there may be many cases of unreported modules suffering from PID. They also found that modules with PID can reach a power loss of up to 100% over several months. Meanwhile, this can be rectified over a few hours by applying a reverse voltage on the module and a low resistance contact to the glass and frame. [12]

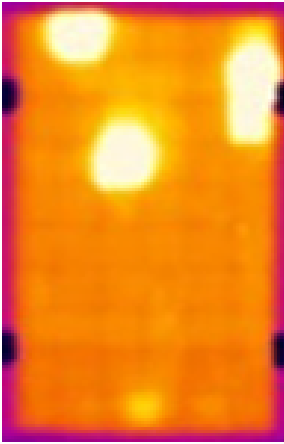
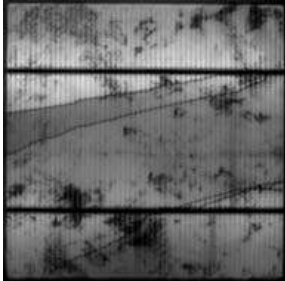
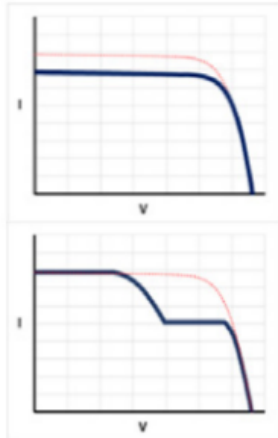
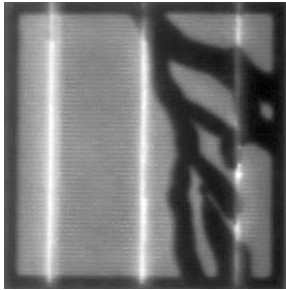
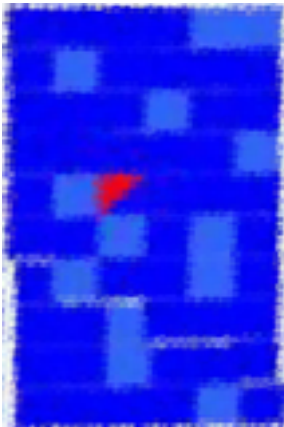
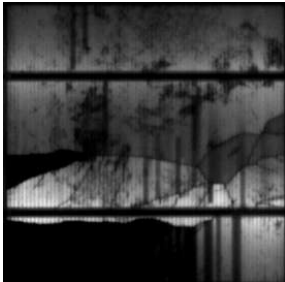
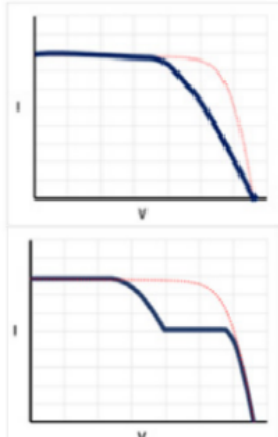
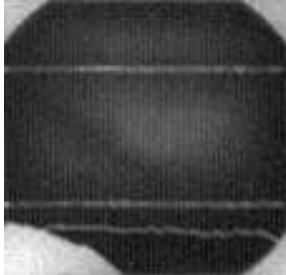
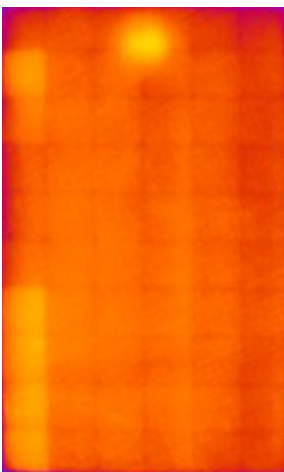
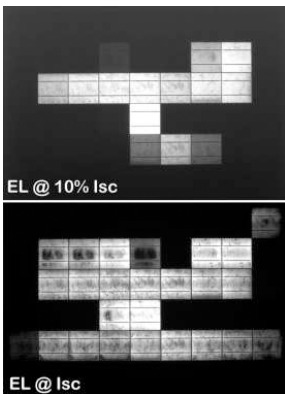
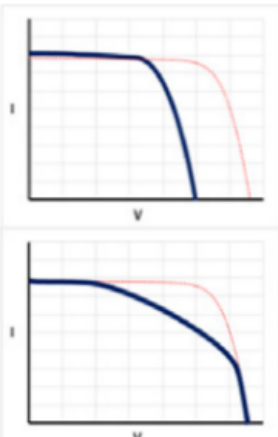
### 3.8 Fault Detection Summary

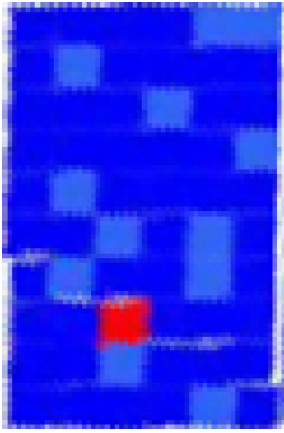

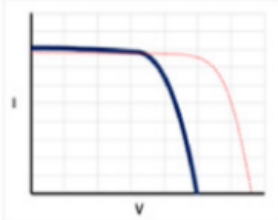
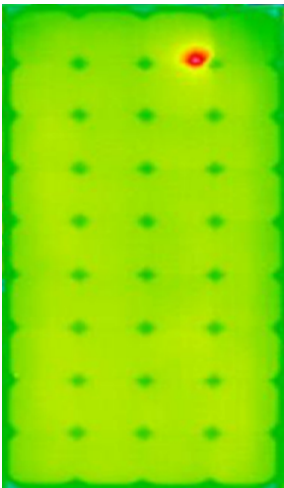
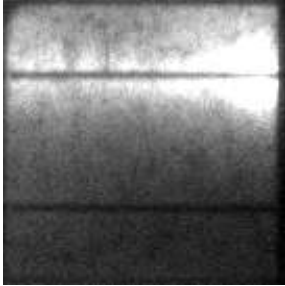
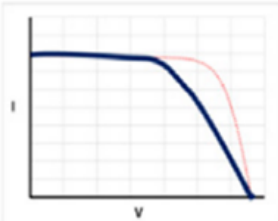
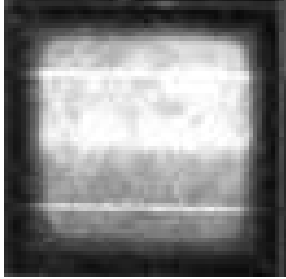

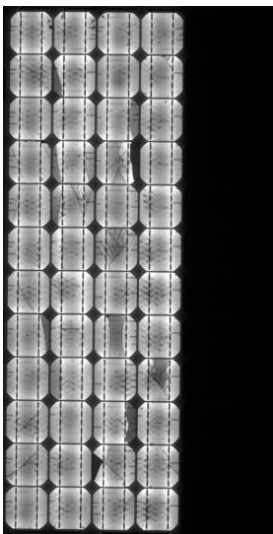
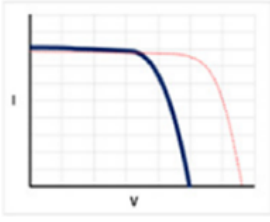
Table 3.8.1 shows a summary of the different main PV-module faults and their respective symptoms in view of IRT-, EL-, and UVF-imaging, as well as IV-sweeps. These examples were found during the review of the current topic literature.

Table 3.8.1: Main fault symptoms with infrared imaging, electroluminescence imaging, current-voltage testing, and ultraviolet fluorescence imaging. Each method is shown by examples that in general do not correspond to the same module.

IRT	EL	IV	UVF
<b>Optical degradation</b>			
 <p data-bbox="300 1227 336 1261">[7]</p>	 <p data-bbox="619 1227 655 1261">[9]</p>	 <p data-bbox="938 1227 975 1261">[7]</p>	 <p data-bbox="1249 1227 1286 1261">[9]</p>
<b>Hot-spots</b>			
 <p data-bbox="300 1883 336 1917">[10]</p>	 <p data-bbox="619 1883 655 1917">[10]</p>	 <p data-bbox="938 1883 975 1917">[10]</p>	 <p data-bbox="1249 1883 1286 1917">[5]</p>



IRT	EL	IV	UVF
<b>Cell Cracks</b>			
 <p data-bbox="300 779 339 813">[7]</p>	 <p data-bbox="611 779 667 813">[12]</p>	 <p data-bbox="932 779 987 813">[7]</p>	 <p data-bbox="1246 779 1302 813">[12]</p>
<b>Isolated cell area</b>			
 <p data-bbox="300 1357 339 1391">[7]</p>	 <p data-bbox="611 1357 667 1391">[12]</p>	 <p data-bbox="932 1357 987 1391">[7]</p>	 <p data-bbox="1246 1357 1302 1391">[12]</p>
<b>Potential induced degradation (PID)</b>			
 <p data-bbox="300 1951 339 1984">[7]</p>	 <p data-bbox="494 1671 611 1693">EL @ 10% Isc</p> <p data-bbox="494 1868 574 1890">EL @ Isc</p> <p data-bbox="611 1951 667 1984">[12]</p>	 <p data-bbox="932 1951 987 1984">[7]</p>	

IRT	EL	IV	UVF
<b>Short/Shunt</b>			
 <p data-bbox="300 763 339 797">[7]</p>	 <p data-bbox="611 763 667 797">[12]</p>	 <p data-bbox="935 763 975 797">[7]</p>	
<b>Broken interconnect</b>			
 <p data-bbox="300 1375 339 1408">[7]</p>	 <p data-bbox="611 1375 667 1408">[12]</p>	 <p data-bbox="935 1375 975 1408">[7]</p>	 <p data-bbox="1246 1375 1302 1408">[12]</p>
<b>Defective bypass-diode</b>			
 <p data-bbox="300 2024 339 2058">[7]</p>	 <p data-bbox="611 2024 667 2058">[12]</p>	 <p data-bbox="935 2024 975 2058">[7]</p>	

## 4 Method

The main goal of this project was to perform fault-detection analysis of PV-modules by utilising the techniques of IV-tracing and EL-, IRT-, and UVF-imaging. Thereupon, the results were visually analysed and discussed, to compare the efficacy of each fault-detection technique compared to the others. To get the most viable results, IEC-standards were followed where possible.

Chapter 4 encompasses the methods used for Preliminary Research, Common Methods for All Tests, Ultraviolet Fluorescence Experiments, Current-Voltage Tracing Experiments, Infrared Thermography Experiments, and Electroluminescence Experiments. The Current-Voltage Tracing Experiments is done in two different ways, one with automated tracing utilising HT IV-500W apparatus, and the other done manually with variable resistors and digital multimeters.

### 4.1 Preliminary Research

The preliminary research was done to get an overview of the current research in the field, regarding the different relevant methods for fault detection in photovoltaic modules. The main tools for obtaining information on the current research were Google Scholar, University of Agder library (Oria), Institute of Electrical and Electronics Engineers (IEEE), Research Gate, Science Direct, International Electrotechnical Commission (IEC), International Energy Agency (IEA), as well as papers recommended by the supervisors. Operational manuals were also studied before the use of all the equipment utilised in the experiments, as well as consulting with experienced personnel/users of the equipment. In addition to the IEC-standards, previous methods of fault detection were also studied. After performing the experiments, the findings were compared to the findings of the relevant previous research in Chapter 3.

### 4.2 Health and Safety Considerations

Precautions were taken when performing the following experiments, to ensure the safety of the person performing them. A risk analysis was performed to identify the possible dangers of working with the experiments. As some of the experiments were done on a roof-top approximately 16 meters above the ground, one had to be careful when moving around on the roof to not trip on any of the wires or beams for the PV-module stands, in addition to there being guard-rails all around the roof. The weather was also taken into account when assessing if the conditions allowed for safe work on the roof. As all of the modules tested in these experiments were operating without sting-connections to other modules, the voltage of the modules was low enough as to not cause any arcing of concern to the health of the person disconnecting them before performing IV-tracing experiments.

For the indoor lab-experiments, the main concerns were electric shock, or UV-exposure. The possible source of electric shock was the power-supply used to deliver forward-bias current to the PV-modules. Proper procedure was followed to eliminate the possibility of electric shock, by assuring that all work with connecting or disconnecting the cables to the modules was only done while the power-supply was turned off completely. UV-protection gear was always used while performing experiments including the use the UV-torch, and the UV-torch was never pointed toward the skin or eyes. As most of the experiments performed in the lab were done with no light in the room, the

floor was cleared of any items capable of causing the person performing the experiment to trip over them.

### 4.3 Common Methods for All Tests

There were some steps used for all of the experiments on all of the PV-modules. Firstly, a visual inspection of the module was performed. Wherein, dust or dirt was removed, and an inspection of eventual visible signs of possible faults was performed. The meteorological conditions were recorded and at least 15 minutes of settling time was allowed between each experiment to ensure steady-state operation. The type of experiment performed was noted, along with the module designation and the timestamp correlating to the experiment. In the case of a new module being introduced to the pool of modules, the specifications of the modules were noted in Table 4.3.1 along with a module designation based on which roof the module was located on.

Prior to the experiments, a visual inspection of the modules was performed based on the checklist published by IEC [35]. The blank checklist is given in Appendix A.

Table 4.3.1: Modules tested, their designation, and characteristics.

Characteristic	Module Specifications			Unit
Module designation	$\alpha$ -I	$\alpha$ -II	$\alpha$ -III	—
Manufacturer	RS Pro	Elkem	Elkem	—
Model	9046125	E5286 – A10162	E5286 – A10156	—
Power	20	214,96	216,94	Wp
Power tolerance	—	$\pm 3\%$	$\pm 3\%$	—
Nominal Voltage	17,5	29,16	30,15	V
Nominal Current	1,15	7,37	7,20	A
Open-Circuit Voltage	22	36,04	36,85	V
Short-Circuit Current	1,27	8,06	7,91	A
Max. System Voltage	1000	1000	1000	V
Geometry	3x12 (half)	6x10	6x10	Cells
Module designation	$\alpha$ -IV	$\beta$ -I		—
Manufacturer	Westech	Suntech		—
Model	CL-160WM	STP225 – 20/Wd		—
Power	160	225		Wp
Power tolerance	$\pm 3\%$	0/+5 %		—
Nominal Voltage	18,1	29,6		V
Nominal Current	7,20	7,61		A
Open-Circuit Voltage	22,2	36,7		V
Short-Circuit Current	9,6	8,15		A
Max. System Voltage	1000	1000		V
Geometry	4x9	6x10		Cells

Figure 4.3.1 shows the images of all of the modules tested in the following experiments, modules  $\alpha$ -I and  $\alpha$ -II had the same type of junction box and circuitry within. An exception is module  $\beta$ -I, where the attempt to open the junction box failed. All of the results from the methods being mentioned in the following chapters were at last, presented and discussed in Chapter 5 and 6, respectively.

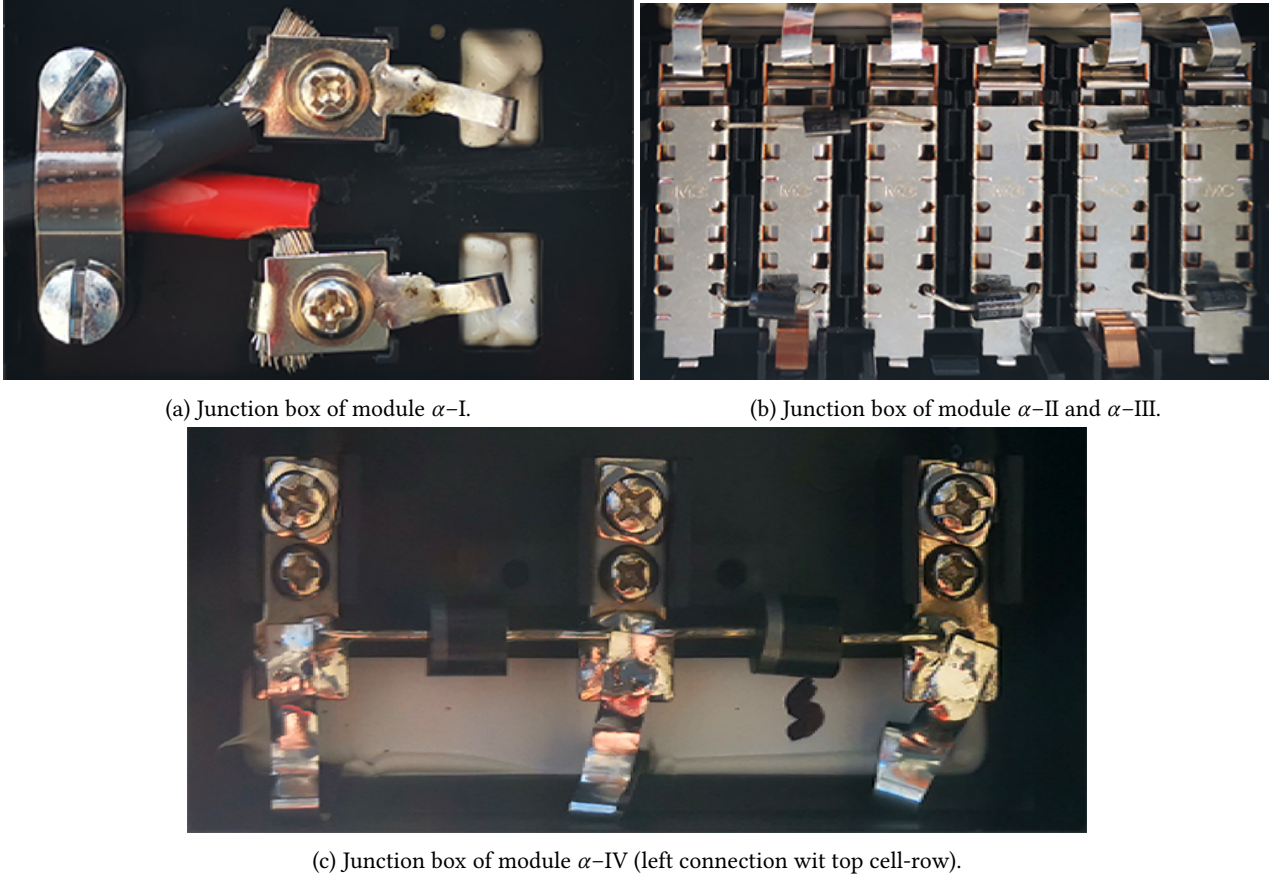


Figure 4.3.1: Junction boxes of the four of the modules tested in these experiments.

#### 4.4 Ultraviolet Fluorescence Experiments

Initially, the modules available for being experimented on were visually inspected at night using the ultraviolet (UV) torch from Trotec, UV-Torch Light 15F [36]. The modules with an extended time of sunlight exposure had a significant ultraviolet fluorescence (UVF) response. From the inspections, several modules of interest were selected for further testing, as noted in Table 4.3.1.

The UVF-imaging of the modules were done in a dark laboratory. The camera, a Canon EOS 400D, was mounted on a tripod in front of the module to keep the camera stable for the long exposure time needed for the imaging. After studying the Canon manual [37], the camera was set to manual mode, the flash was disabled, the aperture was set to automatic, and the ISO was set to the maximum of 1600. To eliminate most of the white light from the UV-torch, the Trotec 15F filter [38] was mounted on the torch. The camera was first focused with the lights on, using the auto-focus. The auto-focus was subsequently disabled, to mitigate the camera getting out of focus when performing UV-imaging in the dark laboratory. The image brightness was controlled by adjusting the shutter speed of the camera, making sure the images were neither too dark nor saturating the sensor.



Because of this experiment being done with only one UV-torch, some of the imaging of the modules had to be segmented across 2-3 images per module. After the images were taken, the raw .CR2 image-files were transferred to a computer with Adobe Photoshop CS6. The first step of post-processing each image was the lens correction, done with profiles included in Photoshop for the specific camera and lens used in the experiment. The lens correction profiles corrected both the image-warp and vignetting caused by the camera-lens. Subsequently, *histogram equalisation*<sup>8</sup> was performed on each image, to make them more suited for visual inspection and comparison with other experiment results. Where relevant, the segmented UVF-images were lastly compiled into one image.

## 4.5 Current-Voltage Tracing Experiments

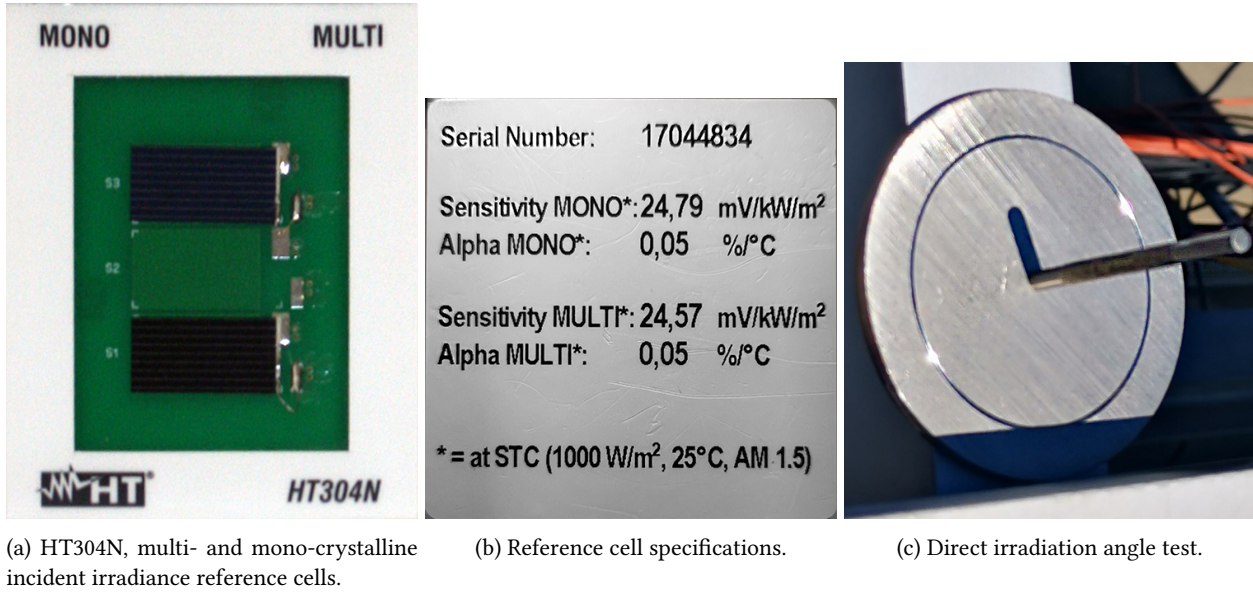
### 4.5.1 Automatic Current-Voltage Tracing

The IV-tracing was performed using the HT I-V 500W from HT Italia. As according to IEC 60891:09, the IV-tracing experiments were done with less than 2 okta of cumulus cloud coverage and incident irradiance of more than  $700 \frac{\text{W}}{\text{m}^2}$ . The tool depicted in Figure 4.5.1c was used to ensure satisfactory relative direct irradiance angle. The reference cell, shown in Figure 4.5.1a, was connected to the relevant port of either multi- or mono-crystalline, depending on the cell technology of the module in question. Before performing the IV-tracing, the temperature-probe was attached to the back of the module, directly behind a cell. After the measured temperature had reached steady-state, the IV-tracing was performed, and the results were saved for later transfer to a computer for post-processing.

Post-processing of the IV-trace results were done by changing the colours of the plots, to a standard set of colours based on the type of plot, and increasing their thickness to make them more suitable for visual analysis. Both the nominal- and STC-corrected plots were included in each graph, to make the analyses of the module-performance easier to perform. Lastly, more defined axes, and a proper legend was added to each figure for reference.

---

<sup>8</sup>"Histogram equalisation is a nonlinear process aimed to highlight image brightness in a way particularly suited to human visual analysis. Histogram equalisation aims to change a picture in such a way as to produce a picture with a flatter histogram, where all levels are equiprobable." - Nixon et al. [39]



(a) HT304N, multi- and mono-crystalline incident irradiance reference cells.

(b) Reference cell specifications.

(c) Direct irradiation angle test.

Figure 4.5.1: Irradiance testing equipment used in conjunction with HT I-V 500W.

#### 4.5.2 Manual Current-Voltage Tracing

In the case of modules having a nominal power output lower than that of the capabilities of the IV-500W, a manual IV-trace was performed. This process entailed the process of incrementally increasing the series resistance across the two poles of the module, meanwhile measuring the applied resistance and the voltage across it. The current and power was then calculated according to Ohm's law,

$$U = R \cdot I, \quad \text{and} \quad P = U \cdot I, \quad (7)$$

Where  $U$ , and  $R$  is the measured voltage, and -resistance, respectively,  $I$  is the current, and  $P$  is the Power. Assuming the first part of the IV-curve being linear, as the voltage increases from zero, the short-circuit current was calculated and used to replace the low currents through the module as the voltage across the module was increased to the activation voltage of the PN-junctions in the cells. Following this, the temperature coefficients of the module, found in the module's data-sheet, were used to calculate an STC-corrected IV-curve according to IEC 60891:09. The equations read as

$$I_1 = I_0 \cdot (1 + \alpha \cdot (T_1 - T_0)) \cdot \frac{G_1}{G_0}, \quad (8)$$

and

$$V_1 = V_0 - R_S \cdot (I_1 - I_0) - \kappa \cdot I_1 \cdot (T_1 - T_0) + \beta \cdot (T_1 - T_0), \quad (9)$$

where  $\alpha$  is the relative current temperature coefficient,  $\beta$  is the relative voltage temperature coefficient,  $R_S$  is the series resistance,  $\kappa$  is a curve correction factor,  $I_0$ ,  $T_0$ , and  $G_0$  are the initial current, module temperature, and incident irradiance values, respectively, and  $I_1$ ,  $T_1$ , and  $G_1$  are the STC corrected target values of current, module temperature and incident irradiance, respectively [40].

The nominal IV- and PV-curves were created by running the Simulink file for the partial shading analysis of photovoltaic modules, published by Mathworks [41]. Within the Simulink model, the data-sheet values of the module were used, as well as the STC-values of incident irradiance and cell temperature at  $1000 \frac{\text{W}}{\text{m}^2}$  and  $25^\circ\text{C}$ , respectively. The resulting current and voltage curves were then exported to Microsoft Office Excel, where the power values corresponding to each voltage were calculated, and the IV- and PV-curves were plotted along with the manually measured IV- and PV-curves. Figure 4.5.2 shows photographs of the variable resistors, and the Fluke 179 digital multimeter used for manual IV-tracing.

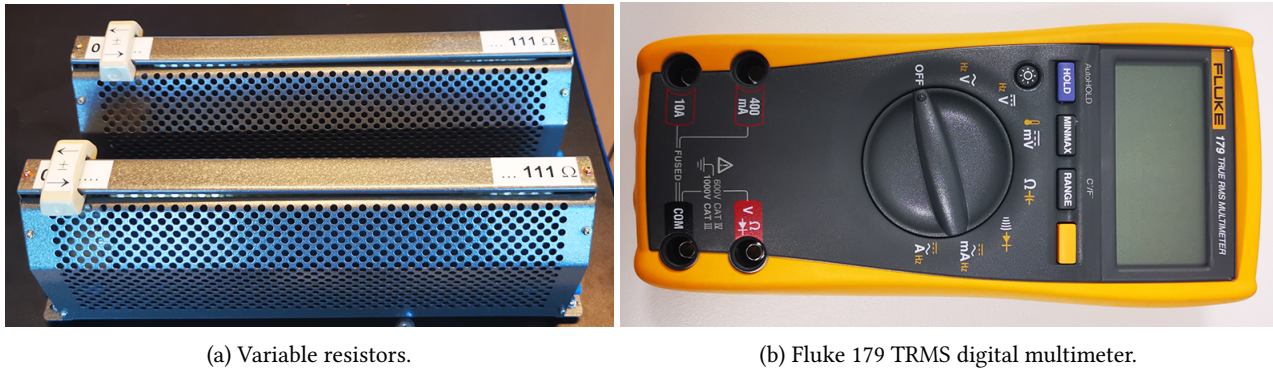


Figure 4.5.2: Equipment used for manual current-voltage tracing of photovoltaic modules.

## 4.6 Infrared Thermography Experiments

Before each infrared thermography (IRT) experiment was performed, the meteorological conditions were checked to be within the limits given by the IEC TS 62446-3:2017 standard. The main points of which were incident irradiance of more than  $600 \frac{\text{W}}{\text{m}^2}$ , wind speeds below  $7,777 \frac{\text{m}}{\text{s}}$ , a cumulus cloud coverage below 2 okta, and a camera angle within the range of  $5\text{-}60^\circ$  relative to the normal of the module plane [4]. In one case, the module had to be moved to eliminate infrared reflections in the module from the guard-rail beside it.

Two different IRT-cameras were used during these experiments, mainly because of issues of resolution and the available space in front of the modules. Firstly, the Fluke Ti400 was used for the IRT-images, according to the manual by Fluke [42]. The camera was mounted to a tripod to eliminate motion blur in the results. The images were then transferred to a computer for post-processing. The .IS2 files contain both the IRT-, RGB-image, and metadata of the experiment results, making it a simple process to adjust the images so that they were easy to visually inspect [43]. Opening the files in Fluke SmartView gave the possibility of adjusting the temperature scale, emissivity settings, RGB-/IRT-image ratio, temperature measurement areas, and more. The emissivity was set as discussed in Chapter 2.5, at 0,85 based on the relative camera angle. The colour/temperature range of the images was then set to a temperature range, which would aid in the visual inspection of the images. Lastly, the image was exported with colour-bar, and the images were cropped to eliminate the background of the image. The limiting factor of this process was the low resolution of the Fluke Ti400, therefore the FLIR A6750 MWIR was applied in the experiments.



The complexity, weight, and cost of the FLIR A6750 MWIR made the experiment process more tedious, compared to the Fluke Ti400. Firstly, the lens needed to be attached to the camera. This process entailed removing the dust cover of the sensor, and attaching the lens all the while keeping the camera at an angle to limit the amount of dust falling onto the sensor. The camera was then mounted to a tripod, and the external power supply was attached to the camera. After powering on the camera, it would start the processing of booting up and cooling the sensor, this took a few minutes. A laptop, placed on a table with wheels, was also booted up during this time and was connected with a TP-cable to the camera when the "ready"-light of the camera was active. The table with wheels made the process of moving the equipment much simpler. After booting the camera control software, a digital connection between the computer and the camera was made, resulting in a live image on the computer-screen. This live-image was used to position the camera, focus the lens, and adjust the temperature range. After capturing all the images, the images were exported and transferred with a colour-bar before the images were cropped. Not having access to software able to read the file format of the raw data from the FLIR camera, containing the temperature metadata, digital colour-matching of the exported .png image and its colour-bar was used to obtain the maximum and minimum temperatures of the module. This gave approximate temperatures of these points, while not being as precise as the method used with the Fluke camera. Because of this, the Fluke images were used where the resolution of the area of interest was not too low to perform a visual inspection of the results. Calibration of these cameras was not performed as the main goal of these experiments were to detect the difference in temperatures within the modules, not as much the absolute temperatures.

IRT-images were also taken during the process of electroluminescence imaging, to explore the possibility of diagnosing faults with current applied to the module, without any sunlight. Figure 4.6.1 shows the experimental setup for the IRT-imaging with the FLIR A6750 MWIR thermal camera, and some of the modules tested in this Thesis.



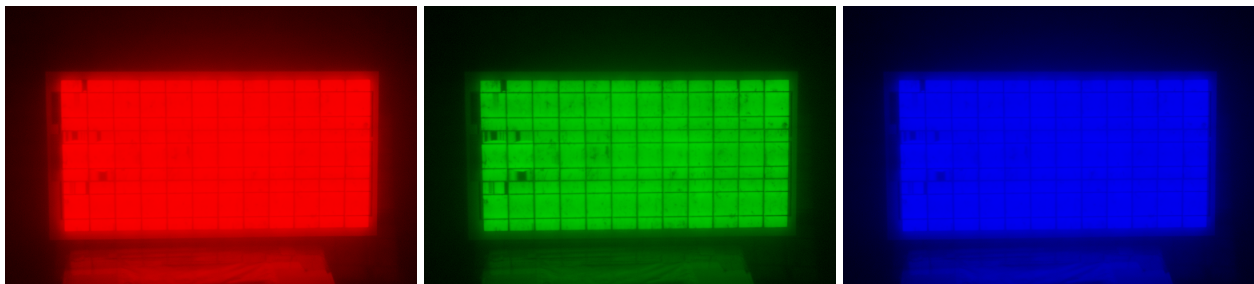
Figure 4.6.1: Photography of the author with FLIR A6750 MWIR camera on tripod, set up for infrared thermography imaging of photovoltaic modules.

*Photo: Anne Gerd Imenes.*

## 4.7 Electroluminescence Experiments

The electroluminescence (EL) imaging was done with a Nikon D5600 DSLR camera according to its manual [44] and IEC 60904-13:2018 standard [11]. The camera was mounted to a stable monopod with a heavy base, and was connected to a laptop with software from BrightSpot PVEEL [45]. The modules being tested were connected to a DC-power supply, set to deliver a current equal to the short-circuit current, and applied electric potential at 110% of open-circuit voltage. The camera was then set up, with filters which blocked visible light from reaching the sensor. The computer software was then used to focus the camera and perform the EL-imaging. During this process, the ISO of the camera was adjusted to ensure a bright image, while avoiding the sensor being saturated. Lastly, the images were transferred to another computer, in raw .nef-format, to be post-processed.

The raw .nef-files were firstly converted to .dng-format, using the Adobe DNG Converter. This conversion was done because the instance of Adobe Photoshop CS6 available, was not able to process the .nef-formatted files. As the conversion to .dng retained the raw-data of the .nef-file, Photoshop could easily pick up on which camera and lens that were used to capture the image, making the process of removing lens warp, and -vignetting a quick task. There were situations where the light captured in the blue and red band created a "glow" effect, where the light from some areas was bleeding over to other areas. This effect was not present in the green band, therefore only the green band was used for the visual analyses. The three different bands are shown in Figure 4.7.2. Lastly, a histogram equalisation, and greyscale-conversion was performed on each image to make them easier to analyse visually. The resulting images were made to show the low excitation being dark, and the high- being light. Figure 4.7.1 shows some of the equipment and the setup related to the EL-, or UVF-experiments.



(a) Electroluminescence result image, red band only. (b) Electroluminescence result image, green band only. (c) Electroluminescence result image, blue band only.

Figure 4.7.1: All three colour bands of red, green, and blue, from electroluminescence experiment result image of a photovoltaic module.



(a) Camera setup for ultraviolet fluorescence imaging- (left), and electroluminescence imaging (right) experiments.



(b) Gophert CPS-6011 (0–60 V, 0–11 A) power supply used to supply short-circuit current to the photovoltaic modules, at 110% of open-circuit voltage.

Figure 4.7.2: Equipment setup for both the electroluminescence- and ultraviolet fluorescence imaging experiments.

After performing the experiments in this chapter, the results were presented in Chapter 5, and discussed in Chapter 6. Thereupon, the gathered data and knowledge was used to form a conclusion in Chapter 7. Lastly, the suggested further work based on the thesis was presented in Chapter 8.



## 5 Results

This part of the report addresses all of the results found from each module, and fault-detection techniques. The chapter is structured such as to undertake each module in turn, with all of the results relating to the module in question being addressed before the next module is addressed. Some areas of the figures presented in this chapter have highlighted areas, which are used in the discussion, in Chapter 6.

When presenting the results from the current-voltage tracing experiments of the modules in this chapter, the curves referred to as "STC-corrected" are of the measured data which is mathematically corrected to STC with regards to measured module temperature and measured irradiance, the curves referred to as "nominal" are generated based on the data-sheet values given by the module manufacturer.



### 5.1 Module $\alpha$ -I

This chapter addresses the results from the testing of the mini-module with designation  $\alpha$ -I, from RS Pro (ref: Table 4.3.1). Figure 5.1.1 shows the RGB photography of the module, with a circuit diagram overlay, inferred from the visible circuits on the module (and the junction box). No bypass-diodes are present in this module.

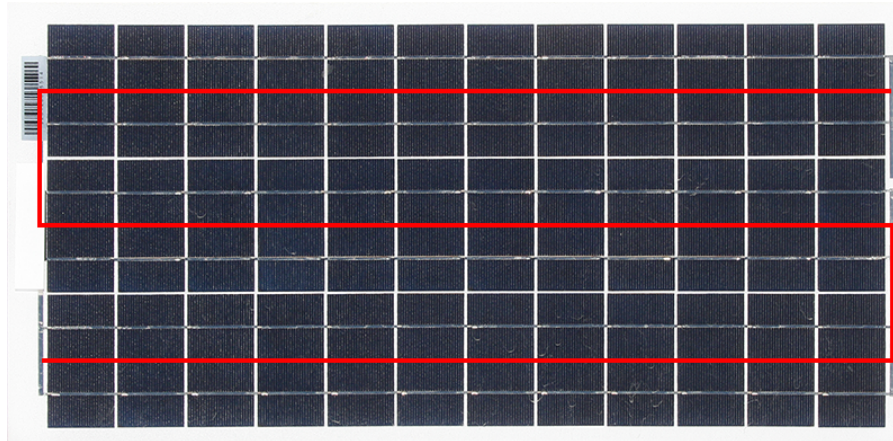


Figure 5.1.1: Photography of module with designation  $\alpha$ -I, with circuit diagram overlay.

The manually traced IV- and PV-curves of module  $\alpha$ -I is presented in Figure 5.1.2. The figure shows both the measured values, and the values corrected to STC, according to the method discussed in Chapter 4.5.2. Wherein, STC-correction of the measured curves of  $I(V)$  and  $P(V)$  are marked by the red and orange plots, respectively, while the purple and blue show the measured curves of  $I(V)$  and  $P(V)$ , respectively. The measured PV temperature ( $T_0$ ), and measured irradiance ( $G_0$ ) used for for the STC-correction and a proposed nominal curve are shown in Table 5.1.1, the STC-irradiance ( $G_1$ ), -temperature ( $T_1$ ), and current temperature coefficient ( $\alpha$ ) are  $1000 \frac{W}{m^2}$ ,  $25^\circ C$ , and  $0,003 \frac{A}{K}$ , respectively.

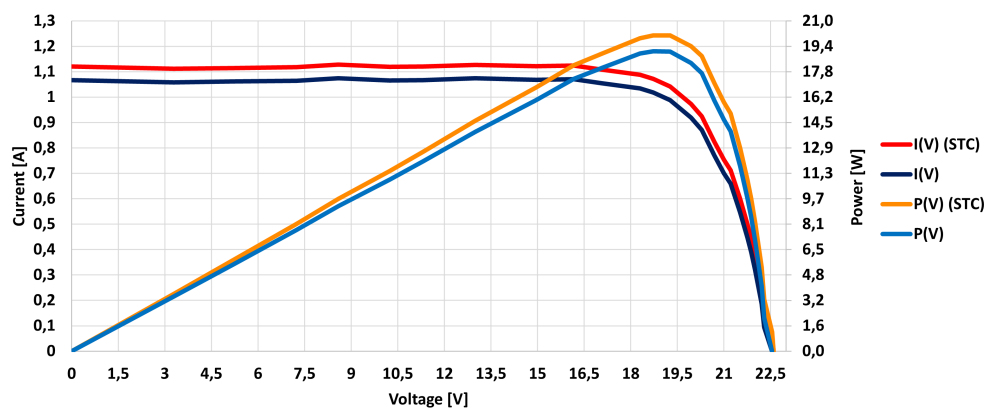


Figure 5.1.2: Measured and STC-corrected current- and power- curves as a function of voltage, module  $\alpha$ -I.

Figure 5.1.3 shows the STC-corrected IV- and PV-curves, as well as the nominal curves based on the values found on the module's data-sheet.

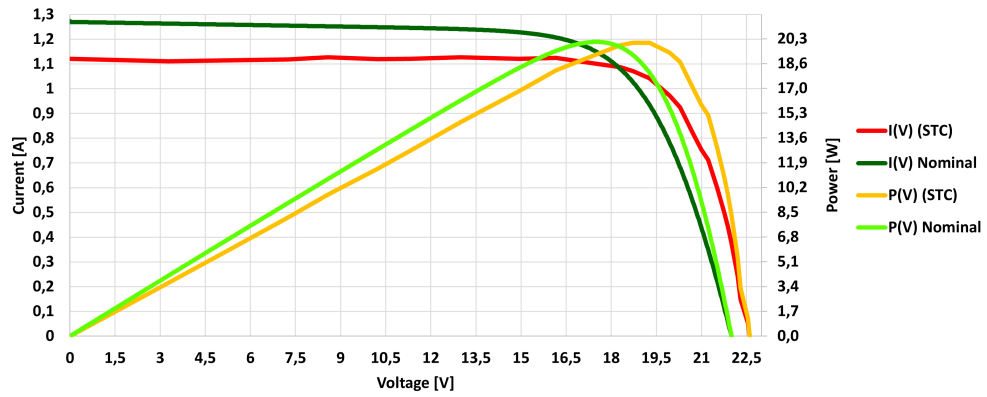


Figure 5.1.3: STC-corrected and nominal current- and power- curves as a function of voltage, module  $\alpha$ -I, according to data-sheet nominal- and open-circuit voltage.

Figure 5.1.4 shows the STC-corrected IV- and PV-curves, as well as the altered curves based on the values from the measured IV-curves. This was done with the assumption of the data-sheet values being imprecise, as an increase in  $V_{OC}$  is not expected at STC, under any known circumstances based on the literature review. The altered curve was created by adjusting the open-circuit voltage ( $V_{OC}$ ) from 22 V to 22,6 V, and the maximum power point (MPP) voltage ( $V_{MPP}$ ) from 17,5 V to 19 V, both based on the manually measured data, and otherwise keeping all current values the same.

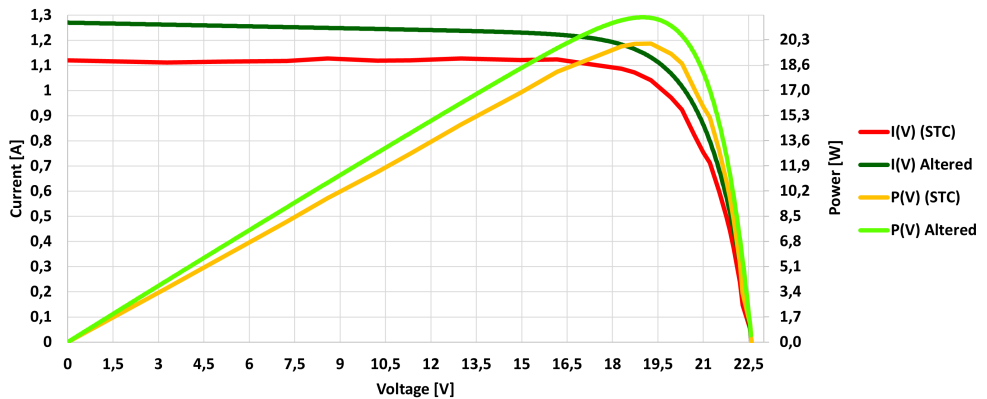


Figure 5.1.4: STC-corrected and nominal current- and power- curves as a function of voltage, module  $\alpha$ -I, according to measured maximum power point-, and open-circuit voltage.

Table 5.1.1: Test result table from current, voltage, and power experiments of module  $\alpha$ -I, including four the stages of measured, STC-corrected, nominal, and altered conditions.

Stage	Open Circuit Voltage ( $V_{oc}$ ) [V]	Short Circuit Current ( $I_{sc}$ ) [A]	MPP Power ( $P_{MPP}$ ) [W]	MPP Voltage ( $V_{MPP}$ ) [V]	MPP Current ( $I_{MPP}$ ) [A]	Fill Factor ( $FF$ ) [-]
Measured	22,6	1,07	19,07	19,27	0,98	0,6824
STC	22,6	1,12	20,07	19,27	1,04	0,7184
Nominal	22,0	1,27	20,12	17,49	1,15	0,7202
Altered	22,6	1,27	21,85	19,00	1,15	0,7820
Measured PV Temperature ( $T_0$ )				Measured Irradiance( $G_0$ )		
25,5°C				951 $\frac{W}{m^2}$		

Figure 5.1.5 shows the resulting image of the ultraviolet fluorescence (UVF) imaging of module  $\alpha$ -I. This module was chosen for further testing based on the dots of higher UVF-response along some of the bus-bars. The brightness along the edge of the image is caused by glare from the area at the circumference of the module.

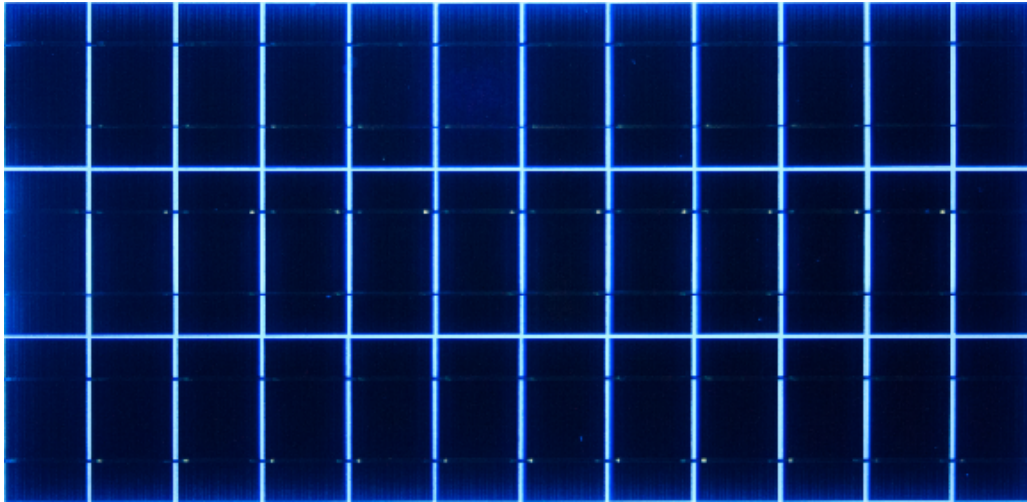


Figure 5.1.5:  $\alpha$ -I indoor ultraviolet fluorescence image.

Figure 5.1.6 shows the infrared thermography (IRT) image results, acquired with the FLIR camera. Table 5.1.2 shows the main points of interest from the IRT results, using digital colour-matching of the module to the colour/temperature-bar.

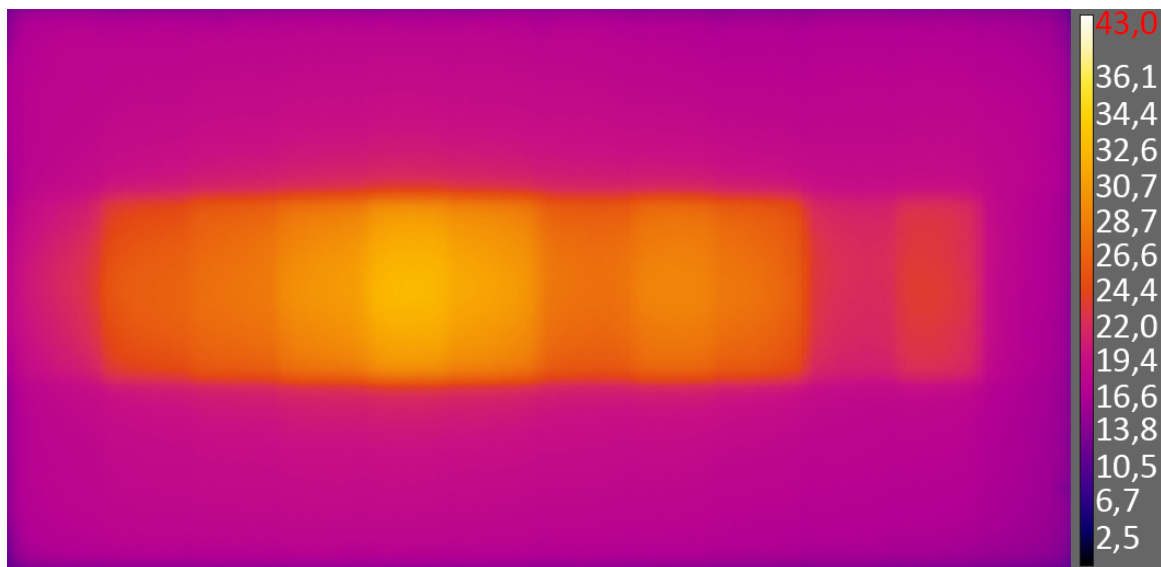


Figure 5.1.6:  $\alpha$ -I operational, outdoor infrared thermography image.

Table 5.1.2: Main temperatures of interest, outdoor infrared thermography of module  $\alpha$ -I.

Maximum Temperature	Minimum Temperature	Temperature Difference
32,6°C	16,0°C	16,6°C



Figure 5.1.7 shows the result of the electroluminescence (EL) image of module  $\alpha$ -I, after histogram equalisation and greyscale-conversion.

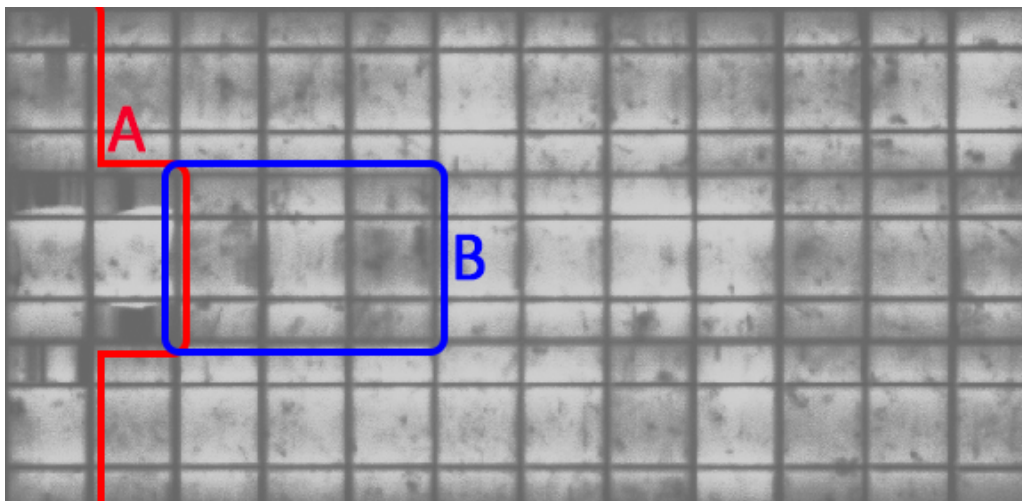


Figure 5.1.7:  $\alpha$ -I indoor electroluminescence image.

Figure 5.1.8 shows the IRT-image of the front of module  $\alpha$ -I done indoors, with forward current equal to the short-circuit current applied to the module. The results show the module having a maximum-, and minimum temperature of 36,1°C, and 27,5°C, respectively.



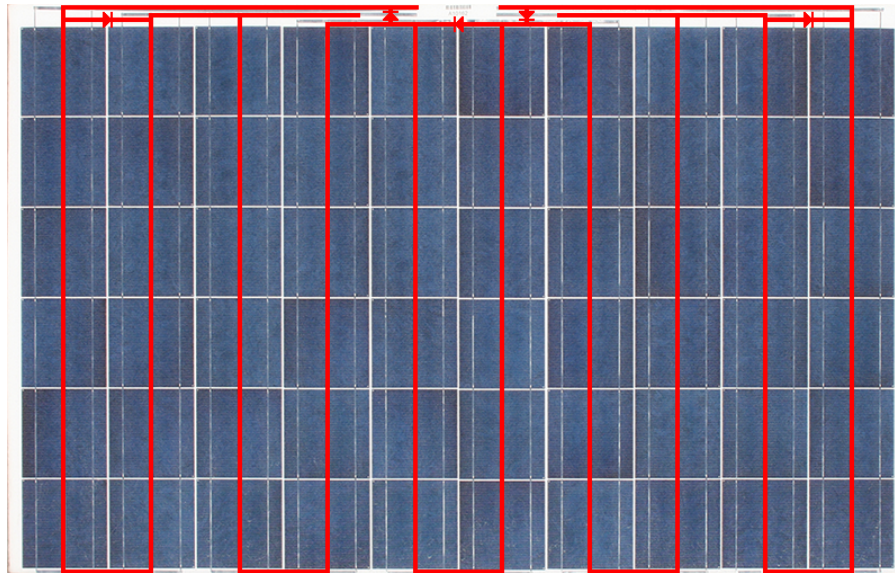
Figure 5.1.8:  $\alpha$ -I forward-current infrared image.

Table 5.1.3: Main temperatures of interest, indoor infrared thermography of module  $\alpha$ -I with short-circuit current applied in forward bias.

Maximum Temperature	Minimum Temperature	Temperature Difference	Average Temperature
36,1°C	27,5°C	8,6°C	33,5°C

### 5.2 Module $\alpha$ -II

This chapter addresses the results from the testing of the module with designation  $\alpha$ -II, from Elkem (ref: Table 4.3.1). Figure 5.2.1 shows a photography of module  $\alpha$ -II, with a circuit diagram overlay and an image of the bypass-diode configuration.



(a) Photography of module with designation  $\alpha$ -II, with circuit diagram overlay.



(b) Bypass diode configuration of module  $\alpha$ -II.

Figure 5.2.1: Photography of module with designation  $\alpha$ -II, with circuit diagram overlay, and crop of bypass-diode configuration.

Figure 5.2.2, and Table 5.2.1 shows the results of the IV-curve tracing of module  $\alpha$ -II. In the figure, the red and green coloured plots represent the IV-curves at STC-, and nominal conditions, respectively. Meanwhile, the orange and lime coloured plots represent the PV-curves at STC-, and nominal conditions, respectively.

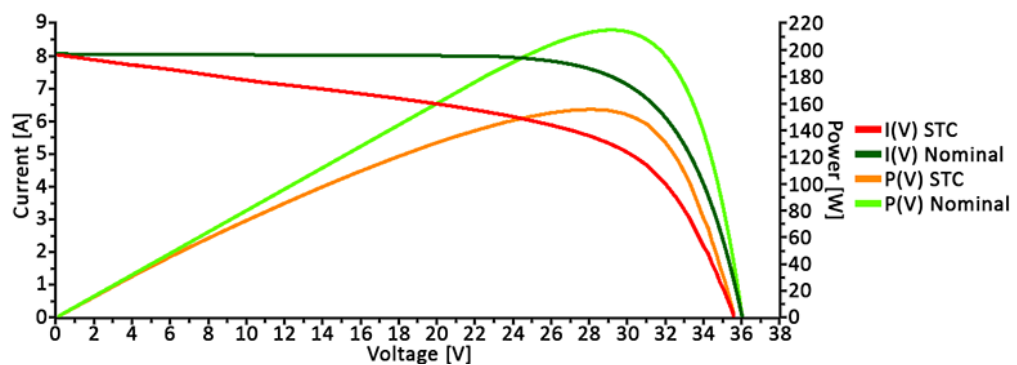


Figure 5.2.2: Current- and power- curves as a function of voltage, module  $\alpha$ -II.

Table 5.2.1: Relevant STC- and nominal values for module  $\alpha$ -II.

	STC	Nominal	Unit	Abbreviation
<b>Open-Circuit Voltage</b>	35,59	36,04	V	$V_{OC}$
<b>Short-Circuit Current</b>	7,79	8,06	A	$I_{SC}$
<b>MPP Voltage</b>	28,14	29,16	V	$V_{MPP}$
<b>MPP Current</b>	5,53	7,73	A	$I_{MPP}$
<b>MPP Power</b>	155,62	215,00	P	$P_{MPP}$
<b>Fill-Factor</b>	0,54	0,74	-	$FF$
<b>Measured PV Temperature (<math>T_0</math>)</b>		<b>Measured Irradiance (<math>G_0</math>)</b>		
15,1°C		962 $\frac{W}{m^2}$		

Figure 5.2.3 shows the UVF-image results of module  $\alpha$ -II. This image is a compound of two images, as the torch used in this experiment was unable to illuminate the whole module.

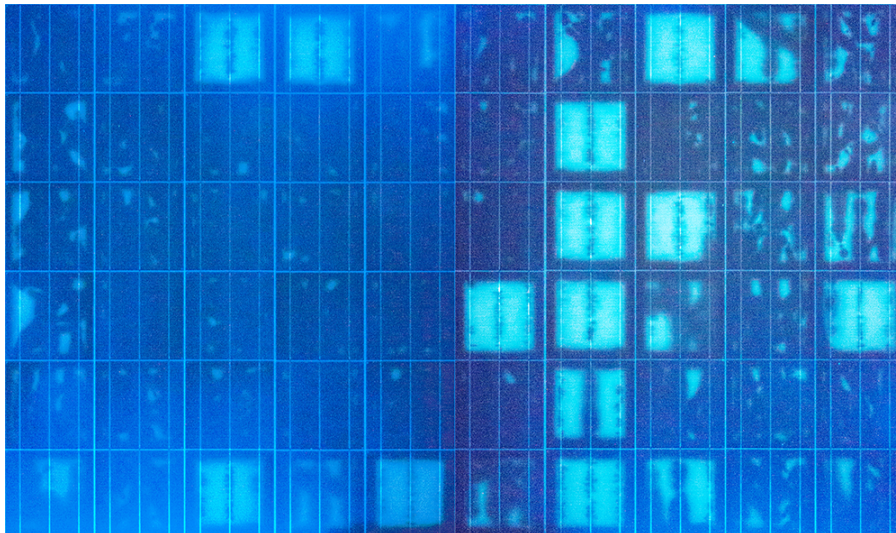
Figure 5.2.3:  $\alpha$ -II indoor ultraviolet fluorescence image.

Figure 5.2.4 shows the outdoor, operational IRT-image results of module  $\alpha$ -II, the relevant temperature measurements are shown in Table 5.2.2.

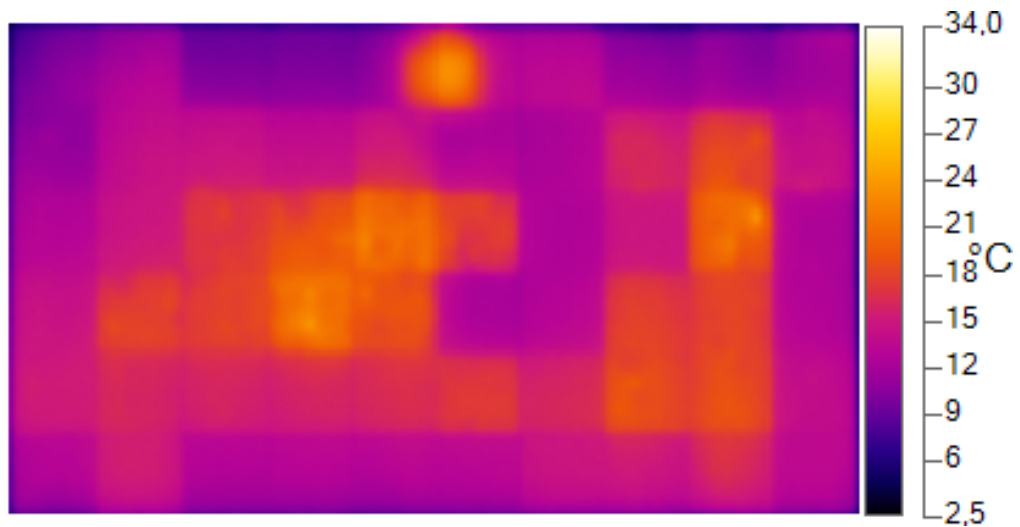


Figure 5.2.4:  $\alpha$ -II operational, outdoor infrared thermography image.

Table 5.2.2: Main temperatures of interest, outdoor infrared thermography of module  $\alpha$ -II.

Maximum Temperature	Minimum Temperature	Temperature Difference	Average Temperature
23,7°C	7,7°C	16,0°C	15,6°C

Figure 5.2.5 shows the result of the EL-image of module  $\alpha$ -II, with histogram equalisation and greyscale-conversion.

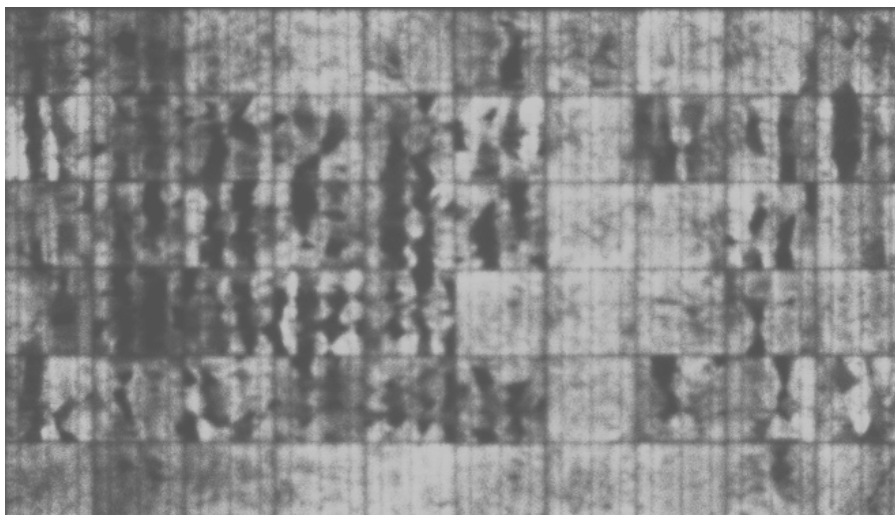


Figure 5.2.5:  $\alpha$ -II indoor electroluminescence image.

Figure 5.2.6 shows the IRT-image of the front of module  $\alpha$ -II done indoors, with forward current equal to the short-circuit current applied to the module. Table 5.2.3 shows the measured data from the IRT-image.

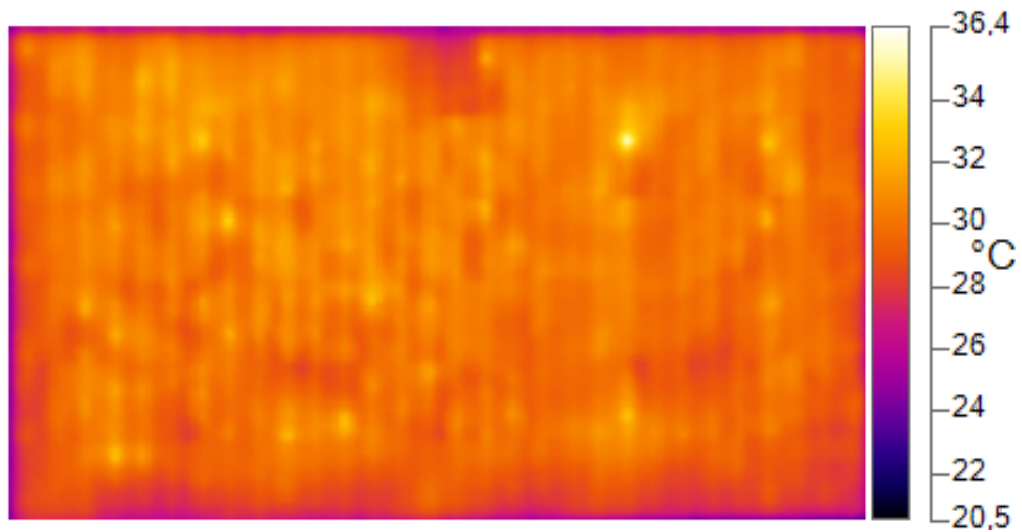


Figure 5.2.6:  $\alpha$ -II forward-current infrared image.

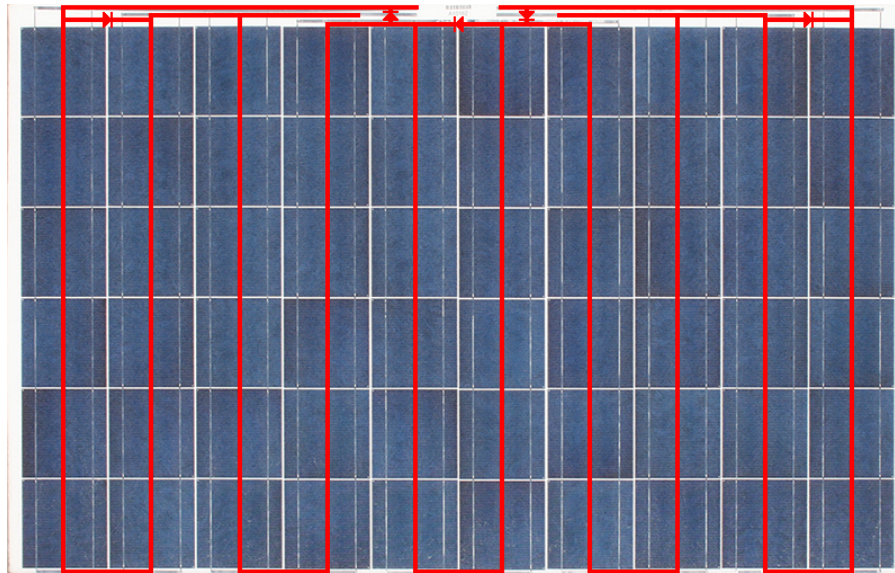
Table 5.2.3: Main temperatures of interest, indoor infrared thermography of module  $\alpha$ -II with short-circuit current applied in forward bias.

<b>Maximum Temperature</b>	<b>Minimum Temperature</b>	<b>Temperature Difference</b>	<b>Average Temperature</b>
35,7°C	25,8°C	9,9°C	29,9°C



### 5.3 Module $\alpha$ -III

This chapter addresses the results from the testing of the module with designation  $\alpha$ -III, from Elkem (ref: Table 4.3.1). Figure 5.3.1 shows a photography of module  $\alpha$ -III, with a circuit diagram overlay and an image of the bypass-diode configuration.



(a) Photography of module with designation  $\alpha$ -III, with circuit diagram overlay.



(b) Bypass diode configuration of module  $\alpha$ -III.

Figure 5.3.1: Photography of module with designation  $\alpha$ -III, with circuit diagram overlay, and crop of bypass-diode configuration.

Figure 5.3.2, and Table 5.3.1 shows the results of the IV-curve tracing of module  $\alpha$ -III. In the figure, the red and green coloured plots represent the IV-curves at STC-, and nominal conditions, respectively. Meanwhile, the orange and lime coloured plots represent the PV-curves at STC-, and nominal conditions, respectively.

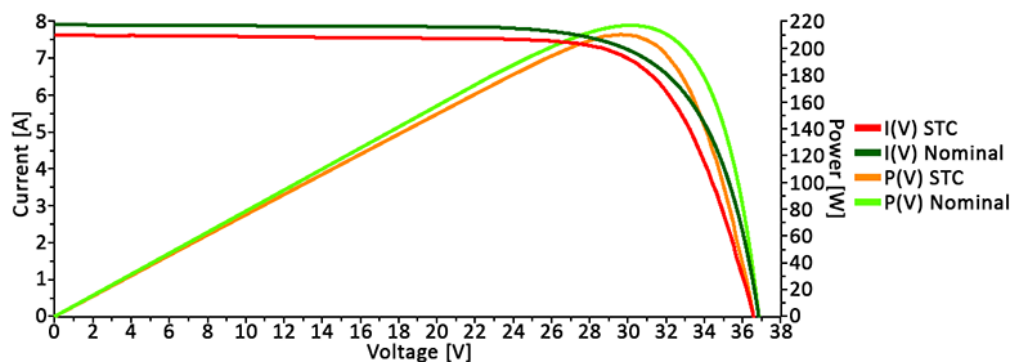


Figure 5.3.2: Current- and power- curves as a function of voltage, module  $\alpha$ -III.

Table 5.3.1: Relevant STC- and nominal values for module  $\alpha$ -III.

	STC	Nominal	Unit	Abbreviation
<b>Open-Circuit Voltage</b>	36,56	36,85	V	$V_{OC}$
<b>Short-Circuit Current</b>	7,61	7,91	A	$I_{SC}$
<b>MPP Voltage</b>	29,63	30,15	V	$V_{MPP}$
<b>MPP Current</b>	7,09	7,20	A	$I_{MPP}$
<b>MPP Power</b>	210,16	217,00	P	$P_{MPP}$
<b>Fill-Factor</b>	0,72	0,74	-	$FF$
<b>Measured PV Temperature (<math>T_0</math>)</b>		<b>Measured Irradiance (<math>G_0</math>)</b>		
15,0°C		960 $\frac{W}{m^2}$		

Figure 5.3.3 shows the UVF-image results of module  $\alpha$ -III. This image is also a compound of two images, as the torch used in this experiment was unable to illuminate the whole module.

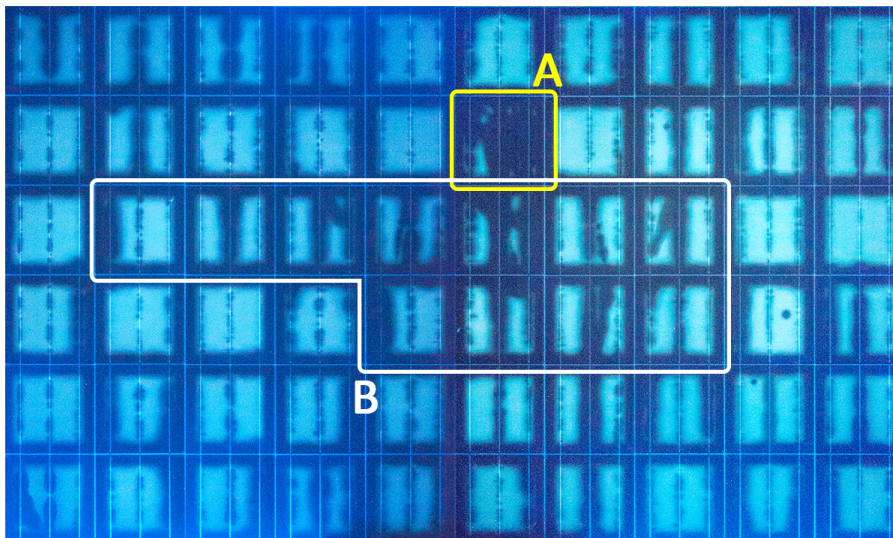
Figure 5.3.3:  $\alpha$ -III indoor ultraviolet fluorescence image.

Figure 5.3.4, and Table 5.3.2 shows the result of the IRT-imaging of module  $\alpha$ -III in outdoor, operating conditions.

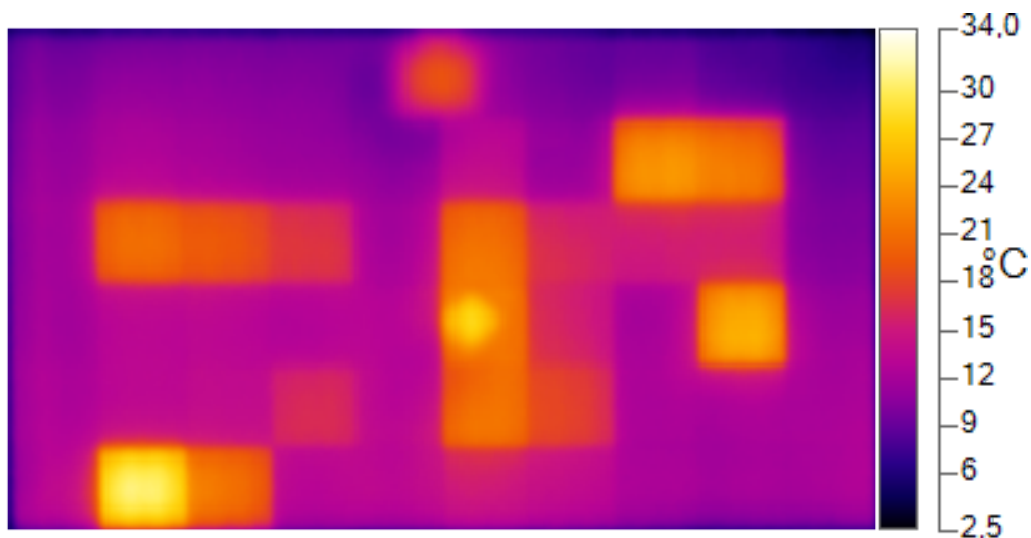


Figure 5.3.4:  $\alpha$ -III operational, outdoor infrared thermography image.

Table 5.3.2: Main temperatures of interest, outdoor infrared thermography of module  $\alpha$ -III.

Maximum Temperature	Minimum Temperature	Temperature Difference	Average Temperature
30,3°C	3,3°C	27°C	14,6°C

Figure 5.3.5 shows the result of the EL-imaging of module  $\alpha$ -III, with histogram equalisation and greyscale-conversion.

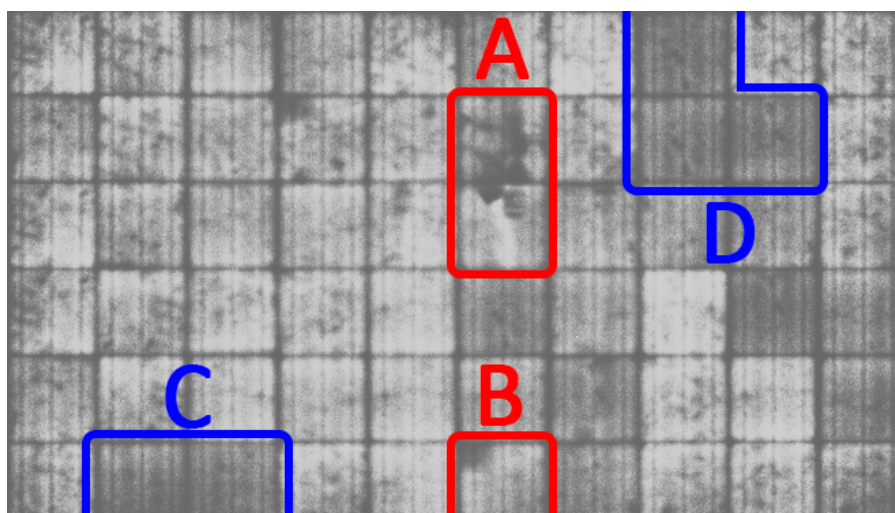


Figure 5.3.5:  $\alpha$ -III indoor electroluminescence image.



Figure 5.3.6 shows the IRT-image of the front of module  $\alpha$ -III done indoors, with forward current equal to the short-circuit current applied to the module. Table 5.3.3 shows the measured data from the IRT-image.

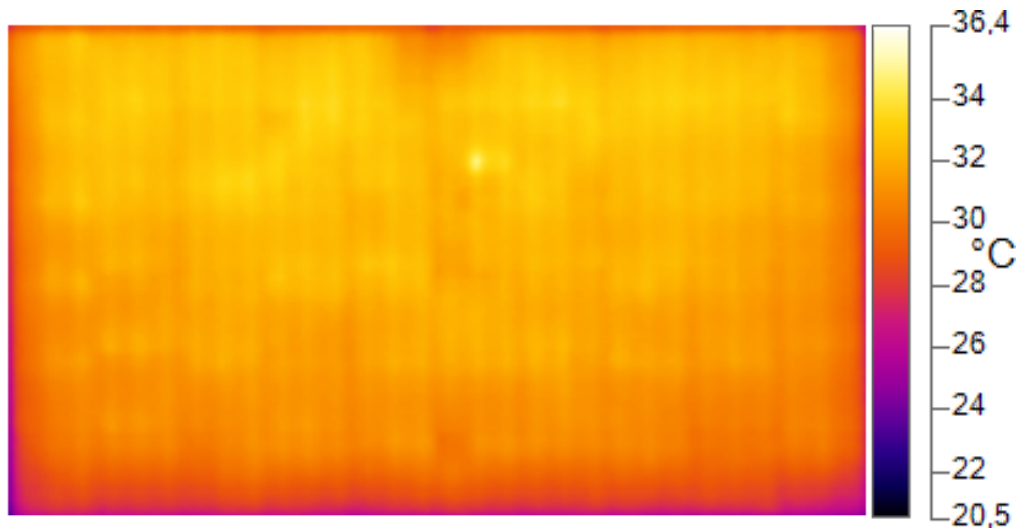


Figure 5.3.6:  $\alpha$ -III forward-current infrared image.

Table 5.3.3: Main temperatures of interest, indoor infrared thermography of module  $\alpha$ -III with short-circuit current applied in forward bias.

<b>Maximum Temperature</b>	<b>Minimum Temperature</b>	<b>Temperature Difference</b>	<b>Average Temperature</b>
35,0°C	25,8°C	9,2°C	31,4°C

### 5.4 Module $\alpha$ -IV

This chapter addresses the results from the testing of the module with designation  $\alpha$ -IV, from Westech (ref: Table 4.3.1). Figure 5.4.1 shows a photography of module  $\alpha$ -IV, with a circuit diagram overlay.

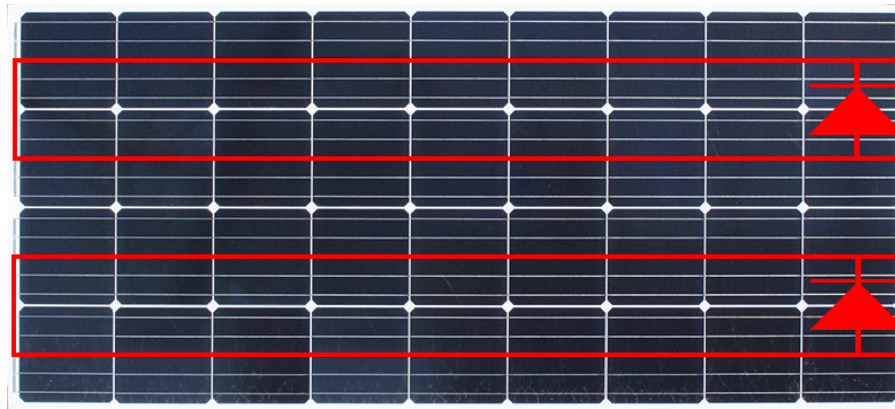


Figure 5.4.1: Photography of module with designation  $\alpha$ -IV, with circuit diagram overlay.

Figure 5.4.2, and Table 5.4.1 shows the results of the IV-curve tracing of module  $\alpha$ -IV. In the figure, the red and green coloured plots represent the IV-curves at STC-, and nominal conditions, respectively. Meanwhile, the orange and lime coloured plots represent the PV-curves at STC-, and nominal conditions, respectively. An accurate result of an altered nominal curve, as the one produced for module  $\alpha$ -I, in the same image as the STC-corrected was not possible to accurately produce, as the curves made by the HT IV-500W was only available as an image. An attempt was made to produce an altered nominal curve using the previously mentioned Simulink model, an apparent bug or insufficient understanding of the model caused the inability to produce a representative altered IV-curve.

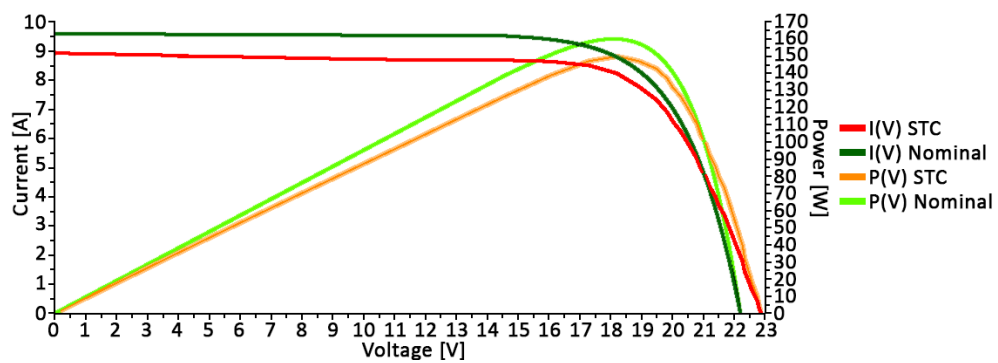


Figure 5.4.2: Current- and power- curves as a function of voltage, module  $\alpha$ -IV.

Table 5.4.1: Relevant STC- and nominal values for module  $\alpha$ -IV.

	STC	Nominal	Unit	Abbreviation
<b>Open-Circuit Voltage</b>	22,87	22,20	V	$V_{OC}$
<b>Short-Circuit Current</b>	8,87	9,60	A	$I_{SC}$
<b>MPP Voltage</b>	18,19	18,10	V	$V_{MPP}$
<b>MPP Current</b>	8,24	8,85	A	$I_{MPP}$
<b>MPP Power</b>	149,84	160,00	P	$P_{MPP}$
<b>Fill-Factor</b>	0,70	0,75	-	$FF$
<b>Measured PV Temperature (<math>T_0</math>)</b> 19,3°C		<b>Measured Irradiance (<math>G_0</math>)</b> 1015 $\frac{W}{m^2}$		

Figure 5.4.3 shows the result from the UVF-imaging experiment of module  $\alpha$ -IV, this experiment had to be done in three parts due to the UV-torch not being able to illuminate the whole module at once.

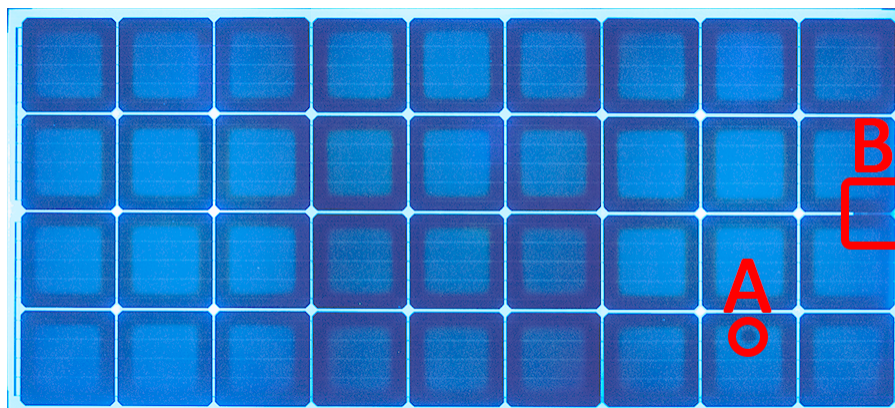


Figure 5.4.3:  $\alpha$ -IV indoor ultraviolet fluorescence image.

Figure 5.4.4 shows the result from the IRT-imaging experiment of module  $\alpha$ -IV, the related measurements are noted in Table 5.4.2.

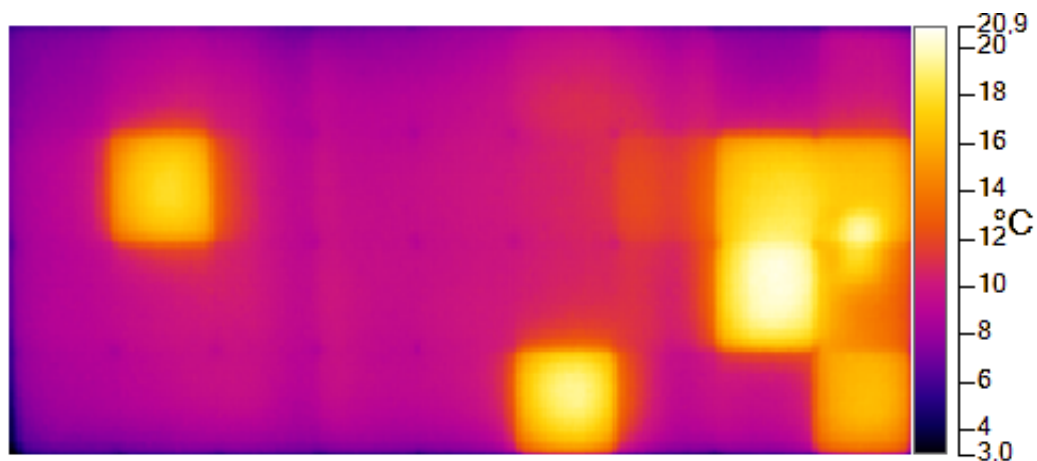


Figure 5.4.4:  $\alpha$ -IV operational, outdoor infrared thermography image.

Table 5.4.2: Main temperatures of interest, outdoor infrared thermography of module  $\alpha$ -IV.

Maximum Temperature	Minimum Temperature	Temperature Difference	Average Temperature
20,6°C	5,5°C	15,1°C	11,1°C

Figure 5.4.5 shows the result of the EL-image of module  $\alpha$ -IV, with histogram equalisation and greyscale-conversion.

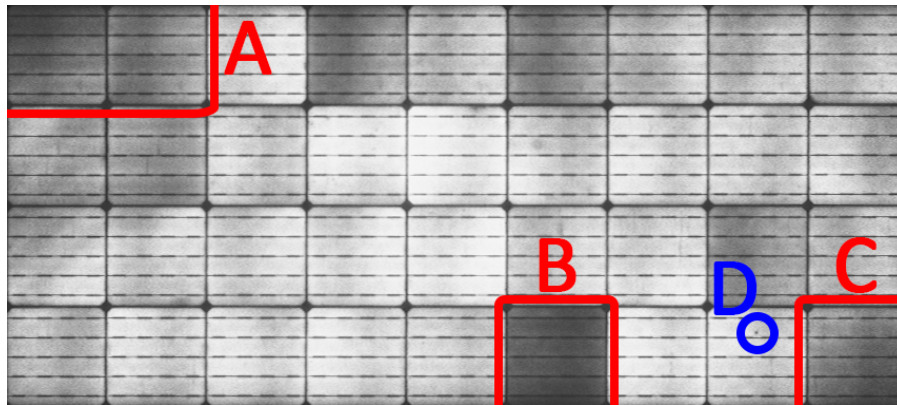


Figure 5.4.5:  $\alpha$ -IV indoor electroluminescence image.

Figure 5.4.6 shows the IRT-image of the front of module  $\alpha$ -IV done indoors, with forward current equal to the short-circuit current applied to the module.



Figure 5.4.6:  $\alpha$ -IV forward-current infrared image.

Table 5.4.3: Main temperatures of interest, indoor infrared thermography of module  $\alpha$ -IV with short-circuit current applied in forward bias.

Maximum Temperature	Minimum Temperature	Temperature Difference	Average Temperature
29,7°C	24,0°C	5,7°C	28,4°C

By using the measured temperature from the IV-trace, in combination with the temperature difference of the outdoor IRT-results, calculations were performed using Equations 8, and 9 to calculate the two extreme examples in Table 5.4.4. The manufacturer's data-sheet of the module is attached in Appendix B.

Table 5.4.4: Two extreme examples of corrected short-circuit current, and open-circuit voltage based on measured temperature, temperature difference and data-sheet values

<b>Current Temp. Coefficient (<math>\alpha</math>)</b>	<b>Voltage Temp. Coefficient (<math>\beta</math>)</b>	<b>Measured PV Temp. (<math>T_0</math>)</b>	<b>IRT Temp. Difference (<math>\Delta T</math>)</b>
+0,04 $I_{SC}(\%)$ °C	-0,35 $V_{OC}(\%)$ °C	19,3 °C	5,7 °C
<b>Characteristic</b>	<b>Nominal</b>	<b>Corrected to 25,0°C</b>	<b>Corrected to 13,6°C</b>
$I_{SC}$	9,6 A	9,6 A	10,02 A
$V_{OC}$	22,2 V	22,2 V	23,09 V

### 5.5 Module $\beta$ -I

This chapter addresses the results from the testing of the module with designation  $\beta$ -I, from Suntech (ref: Table 4.3.1). Figure 5.5.1 shows a photography of module  $\beta$ -I, with a circuit diagram overlay. The bypass-configuration of this module is unknown because of the lack of such information in the data-sheet, and the inability to open the junction-box of the module for inspection.



Figure 5.5.1: Photography of module with designation  $\beta$ -I, with circuit diagram overlay. Bypass-configuration unknown.

Figure 5.5.1, and Table 5.5.1 shows the results of the IV-curve tracing of module  $\beta$ -I. In the figure, the red and green coloured plots represent the IV-curves at STC-, and nominal conditions, respectively. Meanwhile, the orange and lime coloured plots represent the PV-curves at STC-, and nominal conditions, respectively.

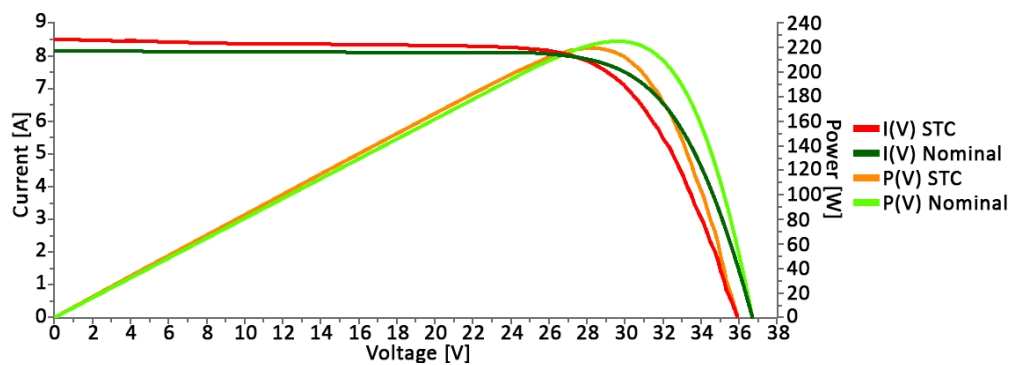


Figure 5.5.2:  $\beta$ -I current- and power-curves as a function of voltage.



Table 5.5.1: Relevant STC- and nominal values for module  $\beta$ -I.

	STC	Nominal	Unit	Abbreviation
<b>Open-Circuit Voltage</b>	35,91	36,70	V	$V_{OC}$
<b>Short-Circuit Current</b>	7,83	7,61	A	$I_{SC}$
<b>MPP Voltage</b>	28,08	29,60	V	$V_{MPP}$
<b>MPP Current</b>	7,83	7,61	A	$I_{MPP}$
<b>MPP Power</b>	219,89	225,00	P	$P_{MPP}$
<b>Fill-Factor</b>	0,74	0,75	-	$FF$
<b>Measured PV Temp. (<math>T_0</math>)</b>		<b>Measured Irradiance (<math>G_0</math>)</b>		
21,0°C		984 $\frac{W}{m^2}$		

Figure 5.5.3 shows the results from the UVF-imaging experiment performed with module  $\beta$ -I, this image is a composition of two separate halves as the UV-torch was unable to illuminate the whole module.

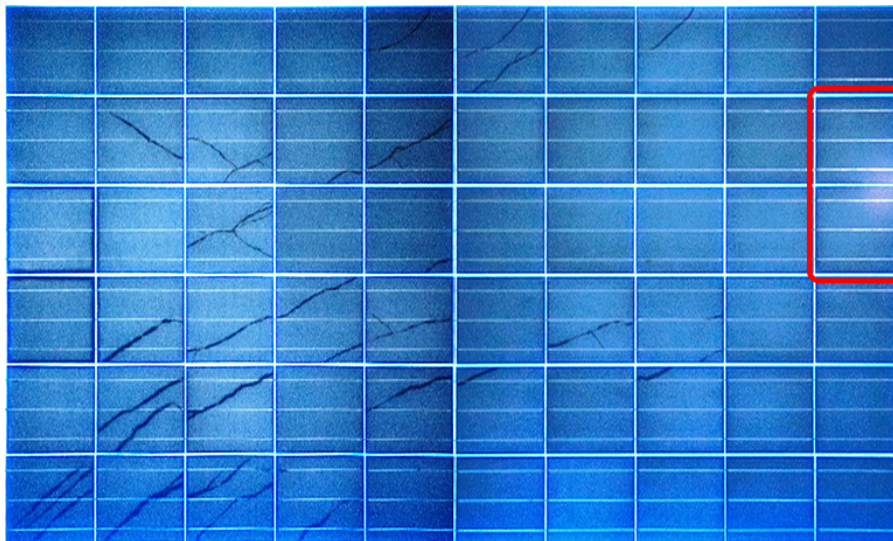
Figure 5.5.3:  $\beta$ -I ultraviolet fluorescence image.



Figure 5.5.4 shows the results from the IRT-imaging of module  $\beta$ -I, done with the FLIR camera. Table 5.5.2 shows the temperatures related to the IRT-image, determined by digital colour-matching of the image and temperature bar.



Figure 5.5.4:  $\beta$ -I operating infrared image.

Table 5.5.2: Main temperatures of interest, outdoor infrared thermography of module  $\beta$ -I.

Maximum Temperature	Minimum Temperature	Temperature Difference
41,1°C	18,5°C	22,6°C

Figure 5.5.5 shows the result from the EL-imaging of module  $\beta$ -I, with histogram-equalisation and greyscale-conversion.

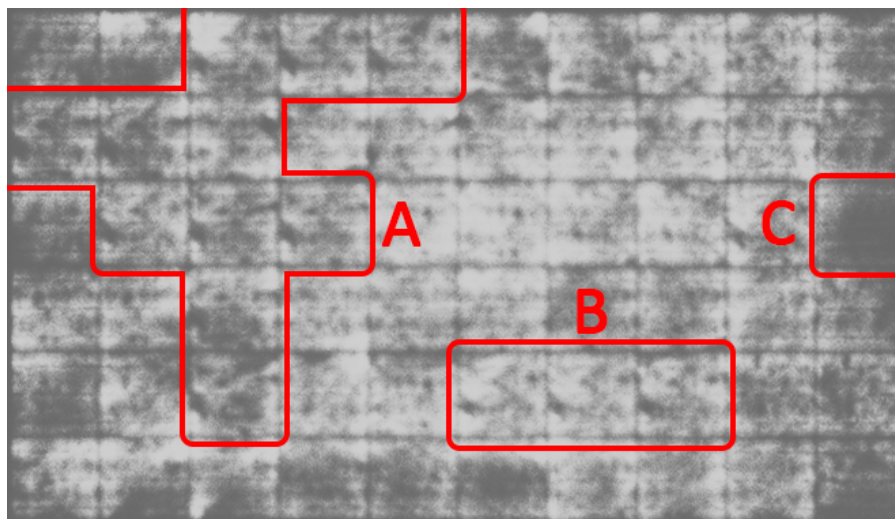


Figure 5.5.5:  $\beta$ -I electroluminescence image.

Figure 5.5.6 shows the result from the indoor IRT-imaging of module  $\beta$ -I, with  $I_{SC}$  applied in forward bias to the module. Table 5.5.3 shows the relevant measured temperatures found.

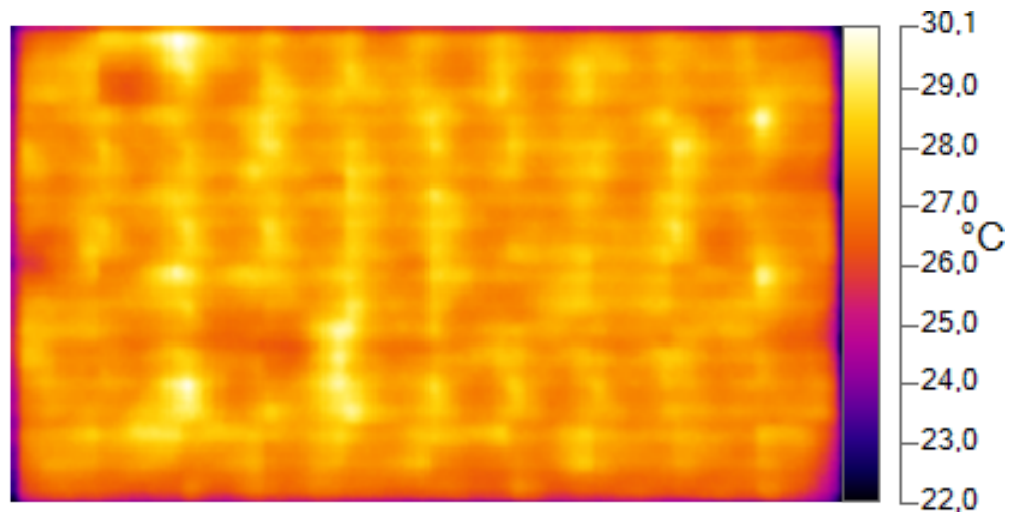


Figure 5.5.6:  $\beta$ -I forward-current infrared image.

Table 5.5.3: Main temperatures of interest, indoor infrared thermography of module  $\beta$ -I with short-circuit current applied in forward bias.

Maximum Temperature	Minimum Temperature	Temperature Difference	Average Temperature
30,1°C	23,8°C	6,3°C	27,6°C



## 6 Discussion

This chapter discusses all of the previously presented results in Chapter 5, divided into sections per module designation. First, each result is considered individually, and then all the results from each module are considered as a whole. Thereupon, the validity of the results from the experiments is discussed in Chapter 6.6. The discussion is done in relation to the results found by the experiments of this thesis and the results of the literature review in Chapter 3. This is done with the purpose of carrying the research in the field closer to a conclusion regarding the fault-detection of photovoltaic modules.

When discussing the results from the IV-tracing experiments of the modules in this chapter, the STC-corrected curves are of the measured data which is mathematically corrected to STC, with regards to measured module temperature and measured irradiance, the "nominal" curves are generated based on the data-sheet values given by the module manufacturer. Some blank pages were inserted to limit the need for back-and-forth page-turning while reading the discussion.

## 6.1 Module $\alpha$ -I

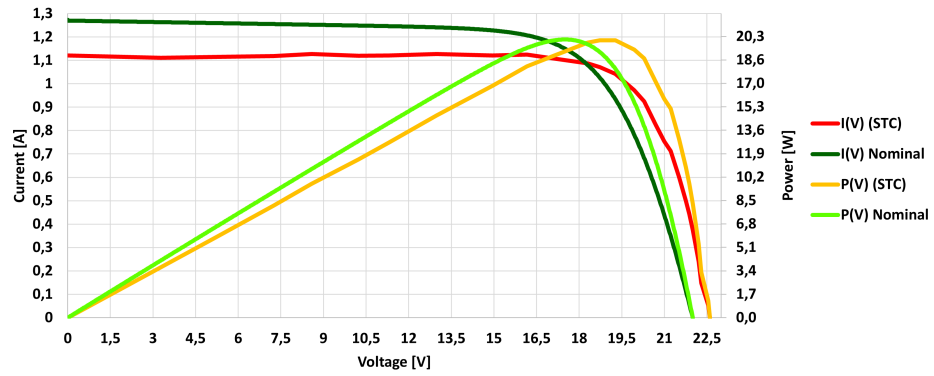
### Individual results

Figure 6.1.1 shows all of the results from each experiment performed with module  $\alpha$ -I. Based on the measured data alone, with an STC-corrected short-circuit current ( $I_{SC}$ ) of 1,12 A compared to the data-sheet value of 1,27 A, there seems to be an overall reduction in current through the module. Comparing the fill-factor (FF) of the results gives two different indications of the module efficiency, based on the STC-corrected values being compared to the curves created from the manufacturer data-sheet values and the altered values, with only a slight decrease or more significant decrease in FF, respectively. The power at STC, at MPP suggests the module is operating at 99,75%-, or 91,85% efficiency based on the manufacturer-, and altered nominal  $P_{MPP}$ . Which is a considerable difference in performance. If the first case is true, there are negligible power losses in the module, while if the second case is true, there is cause for concern as the performance has dropped to 91,85% of nominal. Given the uncertain nature of these results, they should be regarded as such to be considered as an indication of the actual performance of the module.

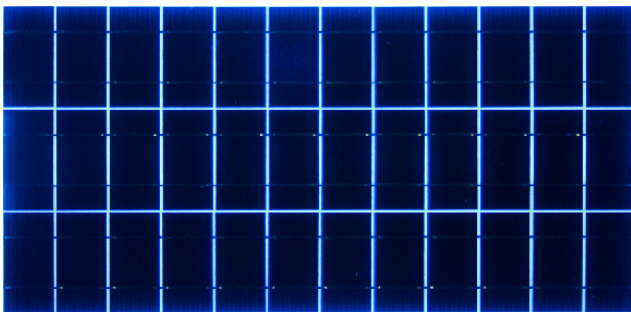
The main points of interest in the UVF-response image were the bright-spots on some of the bus-bars, which were not present on other similar modules in the rack. Figure 6.1.2 shows an image of the UVF-response of module  $\alpha$ -I, with a zoomed-in section showing both the high response spots in some cells, and the more uniform response in neighbouring cells. The cause of these spots is not certain. As mentioned in Chapter 2.8 different materials have varying UVF-response compared to each other, with this in mind there may be a substance on these spots fluorescing more than the other. This is however unlikely, as it is not a uniform pattern across the module, and these spots not being present in other modules of the same module, in the same rack. A cause that may be more likely is a higher UVF-response caused by hot-spots in these bus-bars, as discussed in the review of the work by Köntges et al. [5], in Chapter 3.4. The spots may also be caused by an irregularity in the production process, causing one side of some cells to have this specific UVF-response.

The areas of increased temperature in the IRT-image of the module might suggest that there is an increased resistance in some of the cells, causing them to generate more heat than the neighbouring cells. From the results of the EL-experiment, one can see that there are several cells in the module with areas of reduced and absent EL-response. Highlighted in box "A" seem to be two types of finger contact issues where the cells in the middle row in seem to show the presence of finger-contact issues caused by cell-cracks, while the other two cells seem to have finger-contact issues caused by improper soldering. The cells highlighted by box "B" seem to have reduced EL-response in addition to some smaller areas of no electroluminescence, suggesting that these cells also have some issues that may reduce their efficiency. As discussed in Chapter 3.3, all of the areas with lower/no EL-response may correspond to a lower power output of the cells in question, causing an overall lower module efficiency.

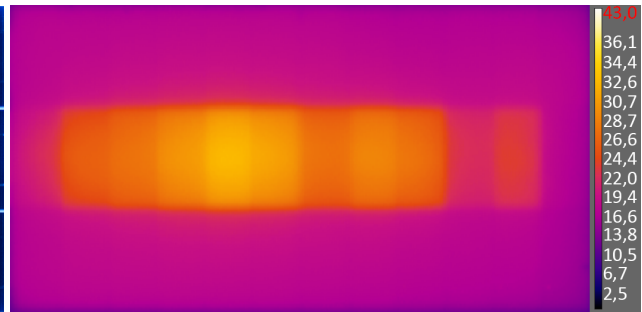
The temperature gradient across the module, in the indoor IRT-image, with heat seemingly concentrating at the top of the module, may suggest the difference in temperature being caused by the heat rising. The low amount of useful diagnostic information available in these results, may point to this method being unproductive in the diagnosis of PV-module faults.



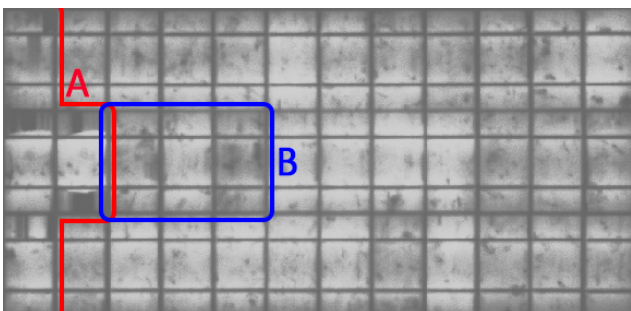
(a)  $\alpha$ -I IV-trace.



(b)  $\alpha$ -I UVF-image.



(c)  $\alpha$ -I outdoor IRT-image.



(d)  $\alpha$ -I EL-image.



(e)  $\alpha$ -I indoor IRT-image.

Figure 6.1.1: All results from experiments performed with module  $\alpha$ -I.

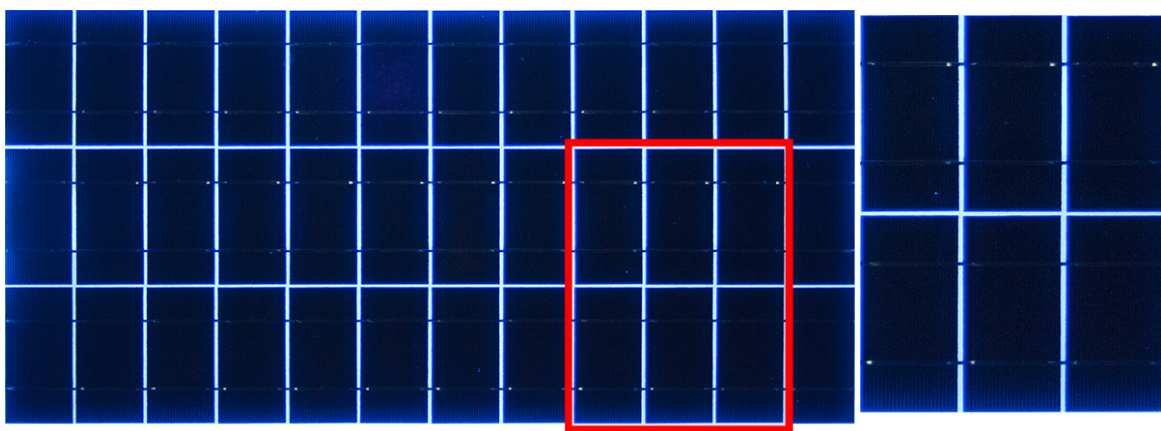


Figure 6.1.2: Indoor ultraviolet fluorescence image of module  $\alpha$ -I, with zoomed area of interest.



### Combined results

Combining the results from the IRT-, and EL-imaging gave the image shown in Figure 6.1.3, where the IRT-image was overlaid the EL-image. From this, there seems to be a correlation between the heat generation in the cells, and where the EL-image showed reduced EL-response in areas between the bus-bars, in area "A". Meanwhile, the cells with finger-contact issues, in area "B", stay cooler.

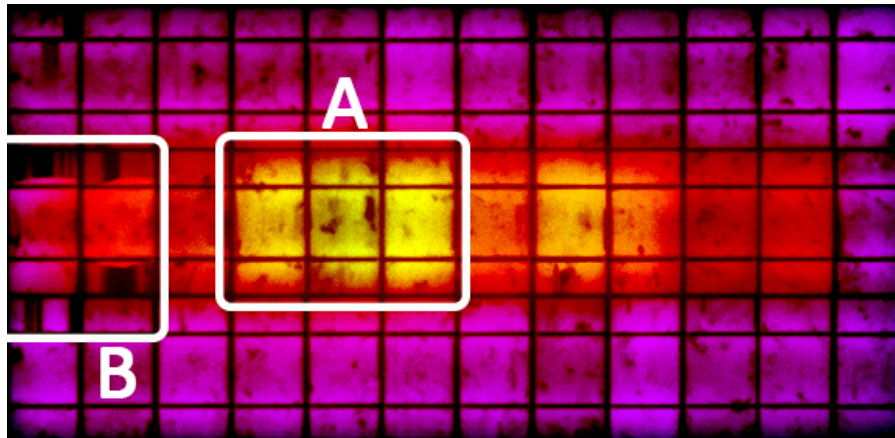


Figure 6.1.3:  $\alpha$ -I infrared thermography image overlaid EL-image.

While the UVF-image shows some spots of elevated UVF-response, it does not show any indications of the faults suggested by the other methods. The outdoor IRT-, and EL-image seem to have some correlation between them, where some of the cells in the centre row show both higher temperature and reduced EL-response. This might suggest that the cells in question have an increased internal resistance, causing both of the symptoms. The EL-image alone shows four cells on the right side of the module having cracks, causing isolated areas of the cells. All of these proposed faults may also correlate with the observed loss in short-circuit current in the manual IV-trace of the module. The indoor IRT-image of module  $\alpha$ -I does not seem to contain any information relating to the diagnosis of faults in the module. As there are no bypass-diodes in this module, each fault may have a significant impact on the overall module efficiency.





## 6.2 Module $\alpha$ -II

### Individual results

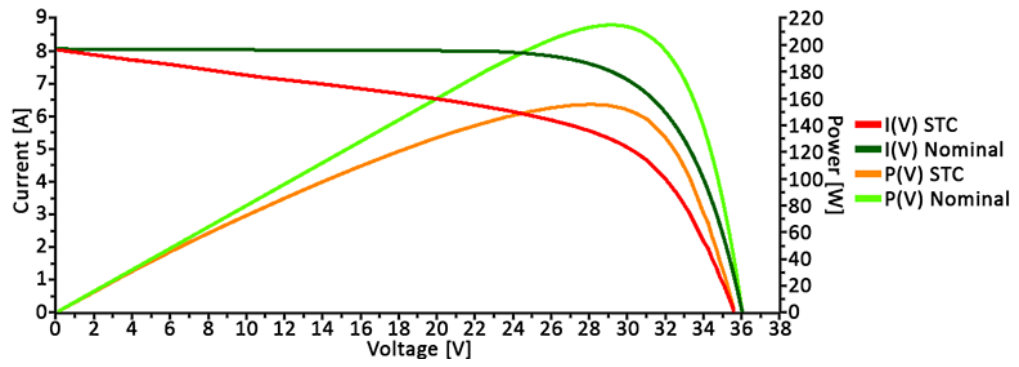
Figure 6.2.1 shows all of the results from each experiment performed with module  $\alpha$ -II. It is clear from the IV-trace results that this module suffers from some kind of fault causing the shunt resistance of the module to decrease from its nominal conditions, as according to the findings by Huang et al., discussed in Chapter 3.1. The power output at MPP in STC is at 72,38% of the rated power, which is a significant reduction of power output. The fault type causing this drop in efficiency, however, is not apparent from the IV-tracing alone. The results of the UVF-experiment show a clear reduction in fluorescence in large areas of the module, caused by ingress of water and/or oxygen, with some areas completely devoid of fluorophores. Meanwhile, there is a range of cells seemingly not affected, with high UVF-response, and cells with patterns suggesting cracked cells, as discussed in Chapter 3.4.

The temperature difference of 16°C measured in the IRT-results of this module, along with the irregular heating pattern, may also be an indication of this module being faulty. The hot spot in the top, centre of the module corresponds to the heat generated in the module's junction box. From the EL-imaging results, it is clear that this module suffers from many areas of inactivity caused by cell-cracks. The indoor IRT-test gave a more detailed result, compared with module  $\alpha$ -I, with more aggressive gradients in the areas standing out in the EL-results, as well as clear vertical stripes of heat in the bus-bars.

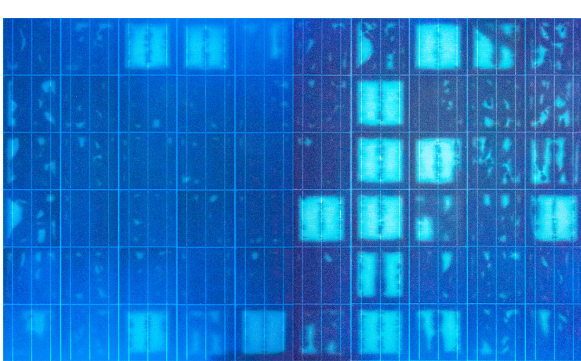
### Combined results

Figure 6.2.1f shows an image where the outdoor, operational IRT-image is overlaid the EL-image. From this image, there is correlation between the most cracked areas of the module and the heat generated within it.

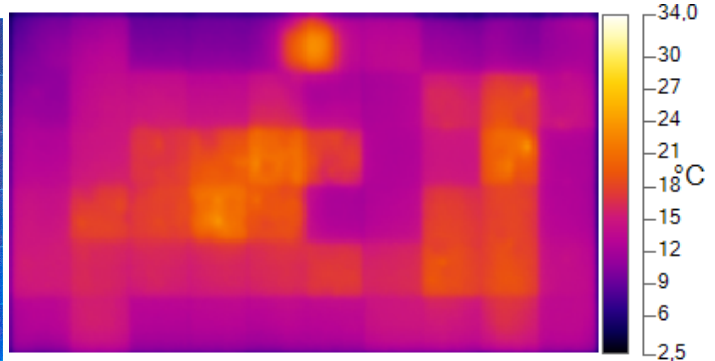
The IV-tracing of the module shows there may be extensive faults in this module, causing a significant decrease in module efficiency by means of a reduction in shunt resistance. From the experiments done with this module, there are clear correlations between the UVF-, outdoor IRT-, and EL-imaging results. The images show problems with most of the cells, and a clear difference in the column where the bottom five cells show none/few signs of faults. The indoor IRT-image also shows a more varied temperature gradient in this module, which may be caused by the extensive amount of faults present in the module. The hot-spot in the top, right corner of the indoor IRT-image seems to correlate with the isolated area of the EL- image in column 8, row 2, which may indicate a fault with high finger-contact resistance.



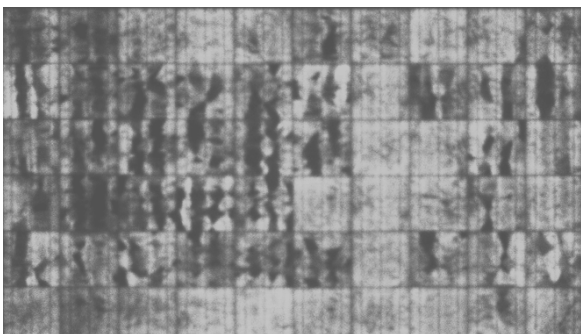
(a)  $\alpha$ -II IV-trace.



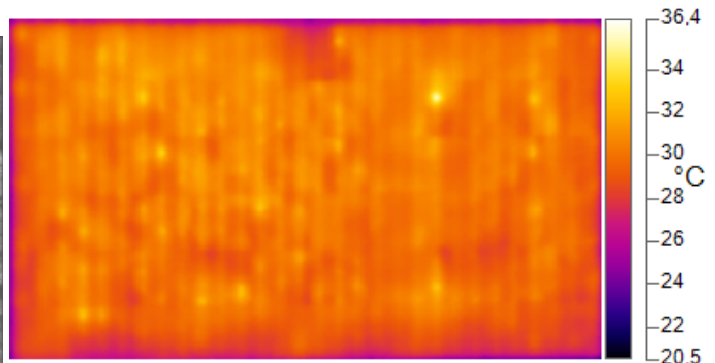
(b)  $\alpha$ -II UVF-image.



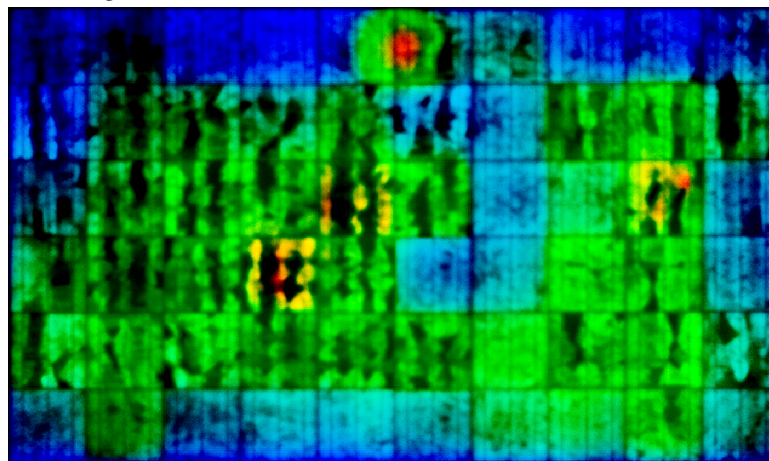
(c)  $\alpha$ -II outdoor IRT-image.



(d)  $\alpha$ -II EL-image.



(e)  $\alpha$ -II indoor IRT-image.



(f)  $\alpha$ -II IRT-image overlaid EL-image.

Figure 6.2.1: All results from experiments performed with module  $\alpha$ -II.

### 6.3 Module $\alpha$ -III

#### Individual results

Figure 6.3.1 shows all of the results from each experiment performed with module  $\alpha$ -III. From the IV-tracing results it seems that this module is operating close to nominal, at STC conditions, with a 0,30 A decrease in  $I_{SC}$ , and a 0,30 V decrease in  $V_{OC}$ . While the drop in current can be explained by a drop in excitation/recombination in the cells, such a low decrease in voltage, of less than the electric potential generated by a single cell, and may be within the uncertainty of the measurement equipment. One plausible cause of the voltage drop, is the temperature probe of the HT IV-500W being placed behind a cell with a temperature causing the calculated STC-curve to not compensate correctly according to the temperature, relative to the actual performance of the module. Another explanation for the reduction in voltage might be a reduction in shunt resistance, as discussed in the findings by Huang et al. [6] in Chapter 3.1. The power output at MPP in STC is at 96,77% of the rated power, which is a low decrease in power output.

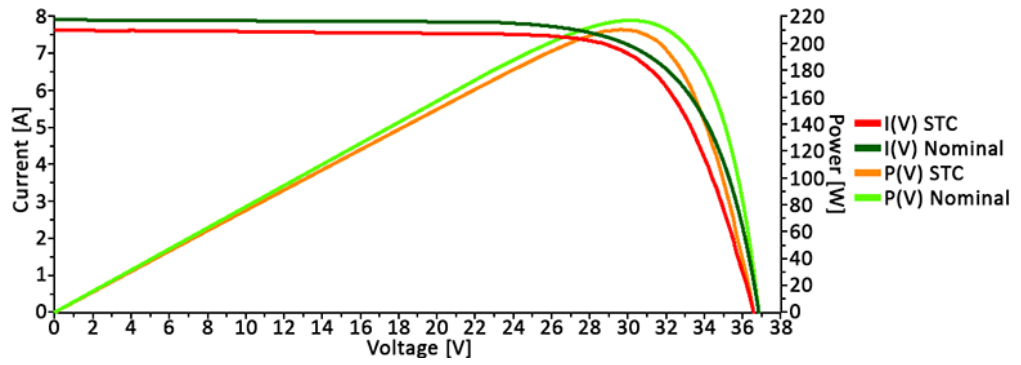
The oxygen/water ingress in this module, shown in Figure 6.3.1b, points to some cracking of the cells in the module, based on the pattern of reduced UVF-response in some of the cells. The cell in the yellow box "A" shows a clear example of where the ingress has caused nearly all of the EVA-laminate to lose its fluorescence, while the cells in the white box "B" show less reduction in fluorescence, making it possible to see the implied cell-cracks based on the fluorescence patterns, as discussed in Chapter 3.4. The wide difference, of 27°C between maximum- and minimum temperature, and the sharp gradient of temperature between some of the cells in the IRT-image, may indicate several issues present in the module. Increased resistance caused by and/or causing the hot cells, may lead to a decrease in overall module performance.

In the EL-results, there are some interesting areas. The red boxes marked "A" and "B" are some of the cells showing areas within the cell with no EL-response. The blue boxes of "C" and "D" show some of the cells with reduced overall response across the whole cell. Both of these could cause a decrease in efficiency, and the cells to have increased temperature during operating conditions as discussed in Chapter 3.6. The results of the indoor IRT-experiment show some increased temperature around the bus-bars, and a spot on one of the middle columns of cells which may indicate a fault in the module.

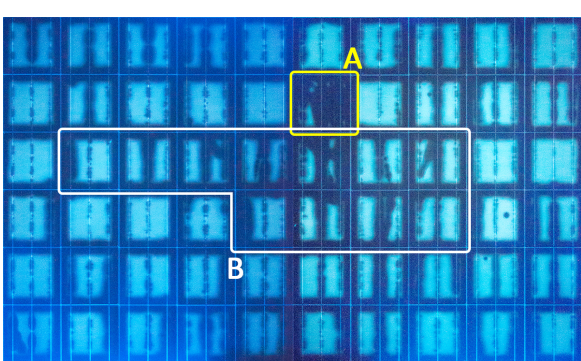
#### Combined results

Figure 6.3.1f shows the IRT-image overlaid the EL-image, where the colour range goes from blue, in cold areas to red, in warmer areas. From this, one could suggest that there may be correlations between the cracked cells and the cells with reduced EL-response and the increase in cell temperature. The IV-trace shows signs of some reduction in efficiency, through a reduction in  $I_{SC}$ . The results of the UVF-, outdoor IRT-, and EL-experiments show some correlations between each other. The blue boxes, and box "A" in the EL-image show correlation with the same areas in the IRT-image. Most of box "B" in the UVF-image shows a correlation with the IRT-image, but is not as apparent in the EL-image. The indoor IRT-image does not give a sign of any apparent faults, other than a slight temperature increase in the area of the isolated parts of the cells in box "A" in the EL-image.

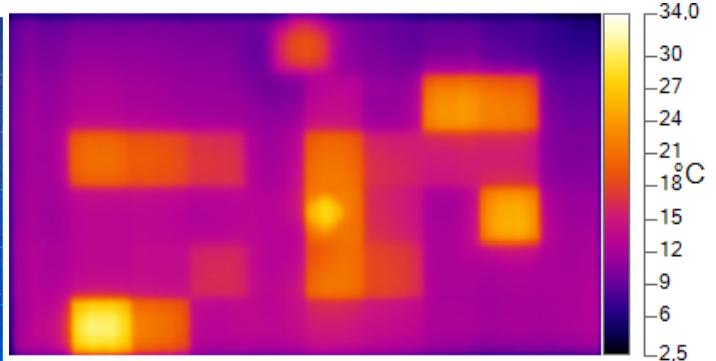




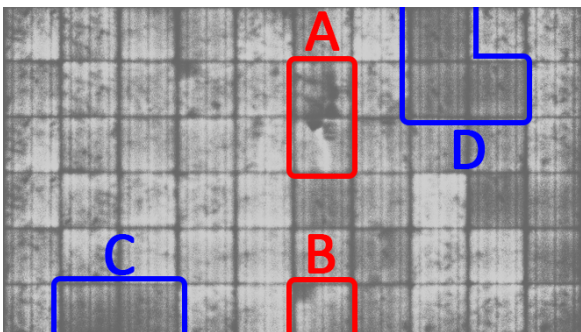
(a)  $\alpha$ -III IV-trace.



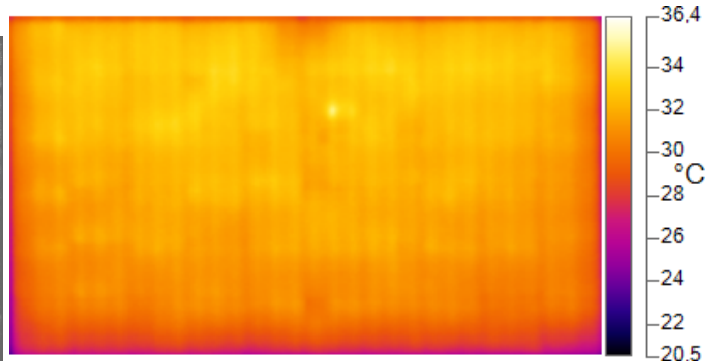
(b)  $\alpha$ -III UVF-image.



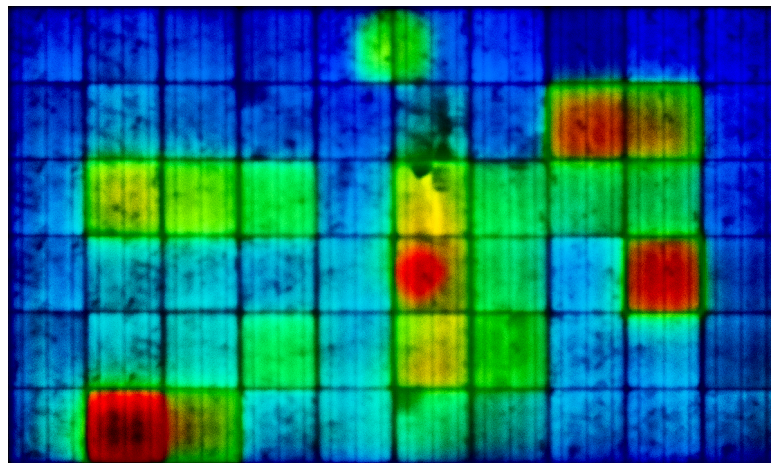
(c)  $\alpha$ -III outdoor IRT-image.



(d)  $\alpha$ -III EL-image.



(e)  $\alpha$ -III indoor IRT-image.



(f)  $\alpha$ -III IRT-image overlaid EL-image.

Figure 6.3.1: All results from experiments performed with module  $\alpha$ -III.

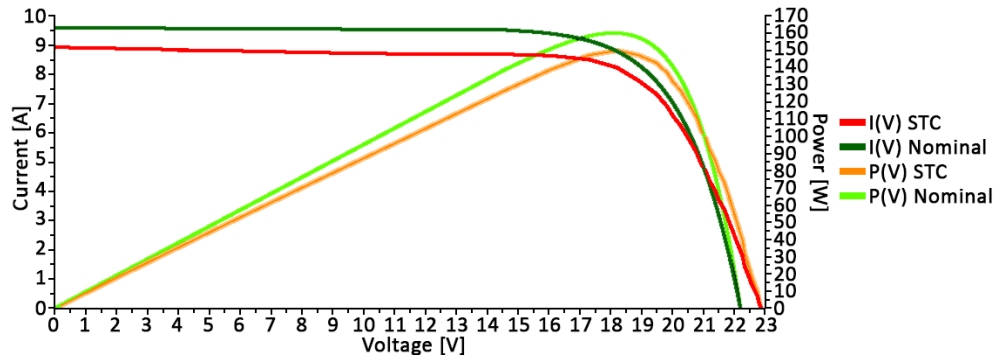
## 6.4 Module $\alpha$ -IV

### Individual results

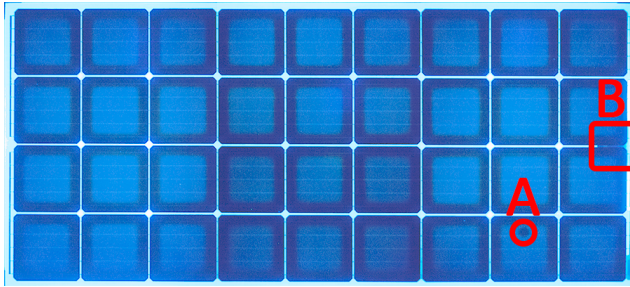
Figure 6.4.1 shows all of the results from each experiment performed with module  $\alpha$ -IV. The decrease in power output, shown in the IV-tracing results, may indicate a decrease in module efficiency. The MPP power output at STC is 93,65% of rated MPP power, which is a noticeable decrease in efficiency. Highlighted in the UVF-results, box "B" shows the area where the junction box is mounted on the back of the module, suggesting that there has been an ingress of oxygen or water through the junction box. This may be caused by sealant failure around the junction-box. The red circle "A" marks a circle of reduced fluorescence, suggesting there is a small point-crack in this spot. Both cases are possible reasons for reduced module efficiency, in the case of the junction box seal being compromised. As shown in the outdoor IRT results, there are several cells with increased temperature in this module, with a difference in temperature of up to 15,1°C. This may suggest there are issues with some of the cells, causing the increase in temperature within them as discussed in Chapter 3.2.

Highlighted in the EL-results, the red boxes of "A", "B", and "C" show examples of cells with reduced EL-response, suggesting there might be some issues with these cells. The blue circle "D" highlights a spot on the EL-image, suggesting a small point-crack with a small spot of no EL-response, which may develop over time to a more serious fault of extensive cracking. As with module  $\alpha$ -I, the indoor IRT-imaging method does show a very uniform temperature gradient with signs of the heat rising to the top of the module. Therefore this image does not seem to give sufficient information to diagnose faults in the module.

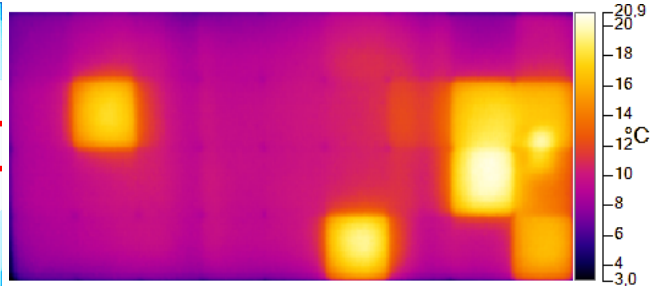




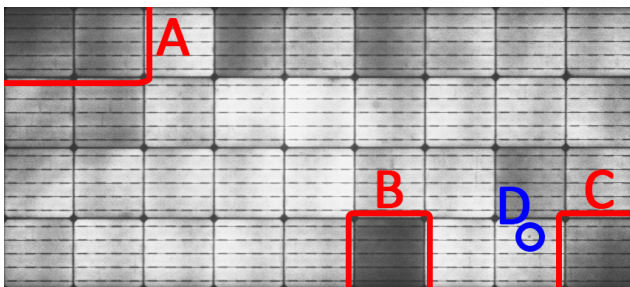
(a)  $\alpha$ -IV IV-trace.



(b)  $\alpha$ -IV UVF-image.



(c)  $\alpha$ -IV outdoor IRT-image.



(d)  $\alpha$ -IV EL-image.



(e)  $\alpha$ -IV indoor IRT-image.

Figure 6.4.1: All results from experiments performed with module  $\alpha$ -IV.

### Combined results

Figure 6.4.2 shows the IRT-image overlaid the EL-image from the experiments with module  $\alpha$ -IV. This made it easier to visually correlate some of the findings from both of the images, and the opposite for other findings. The two hot cells on the lowest row also correlate with a decrease in EL-response, as did the cell with most of the area coloured in white. The other cells with above-average temperature are however not as visibly differentiated in the EL-image.

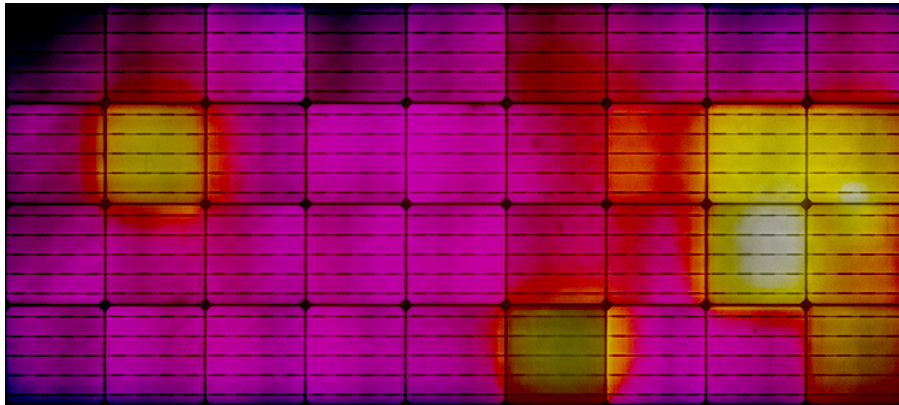
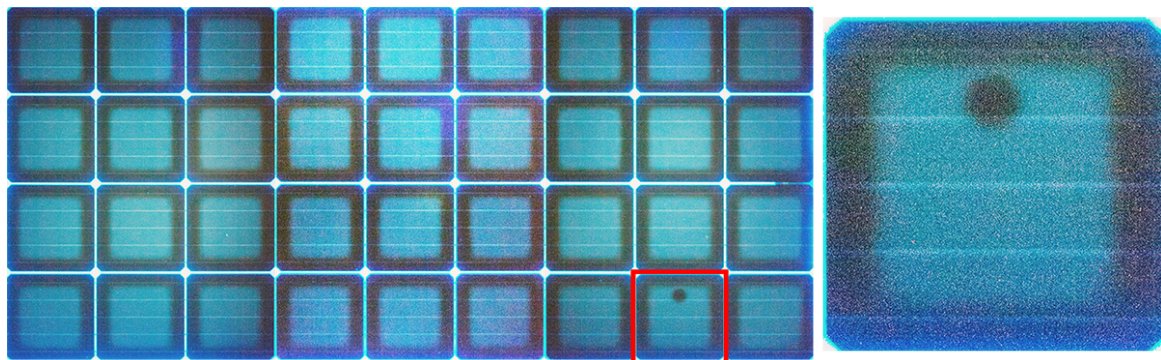
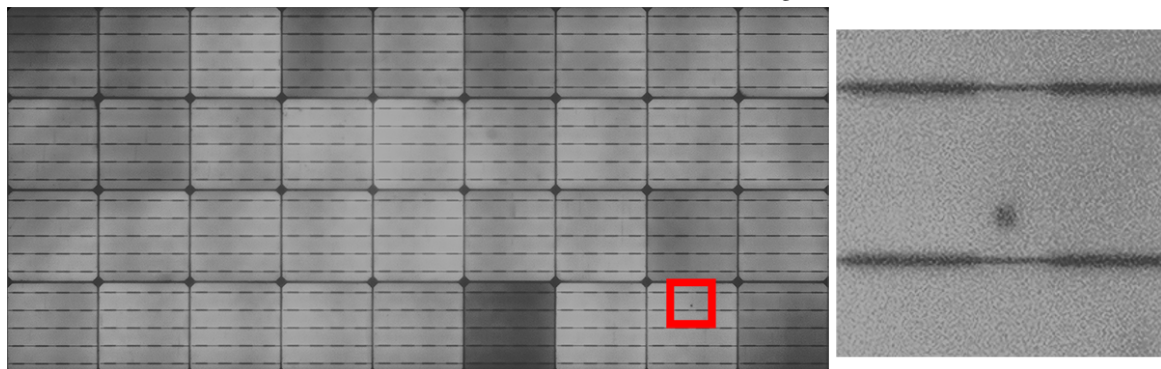


Figure 6.4.2:  $\alpha$ -IV infrared thermography image overlaid EL-image.

Figure 6.4.3 shows the two EL-, and UVF-imaging results with highlighted and zoomed-in sections of the cell with what seems to be a point-crack or puncture point through the cell. This shows an example of a condition where the UVF-imaging may make it easier to spot a fault in the module, as the EL-image only shows a small spot while the UVF-image shows a more prominent spot.



(a)  $\alpha$ -IV ultraviolet fluorescence zoom image.



(b)  $\alpha$ -IV electroluminescence zoom image.

Figure 6.4.3: Highlighting of ultraviolet fluorescence- and electroluminescence image, point-crack in module  $\alpha$ -IV.

The IV-trace shows a reduction in module efficiency caused by a reduction in  $I_{SC}$ . The trace also shows an increase in  $V_{OC}$ , which may be caused by the temperature probe reading a lower temperature than what would correct the measured data correctly to STC. This is also supported by the calculations done of voltage-, and current-correction noted in Table 5.4.4. If this is the case, this may also explain some of the reduction in  $I_{SC}$  as higher temperatures decrease the measured  $V_{OC}$  and increase the measured  $I_{SC}$ , as discussed by Huang et al. [6] in Chapter 3.1. The UVF-, and outdoor IRT-images only seem to correlate between them by the areas where the junction box is located on the module, highlighted in box "B" in the UVF-image. The IRT-image show no signs of the spot highlighted in circle "A" in the UVF-image. Between the UVF-and the EL-image, there seems to be some correlation between only the spot marked with circles in both of the images. This could be a point-crack which may not affect the performance of the module yet, but could develop into a more significant fault with a larger isolated area, as the module is exposed to variations in temperature through the years. The lower EL-response in box "A" does not correlate with any of the other images. The three hot cells not in the 2 by 2 cluster directly in front of the junction box, does also show a reduced EL-response. The two cells on the lowest row, highlighted by box "B" and "C", show a significant reduction in EL-response, suggesting a significant reduction in current through these cells.

## 6.5 Module $\beta$ -I

### Individual results

Figure 6.5.1 shows all of the results from each experiment performed with module  $\beta$ -I. From the IV-tracing curves, there seems to be an increase in  $I_{SC}$ , and a decrease in  $V_{OC}$  which may suggest that there has been a measurement error when performing this experiment. The MPP power output of the module at STC is 97,73% of rated MPP power, which is a small decrease in efficiency. The STC-corrected curves could however suggest that there was an erroneous measurement of incident irradiance and/or module temperature, causing the correction of the measured current to exceed the nominal values. An erroneous measurement of cell temperature could also cause the open-circuit voltage to be lower than expected. 26 of the cells in this module show UVF-patterns suggesting cell-cracks, which may cause these cells to not perform as well as they could. This crack pattern shows some similarities to the presented results from IEA-PVPS T12-01:2014 report [12] in Chapter 3.3, where the module had experienced a heavy mechanical load on the middle of the module plane, suggesting that this may have happened to this module as well. Highlighted in the red box is an area of two cells with what seems to be an increased UVF-response which may be caused by excessive heating of the cells in question, as discussed around the findings by Köntges et al. [5] in Chapter 3.4.

The results of the outdoor IRT-experiment show a scattered image of several cells having a higher cell-temperature compared to the other cells, with a maximum difference of 22,6°C. This may suggest that there are several cells with issues, as discussed in Chapter 3.2. The boxes "A", and "B" in the EL-image highlights some cells with similar patterns of isolated areas. This may suggest that these cell-wafers have been cut from the same ingot, with a fault line running through the length of the ingot, causing the same isolated area to appear in the same spot in all of the cells. Box "C" highlights a cell with significantly lowered EL-response, compared to the other cells. This could suggest there being a short in this cell, or finger contact issues across most of the cell. These faults could reduce the overall efficiency of the module, as discussed in Chapter 3.3.

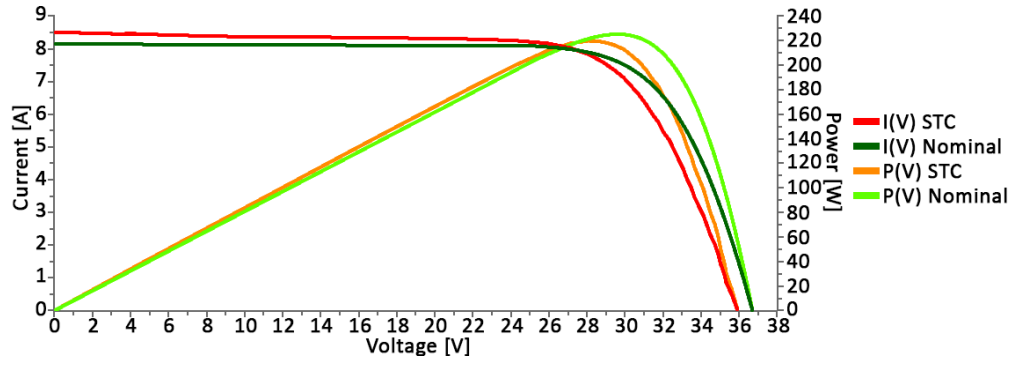
As with the other experiments in this category, there is not a lot of information that can easily be gathered from the indoor IRT-imaging result, as the temperature gradient across the module seems too uniform to give sufficient data for visual analysis.

### Combined results

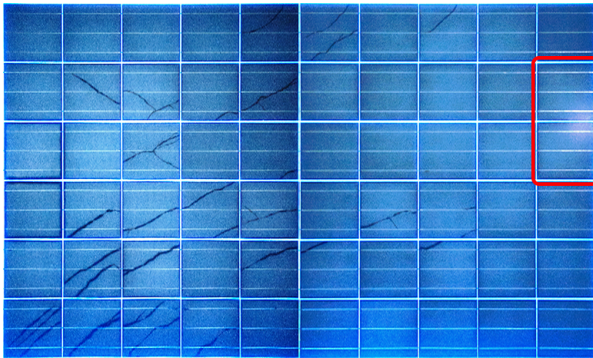
Figure 6.5.1f shows the result from the IRT-imaging, overlaid the result from the EL-imaging of module  $\beta$ -I. The most obvious from this image is the cell on the right side of the module, where there is a significant temperature difference from the rest of the module, suggesting there may be a serious issue with this cell.

While the UVF-image may not correlate fully with the IRT-image where the crack pattern is visible in the UVF-image, it does seem to correlate by means of the hot-spot highlighted with a red box in the UVF-image as these cells are the hottest measured in the IRT-image. This hot-spot does also seem to correlate with the low response cell highlighted in box "C" in the image from the EL-experiment. There also seems to be a correlation between the luminosity of the cells in the EL-image and the cracked pattern in the UVF-image.





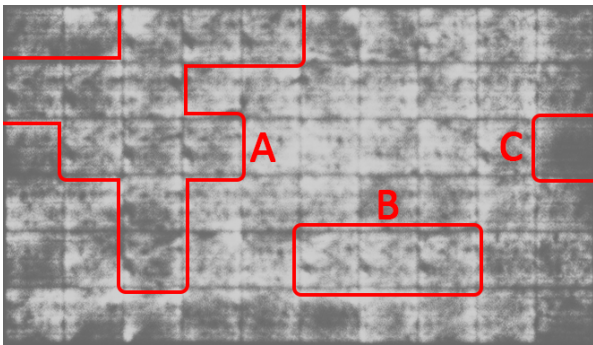
(a)  $\beta$ -I IV-trace.



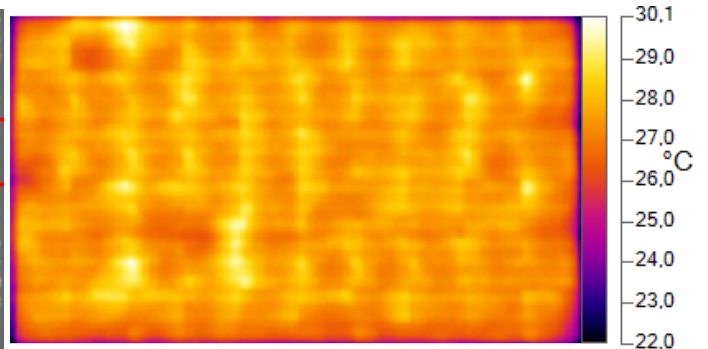
(b)  $\beta$ -I UVF-image.



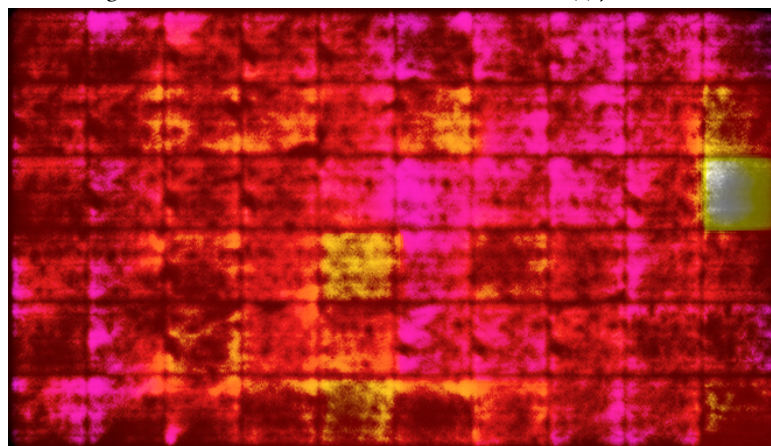
(c)  $\beta$ -I outdoor IRT-image.



(d)  $\beta$ -I EL-image.



(e)  $\beta$ -I indoor IRT-image.



(f)  $\beta$ -I IRT-image overlaid EL-image.

Figure 6.5.1: All results from experiments performed with module  $\beta$ -I.

## 6.6 Fault Detection Validity

This part of the discussion addresses the various factors that may negatively affect the validity of the results, based on each technique. All of the techniques are addressed in order of IV-tracing, EL-imaging, UVF-imaging, IRT-imaging, and visual inspection.

The method of manual IV-tracing of modules brings with it an inherent reduction in validity, as all the resistance adjustments and measurements are done manually. In this case, the Fluke 179 TRMS digital multimeter only had a resolution of  $0,1\Omega$  when measuring resistance. This low resolution could easily affect the final results, as it is used to calculate the current by dividing the measured voltage across the resistor by the measured resistance. Common for both the IV-tracing done manually and those done with the HT IV-500W, are the measurement of module temperature and incident irradiation. The reference cell could be interpreted incorrectly in the case of it not being properly calibrated, which in this case had not been done in the last ten years. The temperature probe of the HT IV-500W only measures the temperature of one spot on the back-plate of the module, this does not give the specific temperature of the cell as the heat has to be conducted through the back-plate. In cases of widely differing temperatures in the module, as seen in many of the presented results, the temperature probe only measures one spot which could widely differ from other cells in the module. These issues of incident irradiance and temperature measurements does affect the STC-correction of the measured IV-, and PV-curves as they are used to calculate the STC-corrected data from the measured data.

The main concern with the validity of the EL-results is the difficulty with focusing the camera, as the EL-response from the modules were too low to get a clear image while in the "Live View"-mode of the software used to control the camera. Focusing the camera with the lights in the room turned on, and the filters removed from the lens before performing the experiments did not succeed in getting a proper focus. Long exposure time and high ISO-setting on the camera can also introduce issues with noise and/or sensor saturation. The issues regarding the camera setting are also a viable concern when considering the validity of the UVF-results. In addition to this, the UV torch should ideally be able to illuminate the whole module evenly, when performing the UVF-imaging. Instances of the front of the module having a broken seal could also cause issues with low UVF-response across the module, without there necessarily being any other faults in the module. There is also a real concern of validity, based on the time a module needs to be exposed to UV-radiation for the fluorophores to be generated. There is also a concern of if ingress of oxygen/water has been going on long enough for the photobleaching to be noticeable, in cases of for example cell-cracks.

IRT-imaging has a validity concern when it comes to image resolution, as the cameras with high-resolution IRT-capabilities are expensive. There is also a concern regarding the operating temperature range, as the camera has to be capable of accurate imaging within the temperatures typical for PV-modules to produce viable results. Image-noise is also a concern with accurate IRT-imaging, as the more advanced IRT-cameras include a sub-ambient cooling system for the sensor to mitigate noise in the results.

As the analyses of the results are all done by visual interpretation, except for the module efficiency regarding power output. There is a clear concern regarding the validity of these analyses, as without sufficient experience one might not be able to spot and/or separate one fault-type from another.



## 6.7 Method Comparison

This part of the discussion addresses each fault-detection technique explored in this thesis, their ability to facilitate the detection of faults, which types of fault they are able to detect, how convenient they were to perform, and their validity. Equipment cost is not taken into consideration in the discussion. From the results, there was a varying degree of correlation between the different techniques for modules with seemingly similar fault-types. An example is the comparison of the IRT-, and EL-results from modules with cracked cells, where some of the instances of cracks seemingly cause higher temperatures than in other cracked cells.

### Infrared Thermography Imaging

Based on the experience gained in the process of creating this Master's thesis by utilising IV-tracing, UVF-imaging, IRT-imaging, and EL-imaging, the technique most convenient to use in spotting faulty modules in a PV-farm setting, seemed to be the outdoor IRT-imaging of operating PV-modules. This is based on the presumption of there being enough space in front of the module, allowing for the camera operator to get a good image of the module with the lens angle on the IRT-camera. With this technique, one could scan over many modules in a relatively short amount of time to check for any modules with high temperature differences either within one module, or between modules in the same string. By manually setting the minimum-, and maximum temperatures, it may become possible to characterise the modules at a faster pace as one could look for areas exceeding the set parameters of the temperature scale, for further investigation.

This technique also has the advantage of being easily done while the PV-farm is in operation, and in daylight within normal work-hours. There may also be a possibility of mounting one or more IRT-cameras to UAVs, for easier and faster access to the optimal viewing angle when performing IRT-imaging of the modules, as UAVs have been used to perform EL-imaging [26]. In some cases, there is also a possibility of automation of temperature alarms based on the IRT-image and the temperature metadata within the raw file from the IRT-imaging results. Based on the results of the experiments performed in this thesis, and the literature review done of current research in the IRT-imaging field, it seems to be a technique which is very versatile in detecting that there may be a fault in the module, but does not always allow for spotting which type of fault the module is suffering from. The outdoor IRT-imaging of operational PV-modules does require the meteorological conditions such as incident irradiance, wind speeds, cloud coverage, etc. to be within a certain range as recommended by the relevant IEC-standard [4].

The experiments performed of indoor IRT-imaging of modules with a supplied short-circuit current and 110% open-source voltage in forward-bias gave results that were seemingly not as usable in the fault-detection process. This is based on the resulting temperature gradient being too uniform, and not giving enough information about the faulty cells of the module to be able to spot the issues via visual analyses of the results.

### Ultraviolet Fluorescence Imaging

The second-most convenient technique seemed to be the nighttime UVF-analysis of the modules. This is based on this technique being able to be performed with a hand-held UV-torch while doing a visual inspection of the module using eyesight only, after dusk. This does however rely on the encapsulant being of the kind, and grade of degradation that allows for a UVF-response visible to the naked eye. There may also be a possibility of utilising a UAV-based system, with a camera and UV-source, for easier and faster UVF-imaging of the modules, as UAVs have been used to perform EL-imaging [26]. The research performed seems to support that for better results from using UVF-imaging, the experiments should be done either in a dark laboratory, or it could be done outside with low amounts of other sources of light than the UVF-response from the module itself. Whichever of these methods is used, a stabilised camera with a long shutter-speed seemed to be able to produce results better suited for analysis.

Based on the results of the experiments performed in this thesis, and the literature review done of current research in the UVF-imaging field, the technique seems to be a good approach to spot modules with issues of cracks, optical degradation, and/or hot-spots over a period of time, as to allow the photobleaching, or further degradation of the encapsulant. As seen in the presented results, UVF-imaging could also show what is seemingly cell-cracks, which may be developed in such a direction or to such an extent as to not affect the efficiency of the module. The technique may however also be used to get a warning of possible future efficiency-affecting issues with the module. Combining this method may be a good way of determining when/if a PV-module should be considered for further, more definitive testing.

### Current-Voltage Tracing

The process of outdoor IV-tracing of a module could give a lot of information on how the PV-module being tested is performing, and is the only method in this thesis which produces numerical data on the performance of the module. With the added ability of automatic STC-correction of the measured data, via the measurement of the incident irradiation and module temperature at the time of measurement. This does, however, seem to introduce a validity concern in the measured conditions as both instruments need to be calibrated for the results to have a high grade of validity. There is also the concern of measuring the correct temperature of the module, as a faulty module may present a wide range of temperatures depending on behind which cell the temperature measurement is performed. Outdoor IV-tracing also requires the module to be disconnected from the string during the whole measurement process, hindering it and all modules connected in the string to supply current to the grid to which the PV-farm is connected. If the PV-plant is not equipped for automatic IV-tracing of each module, this would require a technician to perform the IV-tracing of each module. This may not be desirable as it would require a lot of work, depending on the amount of PV-modules requiring the characterisation by IV-tracing.

Another possibility of outdoor IV-tracing is by performing a manual analysis by use of a variable load resistance, and instruments capable of measuring resistance and voltage. The method entails the measurement of both voltage and the set resistance of the variable resistor and later calculating the current and power supplied by the module in question. By measuring the module temperature

and incident irradiation, one may also perform STC-correction of the measured data. This process introduces some issues regarding the validity of the results, as the measurements are done manually. Additionally, this process is more time consuming than the one done with the automatic IV-tracer. As the calculated current through the module is a product of the voltage and the inverse of the resistance, and the power being a product of the measured voltage and the calculated current, the accuracy of the calculated results may be low. All of the results are dependent on the accuracy of the manual measurements and the logging of these data-points. Because of these issues, this technique may not be recommended as there may be too many concerns with the validity of the results. Another possibility of performing IV-tracing experiment on a PV-module is an indoor laboratory flash-test of the module. Besides requiring the module to be brought to a suitable laboratory, this could eliminate the validity concerns regarding the measurement of incident irradiance and module temperature, as both could be controlled in a laboratory-setting. This process also eliminates the concerns regarding the meteorological conditions required for outdoor IV-tracing, such as not exceeding the recommended cloud coverage, or the incident irradiance not being high enough or at the required angle relative to the module plane. These conditions are described in the recommended ranges by the relevant IEC-standard [40].

### **Electroluminescence Imaging**

In this thesis, indoor EL-imaging of the selected modules was performed. This technique seemed to be able to produce results of high quality in terms of being able to spot cracks, isolated areas, defective bypass-diodes, crystalline defects, and cells or areas of cells with different degrees of reduced EL-response. With sufficient equipment and software, one could be able to perform high-resolution analyses of PV-modules and any of the fault-types described in the literature review in Chapter 3. This would, however, require the module to be disconnected from its string, and brought to a laboratory with suitable equipment for this kind of testing.

An alternative technique is outdoor EL-imaging, with two possible methods. The first method requires two images of each module, one with- and one without the DC-current applied to the module. The image without applied current is then subtracted from the other image in post-processing, this method results in none or minimal amounts of stray light in the results. There is also the possibility of daylight imaging with the use of a UAV-based method. Alves dos Reis Benatto et al. [26] utilised a UAV-based method in which they could spot disconnected cell regions at a scale larger than the variations caused by the crystalline nature of multi-crystalline modules, at a rate of 120 frames per second. By subtracting the background, adjusting perspective by module edge detection, and movement compensation done via an algorithm, usable EL-results seem to be obtainable. By using both AC- and DC modulation, one could obtain even better results by avoiding irradiance interference from the sunlight [8].

Given the complexity and time required to utilise this technique, it may be suggested that EL-imaging techniques should only be used with modules already suspected of containing faulty cells, or in cases where there is a need for specifying exactly the reason why a module is not performing as advertised.



## 7 Conclusion

Five field-aged photovoltaic (PV) modules with different types of faults have been tested, utilising the techniques of automatic/manual current-voltage (IV) tracing, ultraviolet fluorescence (UVF) imaging, infrared thermography (IRT) imaging, and electroluminescence (EL) imaging. The results show all of the selected modules having faults of varying severity, and varying grades of evidence depending on the technique used for identifying them.

Of the literature review, and experiments performed it was found that faults related to cell-cracks, isolated cell-areas, circuit issues, resistance issues, hot-spots, defective bypass-diodes, potential induced degradation, and optical degradation can be diagnosed using the imaging techniques discussed in this thesis. It was also found that IV-tracing is the only method resulting in numerical performance-characteristic of the module. The amount of correlation between results from different techniques was found to have a varying degree of correlation between modules with seemingly similar faults.

Outdoor IRT-imaging of operational modules was found to be the most convenient technique for detecting that there may be a fault in a given module, as the process can be done efficiently, and easily in daylight conditions. This technique should be used to assess if the state of the module requires further testing, or if it should be replaced in severe cases of over-heating. Performing indoor IRT-imaging of modules supplied with forward-bias current did not produce a temperature gradient appropriate for fault detection in the PV-modules.

UVF-analysis of PV-modules was found to be a good method for detecting some faults affecting the module-efficiency, and faults that could develop over time. UVF should be used in combination with IRT-imaging to assess the need for further testing of the module.

IV-tracing requires the module to be disconnected from the string for the duration of the tracing. This could be done with automated systems, or by a technician testing the module with a suited apparatus, where the first alternative could be done more efficiently than the last. Performing manual IV-tracing of a module is not recommended as this introduces several concerns in regards to the validity and accuracy of the results. Performing IV-tracing of a module with widely differing cell-temperatures is not recommended, as the accuracy of the STC-correction depends on accurate module-temperature measurement. Indoor IV-characterisation of a module using a flash-tester would give more reliable results, but requires the module to be transported to a laboratory with the required equipment.

High resolution EL-imaging of a PV-module is able to produce results giving definitive results about the state of the module in terms of cracks, isolated areas, defective bypass-diodes, crystalline defects, and cells or areas of cells with different degrees of reduced EL-response. This process does require the module to be transported to a suitable laboratory for testing by removing the module from the string, or to be done at night with forward current applied to the module. This technique is recommended only if the previous test methods were unable to determine if the module should be replaced, or to more accurately determine the type of fault causing the module to perform at reduced efficiency.





## 8 Further Work

In this chapter, the proposed further work and the associated discussion are presented, related to the work that should be done to further develop the field of research in fault-detection of photovoltaic modules.

More data should be gathered in regards to the performance characteristics of modules with faults, and images from several or all of the imaging techniques. With this data, one could perform a study to correlate the fault types detected by the imaging techniques to the potential power loss correlating to the fault. Furthermore, one could research the instances where the different fault-detection techniques gives results with or without directly correlating data.

A higher number of techniques should be tested and compared to generate a sufficient amount of data, to make a comprehensive comparison of the available fault-detection techniques. These techniques include, but are not limited to, flash-testing, photoluminescence-testing, UAV-based imaging, in-field variants of the relevant lab-based techniques, and IRT-imaging of modules supplied with backward-bias current.

Given enough computational power, and a large enough data-base of images of modules with faults and the corresponding performance characteristics, it could be possible to develop a fault-detection algorithm with power-loss estimation using machine learning (ML). There are ML-algorithms available, with the capability of processing multiple types of input, like numerical data and images which may be able to be developed for automatic fault-detection, and -analysis.

No standard for ultraviolet fluorescence (UVF) imaging of PV-modules was found when developing the method used in this thesis. There should be developed a standard for UVF-imaging, and any other techniques without standard testing methods, as this would ensure the repeatability and validity of the techniques.



## References

- [1] H. S. Ljosland, "ENE503 – Power loss estimation of different PV-module faults," 2021, unpublished.
- [2] K. Mertens, *Photovoltaics - Fundamentals, Technology, and Practice*, 2nd ed. Croydon: John Wiley & Sons Ltd, July 2018.
- [3] National Renewable Energy Laboratory. (2022) Reference air mass 1.5 spectra | grid modernization | nrel. [Online]. Available: <https://www.nrel.gov/grid/solar-resource/spectra-am1.5.html>
- [4] International Electrotechnical Commission, "Photovoltaic (PV) systems – Requirements for testing, documentation and maintenance -- Part 3: Photovoltaic modules and plants – Outdoor infrared thermography," International Electrotechnical Commission, Geneva, CH, Standard, Jun. 2017.
- [5] M. Köntges, A. Morlier, G. Eder, E. Fleiß, B. Kubicek, and J. Lin, "Review: Ultraviolet fluorescence as assessment tool for photovoltaic modules," *IEEE Journal of Photovoltaics*, vol. 10, no. 2, pp. 616–633, 2020.
- [6] J.-M. Huang, R.-J. Wai, and W. Gao, "Newly-designed fault diagnostic method for solar photovoltaic generation system based on iv-curve measurement," *IEEE Access*, vol. 7, pp. 70 919–70 932, 2019.
- [7] J. A. Tsanakas, L. Ha, and C. Buerhop, "Faults and infrared thermographic diagnosis in operating c-si photovoltaic modules: A review of research and future challenges," *Renewable and Sustainable Energy Reviews*, vol. 62, pp. 695–709, 2016. [Online]. Available: <https://www.sciencedirect.com/science/article/pii/S1364032116301629>
- [8] T. Fuyuki and A. Kitiyanan, "Photographic diagnosis of crystalline silicon solar cells utilizing electroluminescence," *Applied Physics A*, vol. 96, pp. 189–196, 07 2009. [Online]. Available: <https://doi.org/10.1007/s00339-008-4986-0>
- [9] O. K. Segbefia, A. G. Imenes, I. Burud, and T. O. Sætre, "Temperature profiles of field-aged photovoltaic modules affected by optical degradation," Mar 2022, p. 26. [Online]. Available: <https://ssrn.com/abstract=4046700>
- [10] R. Moretón, E. Pigueiras, J. Leloux, and J. Carrillo, "Dealing in practice with hot-spots," 09 2014.
- [11] International Electrotechnical Commission, "Photovoltaic devices – Part 13: Electroluminescence of photovoltaic modules," International Electrotechnical Commission, Geneva, CH, Standard, Aug. 2018.
- [12] M. Köntges, S. Kurtz, C. Packard, U. Jahn, K. A. Berger, T. Friesen, H. Liu, and M. V. Iseghem, "Performance and Reliability of Photovoltaic Systems – Subtask 3.2: Review of Failures of Photovoltaic Modules," International Energy Agency, report, Mar. 2014.
- [13] European Commission, "Communication from the commission to the european parliament, the council, the european economic and social committee and the committee of the regions empty – 'fit for 55': delivering the eu's 2030 climate target on the way to climate neutrality," 2021.

- [14] Eurostat. (2020, dec) Renewable energy statistics - statistics explained. [Online]. Available: [https://ec.europa.eu/eurostat/statistics-explained/index.php?title=Renewable\\_energy\\_statistics#Wind\\_and\\_water\\_provide\\_most\\_renewable\\_electricity.3B\\_solar\\_is\\_the\\_fastest-growing\\_energy\\_source](https://ec.europa.eu/eurostat/statistics-explained/index.php?title=Renewable_energy_statistics#Wind_and_water_provide_most_renewable_electricity.3B_solar_is_the_fastest-growing_energy_source)
- [15] A. Gaur and S. Singh. (2018, January) P-n junction | electronics | britannica. [Online]. Available: <https://www.britannica.com/technology/p-n-junction>
- [16] S. Perkowitz, W. L. Hosch, R. Pallardy, and N. Parwani. (2010, October) Hole | solid-state physics | britannica. [Online]. Available: <https://www.britannica.com/science/hole-solid-state-physics>
- [17] P. Hersch and K. Zweibel, *Basic photovoltaic principles and methods*. Technical Information Office, February 1982. [Online]. Available: <https://www.osti.gov/biblio/5191389>
- [18] C. Honsberg and S. Bowden. Bypass diodes | pveducation. [Online]. Available: <https://www.pveducation.org/pvcdrom/modules-and-arrays/bypass-diodes>
- [19] International Electrotechnical Commission, “Photovoltaic (PV) module performance testing and energy rating – Part 1: Irradiance and temperature performance measurements and power rating,” International Electrotechnical Commission, Geneva, CH, Standard, Jan. 2011.
- [20] S. Wenham, M. Green, M. Watt, and R. Corkish, *Applied photovoltaics*, 2nd ed., 09 2013.
- [21] C. Honsberg and S. Bowden. (2007, mar) Standard solar spectra. [Online]. Available: <https://www.pveducation.org/pvcdrom/appendices/standard-solar-spectra>
- [22] J. Kurnik, M. Jankovec, K. Brecl, and M. Topic, “Outdoor testing of pv module temperature and performance under different mounting and operational conditions,” *Solar Energy Materials and Solar Cells*, vol. 95, no. 1, pp. 373–376, 2011, 19th International Photovoltaic Science and Engineering Conference and Exhibition (PVSEC-19) Jeju, Korea, 9-13 November 2009. [Online]. Available: <https://www.sciencedirect.com/science/article/pii/S0927024810002126>
- [23] Teledyne FLIR LLC. (2021, Nov) How does emissivity affect thermal imaging? [Online]. Available: <https://www.flir.com/discover/professional-tools/how-does-emissivity-affect-thermal-imaging/>
- [24] H. Glavaš, M. Vukobratović, M. Primorac, and D. Muštran, “Infrared thermography in inspection of photovoltaic panels,” in *2017 International Conference on Smart Systems and Technologies (SST)*, 2017, pp. 63–68.
- [25] S. B. Jensen, “Studie av elektroluminescens og strømspenningskurver for å undersøke defektutvikling i solcellemoduler,” Master's thesis, Norges miljø- og biovitenskaplige universitet, 05 2021.
- [26] G. Alves dos Reis Benatto, C. Mantel, S. Spataru, A. A. Santamaria Lancia, N. Riedel, S. Thorsteinsson, P. B. Poulsen, H. Parikh, S. Forchhammer, and D. Sera, “Drone-based daylight electroluminescence imaging of pv modules,” *IEEE Journal of Photovoltaics*, vol. 10, no. 3, pp. 872–877, 2020.

- [27] T. Kropp, M. Berner, L. Stoicescu, and J. H. Werner, "Self-sourced daylight electroluminescence from photovoltaic modules," *IEEE Journal of Photovoltaics*, vol. 7, no. 5, pp. 1184–1189, 2017.
- [28] C. A. Munson, J. L. Gottfried, F. C. De Lucia, K. L. McNesby, and A. W. Miziolek, "Chapter 10 - laser-based detection methods of explosives," in *Counterterrorist Detection Techniques of Explosives*, J. Yinon, Ed. Amsterdam: Elsevier Science B.V., 2007, pp. 279–321. [Online]. Available: <https://www.sciencedirect.com/science/article/pii/B9780444522047500298>
- [29] A. Durgadevi, S. Arulselvi, and S. Natarajan, "Photovoltaic modeling and its characteristics," in *2011 International Conference on Emerging Trends in Electrical and Computer Technology*, 2011, pp. 469–475.
- [30] R. D. Isaksen, "Ir- og dataanalyse for feildeteksjon og diagnostisering av solcellemoduler," Master's thesis, Universitetet i Oslo, 05 2021.
- [31] S. Richter, M. Werner, S. Swatek, and C. Hagendorf, "Understanding the snail trail effect in silicon solar modules on microstructural scale," 01 2012.
- [32] S. Koch, T. Weber, C. Sobottka, A. Fladung, P. Clemens, and J. Berghold, "Outdoor Electroluminescence Imaging of Crystalline Photovoltaic Modules: Comparative Study Between Manual Ground-level Inspections and Drone-based Aerial Surveys," 06 2016, pp. 1736–1740.
- [33] A. Haque, K. V. S. Bharath, M. A. Khan, I. Khan, and Z. A. Jaffery, "Fault diagnosis of photovoltaic modules," *Energy Science & Engineering*, vol. 7, no. 3, pp. 622–644, 2019. [Online]. Available: <https://onlinelibrary.wiley.com/doi/abs/10.1002/ese3.255>
- [34] B. Sopori, P. Basnyat, S. Devayajanam, S. Shet, V. Mehta, J. Binns, and J. Appel, "Understanding light-induced degradation of c-si solar cells," in *2012 38th IEEE Photovoltaic Specialists Conference*. IEEE, 2012, pp. 001 115–001 120.
- [35] K. S. . M. Sinclair, *Silicon Solar Module Visual Inspection Guide*, International Electrotechnical Commission.
- [36] Trotec. Uv-torchlight 15f. [Online]. Available: <https://uk.trotec.com/shop/uv-torch-light-15f.html>
- [37] Canon Incorporated, *Cabib EOS 400D Digital Instruction Manual*, Canon Incorporated.
- [38] Trotec. Uv-torchlight 15f filteraufsatz. [Online]. Available: <https://www.trotec24.com/en-il/measuring-instruments/leak-detection/leak-detection-accessories/uv-torchlight-15f-filteraufsatz.html>
- [39] M. S. Nixon and A. S. Aguado, "3 - image processing," in *Feature Extraction and Image Processing for Computer Vision (Fourth Edition)*, fourth edition ed., M. S. Nixon and A. S. Aguado, Eds. Academic Press, 2020, pp. 83–139. [Online]. Available: <https://www.sciencedirect.com/science/article/pii/B9780128149768000038>
- [40] International Electrotechnical Commission, "Photovoltaic devices – Procedures for temperature and irradiance corrections to measured I-V characteristics," International Electrotechnical Commission, Geneva, CH, Standard, Dec. 2009.

- [41] Mathworks. (2020, 9) Partial shading of a pv module - matlab & simulink - mathworks nordic. [Online]. Available: <https://se.mathworks.com/help/phymod/sps/ug/partial-shading-of-a-pv-module.html>
- [42] Fluke, *Ti200, Ti300, Ti400, Ti450, Ti450SF6, Ti480 Thermal Imagers Users Manual*, Fluke Corporation.
- [43] FileInfo. (2019, may) Is2 file extension - what is an .is2 file and how do i open it? [Online]. Available: <https://fileinfo.com/extension/is2>
- [44] Nikon Corporation, *Digital Camera D5600 Reference Manual*, Nikon Corporation.
- [45] BrightSpot Automation LLC, *EL-Spot Manual*, BrightSpot Automation.



# Appendix

## A Blank IEC Visual Inspection Checklist

Module designation: _____		Initials: _____		Defect present?			
Component	Defect		No	Yes	If yes, Score	Safety Issue?	
1. Label	1.1	Missing					
	1.2	Poorly attached					
	1.3	Information is missing					
	1.4	Incorrect spelling					
2. Back-sheet	2.1	Burn marks					
	2.2	Discoloration					
3. Junction box	3.1	Faulty electrical connection					
	3.2	Cracks/breaks/gaps in housing					
	3.3	Sealant failure					
	3.4	Electrical polarity not indicated					
4. Wiring	4.1	Cracks or exposed metal					
5. Frame	5.1	Damaged					
	5.2	Adhesive/sealant failure					
6. Front glass	6.1	Cracking					
	6.2	Scratches					
7. Encapsulation	7.1	Discoloration					
8. Cells	8.1	Snail-trails					
	8.2	Shiny locally/inconsistent colour					
9. Cell Metallization	9.1	Fingers not connected to busbar					
	9.2	Not the same pattern on all cells					
	9.3	Fingers off of edge of corner of cells					
10. Cell interconnection	10.1	Interconnection is discontinuous					
	10.2	Cells connected in parallel (counterfeit)					
	10.3	Poorly aligned and/or soldered					
	10.4	Cells connected in parallel (real cells)					
Summary Indicate if any defects and safety issues are present and sum of score.							

## B Westech CL-160WM Data-Sheet



### Monokristalline Module Größe: 160 Watt



#### Technische Daten

Spitzenleistung(W)	160W
Spannung bei max. Leistung(Vmp)	18,10V
Strom bei max. Leistung(Im)	8,85A
Leerlaufspannung(Voc)	22,20V
Kurzschlußstrom(Isc)	9,60A
Zellwirkungsgrad(%)	18.48%
Modulwirkungsgrad(%)	15.35%
Leistungstoleranz	0%+3%
NOCT(normale Zelltemperatur)	45°C +/-2°C

#### Vorteile

- hocheffiziente Solarzellen mit hoher Transmission und texturiertem Glas liefern hohe Effizienz für Module;
- Bypass-Dioden minimieren den Leistungsabfall bei Verschattung;
- Gehärtetes Glas, EVA-Kunststoff und witterungsbeständige Folie, plus Aluminiumrahmen für den Langzeiteinsatz im Außenbereich;
- Module unabhängig getestet, um die Konformität mit Normen und Zertifikaten zu garantieren;
- Fertigung nach ISO 9001 zertifiziertem Qualitäts-Managementsystem-Normen.



#### Anwendungen

- On-Grid Dächer /Privathäuser
- On-grid Gewerbe / Industrie Dächern
- Solarkraftwerke
- Off-Grid Inselanlagen

#### Temperaturkoeffizienten

Temperaturkoeffizient	Is <sub>c</sub> (%) °C	+0.04
Temperaturkoeffizient	Voc(%) °C	-0.35
Temperaturkoeffizient	P <sub>m</sub> (%) °C	-0.45
Temperaturkoeffizient	I <sub>m</sub> (%) °C	+0.04
Temperaturkoeffizient	V <sub>m</sub> (%) °C	-0.35



# Monokristalline Module

## Größe: 160 Watt

### Technische Daten

Solarzelle	125*125 Mono
Anzahl der Zellen(Stück)	4*9
Modulgröße(mm)	1480*680*35
Glasstärke(mm)	3.2
Maximale Tragkraft der Oberfläche	2400-5400Pa
Zulässige Belastung durch Hagel	23m/s ,7.53g
Gewicht pro Stück(KG)	11,50
Bypass- Dioden Rating(A)	10
Rahmen(Aluprofile.)	35 mm
Rückseitenfolie (Typ)	TPT
Temperaturbereich	-40°C bis +80°C
Anschluss	70-76%
Standard Testbedingungen	AM1.5 1000W/3j 25 +/-2 °C

### Verpackung

Verpackung	Holzkasten/ Palette/ Karton
Stück pro	1 Stück im Karton

### Projektbild



### Konstruktionszeichnungen

Model	CL-160Ww		
Designed by	Checked by	Approved by	Date
			8/12/2016

© Westech Solar Alle Rechte vorbehalten.

Daten in diesem Datenblatt können bei technischen Änderungen ohne Vorankündigung geändert werden.



WestechSolar-Energy GmbH  
 Robert-Koch-Str. 3a  
 82152 Planegg  
 Tel. 089 89545770  
 Fax 089 89545771  
[www.westech-energy.com](http://www.westech-energy.com)